^{23}Na multi-quantum coherences: from cellular spectroscopy to clinical imaging development

Referees: Prof. Dr. Lothar R. Schad

Prof. Dr. Peter Bachert

DISSERTATION

submitted to the
Combined Faculty of Natural Sciences and Mathematics
of Heidelberg University, Germany
for the degree of
Doctor of Natural Sciences

put forward by
Michaela Anna Ulrike Hösl, MSc
born in Freising, Germany
Oral examination: January 22, 2019

Michaela Anna Ulrike Hösl, MSc

^{23}*Na multi-quantum coherences: from cellular spectroscopy to clinical imaging development*

DISSERTATION, January 22, 2020

Referees: Prof. Dr. rer. nat. Lothar R Schad and Prof. Dr. rer. nat. Peter Bachert

Supervisors: Prof. Dr. rer. nat. Lothar R Schad

Heidelberg University

Computer Assisted Clinical Medicine

Medical Faculty Mannheim

Department of Physics

Theodor-Kutzer Ufer 1-3

68167 and Mannheim

ZUSAMMENFASSUNG

Nicht invasive Verfahren zur Bestimmung von biologischen Informationen sind wichtig für die medizinische Diagnose und die Überwachung des Behandlungsverlaufs. Protonen Magnet Resonanz Tomographie (MRT) Techniken geben detaillierte morphologische Informationen. Die ^{23}Na MRT bietet direkte, biochemische Gewebeinformationen. Natrium Werte steigen z.B nach Gewebeverletzungen an. Natrium Kerne, haben Spin 3/2, und können höhere Quanten Kohärenzen ausbilden. Die Standard ^{23}Na MRT, die bisher Anwendung in klinischen Studien findet, misst allein das Single Quantum (SQ) Signal zur Bestimmung des Natriumgewebegehalts (TSC). Um ein vollständiges Bild des Natrium Signals innerhalb von Geweben erhalten zu können, ist es wichtig, die Multi Quantum (MQ) Kohärenzsignale zu messen. Der Fokus dieser Arbeit lag auf drei Teilen: Zuerst der physiologischen Untersuchung des ^{23}Na Triple Quantum (TQ) Signals am Hochfeld Präklinischen 9.7 T MRI mit lebend Zellexperimenten. Die präklinische Erforschung des TQ Signals von humanen Leberzellen (HEP G2) und neonatalen Herzmuskelzellen der Maus wurde realisiert durch einen speziellen MR kompatiblen Bioreaktor, der sowohl ein Aufrechterhalten von gleichbleibenden Bedingungen im MRT ermöglicht, als auch gezielte Veränderungen zulässt. Die umstrittene Theorie der “Trennung von Intra - und Extrazelluärsignal” wurde mittels Liposomen untersucht. Die Entwicklung einer Ein-Voxel Spektroskopie Methode stellte den ersten Schritt in Richtung einer klinischen MQ Sequenz dar, die an Phantomen und an einer Ratte in vivo getestet wurde.

Beide Zelllinien zeigten ein TQ Signal im lebenden Zustand und unter normaler Nährstoffversorgung mittels Zellmedium Perfusion von [0.26%,15σ] normalisiert zum SQ Signal. Sauerstoffmangel und Nährstoffzufuhrstopp führen physiologisch zu einer Hypertrophie, die im Bioreaktor gemessen werden konnte. Ein Rückgang des TQ Signals auf 56% des Ausgangsniveaus wurde gemessen [0.15%,24σ], das bei Rückkehr zu Normalbedingungen mit 92% auf nahezu Ausgangsniveau zurückkehrte. Die Referenzmessung im Bioreaktor ohne Zellen lieferte ein TQ Signal von [0.06%,1σ].AuSSerdem konnte gezeigt werden, dass bei irreparabel geschädigten Zellen kein TQ Signal mehr vorhanden war [0.016%,1σ]. Dies belegt die Relevanz des TQ Signals in biologischem Gewebe. Den zweiten Teil der Arbeit bildete die Simulation der Drei-Puls Sequenz zum Kohärenztransfer. Das Ziel war die Entwicklung eines “Frameworks” zur Untersuchung der Signale unter verschiedenen Phasenzyklen und das Finden der Parameter für eine optimale, klinische MQ Messung. Die MQ Signale verschiedener Phasenzyklen wurde für verschiedene Echozeiten, unter Einfluss von Störungen simuliert. Destruktives Signalverhalten bei B0 Inhomogen-

itäten wurde verifiziert für $\Omega(Hz) = (k\pi + \xi)/(\tau_1), k \in \mathbb{Z}$. Stimulierte Echosignale waren ein weiterer potentieller Störfaktor, der allerdings in einem konstanten Offset nach Fourier Transformation, die übrigen MQ Signale nicht beeinflusste.
Im dritten Teil wurden die Erkenntnisse aus Teil I und Teil II auf den klinischen Transfer und die Entwicklung der klinischen Bildgebungssequenz angewendet. Eine 2D kartesische MQ, multi-echo Sequenz (CRISTINA) wurde entwickelt und implementiert. Durch die Entwicklung einer Fit Routine konnten Relaxations und TQ als auch SQ Karten und dessen Verhältnis erstellt werden, die zur Beurteilung der Gewebevitalität dienen können. Die Sequenz wurde am Phantom und in 5 gesunden Probanden im Kopf validiert und optimiert. TQ zu SQ Verhältnis zu Agar Konzentration ergaben ein lineares Verhältnis (R^2 =0.87, p-value = 0.0007), ebenso wie SQ Signal zu Natriumkonzentration, zur Bestimmung des Natriumgehalts im Gewebe (R^2 =0.75, p-value = 0.006).

ABSTRACT

Non-invasive biological tissue information is vital for medical diagnostics and treatment monitoring. While standard ^{1}H magnetic resonance imaging (MRI) methods show detailed morphological information, ^{23}Na MRI provides additional biochemical information about the tissue. Sodium nuclei have spin 3/2 and, therefore, can exhibit higher quantum coherence signals. Multi-quantum (MQ) imaging offers additional information compared to standard SQ sodium, which focuses on tissue sodium concentration (TSC), e.g., it is hard to discern edema and tumor regions, both exhibiting higher TSC. ^{23}Na triple-quantum (TQ) signals are of high interest to probe the molecular environment in tissues and alleviate this problem.

The focus of this thesis was on the ^{23}Na TQ signal from preclinical investigations on cells via a simulation study and, finally, a transfer of preclinical and simulation findings into the development of an optimal clinical MQ imaging sequence, CRISTINA.

First, the physiological importance was studied at ultra-high field, 9.4 T, to gain insight into TQ signal changes under different cellular conditions. An MR-compatible bioreactor setup allowed for finely tunable TQ signal monitoring of cell lines human liver cells (HEP G2) and neonatal cardiomyocytes of mice. Both cell lines showed a TQ signal in vital state, under standard perfusion [0.26%,15σ], normalized to the SQ signal. Hypertrophy was simulated with oxygen and nutrient stop and resulted in a TQ signal to 56% of the initial value [0.15%,24σ]. Re-perfusion resulted in a come back of the TQ signal to 92% of the initial value. Reference measurements without cells as well as dead cells showed a TQ signal of [0.06%,1σ and 0.016%,1σ].

Further, the long-standing debate of TQ signal connection to intracellular space was investigated based on liposomal cell-phantoms and it was shown that the TQ signal in liposomes was related to the interaction of the sodium ions with the double lipid membrane, which is constituted of negatively charged fatty acids. A single-voxel localization technique was developed on the preclinical system as the first step in the direction of a clinical sequence and tested on phantoms and in-vivo rat.

Second, simulation of different phase-cycle schemes of the standard three-pulses coherence transfer technique was performed. A unified framework was developed to compare and find an optimum. Destructive effects of B0 inhomogeneity were investigated and verified for $\Omega(Hz) = (k\pi + \xi)/(\tau_1), k \in \mathbb{Z}$. Stimulated echo signal stood as further potential biases but resulted in a continuous offset after Fourier Transformation.

Third, knowledge from part I and II was transferred to develop an efficient clinical

MQ imaging method: CRISTINA, a 2D Cartesian MQ, multi-echo imaging sequence for clinical use. A Multi-parameter fit routine provided T2 relaxations maps and ratio of TQ to SQ signals which could be of interest to monitor pathologies in future. CRISTINA was tested and optimized on phantoms and in vivo on 5 healthy brain volunteers. A linear relationship was found for the ratio TQ over SQ signal against agar concentrations (R^2 =0.87, p-value = 0.0007) as well as for the SQ signal against TSC (R^2 =0.75, p-value = 0.006).

Acknowledgement

Ich möchte herzlich meinem Professor, Lothar Schad danken, für die Möglichkeit bei Ihm an der Universität Heidelberg in Physik zu promovieren. Besonders geschätzt habe ich Ihre offene und unterstützende Art, vor allem hinsichtlich meines Auslandsaufenthalts und Projektwahl. Ein herzliches Danke an meine Mannheimer Kollegen: Basti und Valerie mit denen in für einige Zeit mein Büro geteilt habe. Darüberhinaus, Danke an Alena, Efe, Edgar, Irène, Ingo, Jorge, Nadja, Simon, Sebastian, Tanja, Tom, Wiebke, für die sportlichen Tätigkeiten und schöne Zeit. Besonderer Dank gilt meiner X-Nuclei Gruppe mit Dennis, Ruomin, Nadia, Anne und Matze. Vor allem an Dennis: Danke für deine Unterstützung, die Diskussionen und auch für meine erste Skitour und erstes Skating.

À l'ensemble de l'équipe du CEMEREM, Centre d'Exploration Métabolique par Résonance Magnétique: j'ai passé huit mois chez vous et c'était une de mes phases préférées de mon PhD. Merci pour votre accueil chaleureuse. Spécialement à mes collègues avec qui j'ai partagé le bureau: Arash, Luca, Tangi, Clémentine, Guillaume, Simon, Soraya, Audrey, Zak. Plus particulièrement un merci à mon supervisor et collaborateur Stanislas Rapacchi: J'avais la chance d'avancé mon project avec ta soutenance. Ces mois étaient un vrai plaisir de travailler avec toi. Avec ta curiosité, ton soutien, tes précieux conseils et nos discussions j'ai avancé beaucoup plus que je n'avais pas imaginée avant. Un grand merci aussi à Olivier et Jean-Philippe pour tous les discussions intéressantes.

An meine Musikerfreunde: Gerade während der Doktorarbeit ist Ausgleich wichtig und den habe ich mit der Akademischen Philharmonie Heidelberg gefunden. Es waren nicht nur aufregende und höchst anspruchsvolle Programme zu meistern wie z.B. Strawinsky's Feuervogel oder Strauss' Alpensinfonie, ich habe dort mit euch entspannen und mich in Heidelberg einleben können. Euch werde ich sehr vermissen! Einen besonders herzlichen Dank an meine Pultis: Feli, Philip und Lucy, an die Geigengruppe mit Leonie, Julia und Ellie und an unseren Dirigenten Jesko der uns so schön getriezt hat und mich dazu gebracht hat mehr zu üben. An meine Freunde in Heidelberg, insbesondere Matthias, Mira, Barbara und Anna mit denen

ich viel Spaß in Musik und Sport hatte.

An meine Familie: Der größte Dank gilt meiner Familie, meinen Eltern, Großeltern, und meinem Bruder Andreas, die zu jeder Zeit präsent waren und mich unterstützt haben. Allein meine ganzen Umzüge von München über Boston nach Utrecht, Mannheim und Marseille und wieder zurück nach Heidelberg wären ohne euch alle nicht möglich gewesen. Meine Höhen und Tiefen der Doktorarbeitsphase habt ihr miterlebt und mich immer beraten und unterstützt. Danke Andreas, dadurch dass ich dir seit dem Studium alles nachgemacht habe inklusive Doktorarbeit konntest du immer direkt nachvollziehen wie es mir geht und mir Tipps geben. Finalement, merci à Simon: Tu a rendu cette dernière phase du PhD tellement plus heureux et je te remercie pour me donner du motivation et encouragement. Thank you!

Contents

Acronyms

2D two-dimensional. 9

3D three-dimensional. 8

ADC analog-to-digital converter. 13

CON cones. 29

CRISTINA Cartesian Imaging of Single and Triple Quantum signals In ^{23}NA. 10

DA-RP density adapted radial projection. 29

DQ Double Quantum. 3

DQC Double Quantum Coherence. 38

FOV field of view. 27

FT Fourier Transform. 10

GRE gradient echo. 25

MQ Multi Quantum. 3, 9

MR magnetic resonance. 3

MRI magnetic resonance imaging. 3

NMR nuclear magnetic resonance. 3

POCS projections onto projections onto convex sets. 27

PSF point spread function. 30

RAD radial acquisition. 29

RF radio frequency. 13

SENSE sensitivity encoding technique in parallel imaging. 29

SNR signal to noise ratio. 3, 13

SQ Single Quantum. 3

SQC Single Quantum Coherence. 38

STE stimulated echo. 10

TPI twisted projection imaging. 29

TQ Triple Quantum. 3

TQC Triple Quantum Coherence. 38

TQTPPI Triple Quantum Time Proportional Phase Increment. 10

UTE ultra-short echo time. 29

1 Introduction

1.1 Motivation and Problem Statement

While ^{1}H magnetic resonance imaging (MRI) is an established clinical tool to visualize soft tissue contrast, sodium magnetic resonance (MR) techniques are up to now of a rather exotic type in the world of clinical MRI. Standard clinical protocols use ^{1}H images to find tissue anomalies and to distinguish a tumor from healthy surrounding tissue. Despite the technological advances in ^{1}H MRI techniques, there is a role for other nuclei, so called “X-nuclei" MRI and nuclear magnetic resonance (NMR) methods, the latter refers to spectroscopic methods. Both techniques can reveal physiological information in addition to morphology. X-nuclei of interest exhibit a nonzero spin and are naturally abundant in vivo. They are worth having a deeper look to leverage the additional biochemical information about cell physiology and viability that especially the ^{23}Na nuclei measurements offer. Despite sodium MRI techniques starting around 30 years ago, it remains primarily a research tool meeting little clinical response up to now. The spin $^{3}/_{2}$ of the quadrupolar sodium nucleus results in multi-quantum (MQ) coherences that can be observed under certain conditions. In the case of sodium nuclei MQ coherences denotes single-, double-, and triple quantum (SQ, DQ, TQ) coherences signals. Already in the early days of sodium NMR, the concepts and physics for MQ sodium NMR were investigated and described [1, 2, 3, 4, 5, 6]. In standard sodium MRI, at clinical scanners, excitation and detection of solely the SQ transition is performed which shows parallels to ^{1}H MRI, where with spin $^{1}/_{2}$, a transition is only possible between the two energy states. The inclusion of MQ coherence signals offers the full potential of the spin $^{3}/_{2}$ sodium nuclei and results in a complete picture that could enhance clinical diagnostics.

For sodium MRI scans specific requirements have to be met which withheld X-nuclei techniques from gaining popularity. Additionally, costly hardware is necessary to excite and measure at a different frequency. Furthermore, the lower gyromagnetic ratio (γ) leads to a reduction in signal to noise ratio (SNR). The lower natural abundance, compared to proton nuclei, further lowers the SNR. Sodium images cannot compete with proton MRI images for morphological information due to the lower SNR. Other obstacles are sodium MRI sequences and reconstruction algorithms which are not

standardly available which complicates the transfer and application of research findings. Recent technological advances resulted in higher available field strengths up to 7 T for clinical and 9.4 T for pre-clinical MRI scanners. Improved gradient systems offer new sequence design possibilities. These developments led to a revival of sodium MRI as the search for advanced diagnostic tools continues, even with all the progress of high resolution morphological proton MRI images. Alongside, increased computer performance offers improved post-processing. Establishing a biomarker with sodium MRI signals [7, 8, 9, 10] might be a game changing information for various diseases, such as in stroke [11, 12], multiple sclerosis [13, 14, 15, 16] and for radiotherapy treatment monitoring [17]. Common body sites for sodium MRI are the kidney [18, 19], the brain [20], the heart [10] and in the cartilage of the knee[21].

Physiological role The ^{23}Na TQ coherences signal gives more information about cell vitality than the SQ coherences signal alone [22] and thus plays a role in preventive diagnostics in the future. The regulation of electrical and chemical gradients across cell membranes by specific ion levels is the underlying basis for many biological processes, such as repeated muscle cell contractions, maintenance of the resting membrane potential, neuronal action potential formation and transmission along nerve fibers[9]. The complex interaction of charged ions maintains or deliberately changes the electric potentials across cell membranes. There is a large gradient between intracellular ($Na_{int} \approx 15$ mM) and extracellular sodium ($Na_{ext} \approx 140$ mM). The sodium potassium pump exchanges Na^+, K^+ ions under energy consumption to maintain this large gradient which would otherwise strive to equilibrium by sodium ions entering regularly at different channels. Three sodium ions are pumped from intracellular space to the extracellular space with two potassium ions being exchanged against the electrochemical gradient (Figure 1.1). Further ions of interest are Cl^- and, especially for muscle cells Ca^{2+}. In case of fading cell vitality or abnormal high cell division rates, as in tumor cells, homeostasis is disturbed and sodium levels increase within cells. Increased intracellular sodium levels can be harmful and lead to cell swelling and eventually to cell death [8]. As sodium MRI measures mean concentrations for voxel signals, a problem of distinguishing two cases arises: 1) Increase due to higher intracellular sodium levels or 2) Increase of extracellular space in case of cell death and apoptosis. This problem is known as the Hilal ambiguity [23]. It has to be kept in mind that the blood pool offers an abundant source of sodium ions for maintaining the extracellular level. Separating the signal of the intra- and extracellular sodium is therefore of clinical interest. In the MRI community the distinction of those two compartments has been subject to longstanding discussions. Initially the two relaxation rates, characterizing the

bi-exponential transversal decay for sodium where thought to be attributable to the two compartments. However, studies showed the bi-exponential decay stems from intra-, as well as extracellular space [24]. Toxic chemical shift reagents are currently the only way to resolve extra- and intracellular sodium, reserved for preclinical studies [25]. Shift reagent experiments in an in-vivo rat reported that approximately 60 % of the TQ signal originates from the intracellular compartments [26] which are considered more densely packed by proteins e.g. in form of cell-organelles than extracellular space. Therefore the TQ signal was attributed to a possibly differentiate between intra- and extracellular signal [27, 5, 28, 29, 30, 31, 32]. Although it was reported that evidence for the hypothesis was lacking [10, 24]. Molecules and proteins are in direct environment of sodium ions on both sides of the cell membrane with a mean lifetime of interaction in the order of 10^{-9}s [33, 34] and bound states of the sodium ions therefore do not exist. However, there remains controversy as to whether the TQ signal can distinguish between intracellular and extracellular compartments.

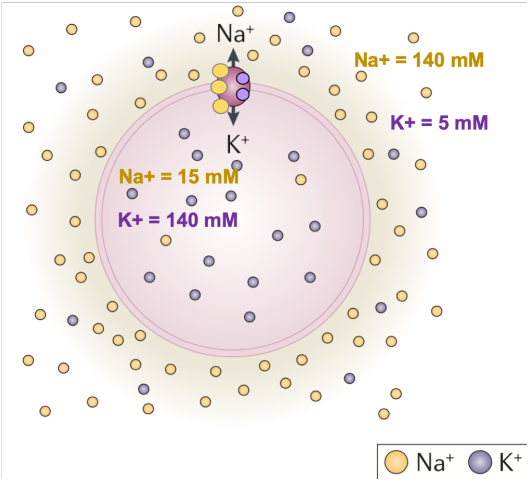

Figure. 1.1: Simplified scheme of a cell visualizing the steep gradient between the intracellular and extracellular Na concentration. The sodium potassium pump works constantly under consumption of energy to maintain this steep gradient.

Multi quantum (MQ) sodium signals The ^{23}Na relaxation processes are determined by the electric-quadrupole interaction and fundamentally distinguishes it from the dominant dipole-dipole interaction of proton nuclei. Sodium spin 3/2 nuclei exhibit four possible energy levels. Depending on the surrounding medium different transitions between the levels are possible. Inhomogeneous distribution of the electron clouds leads to an electric field gradient (EFG). The EFG of the medium changes e.g. in the presence of macromolecules leading to a fluctuating quadrupolar interaction. The quadrupolar moment of the spin 3/2 nuclei couples to the EFG and results in the

possibility of forming higher quantum coherences signals. In biologic environment, the fluctuating quadrupolar interaction adds to the Zeeman splitting and leads to a bi-exponential relaxation behavior so that DQ and TQ coherences signals can be observed (Figure 1.2b). In an anisotropic environment, the quadrupolar moment of the sodium nuclei couples to the EFG which acts as relaxation mechanism and leads to a more rapid decay of the outer than inner transitions w.r.t the spin 3/2 energy levels. This effect results in a bi-exponential T2 relaxation, with fast and slow components, which gives the possibility of MQ transfer due to violation of the coherence transfer rules [4, 5, 35]. In contrast, the quadrupole moment does not couple to an isotropic field, therefore no higher order quantum coherences can be measured (Figure 1.2a). A static quadrupolar interaction is observed in further macroscopically ordered environments, which is rare in biological medium but can for example be found in cartilage (Figure 1.2c). DQ coherences signal can yield information about the anisotropy in tissue because in ordered structures, there exists a preferred orientation of the quadrupolar sodium nuclei relative to the magnetic field B0. DQ coherences arise from two mechanisms: bi-exponential relaxation (T_{32}) and quadrupolar splitting (T_{22}) [5, 36]. Only if a magic angle sequence is used, does the DQC signal solely relate to macroscopically ordered signal by selecting the T_{22} contribution, otherwise the signal stems from both, T_{32} and T_{22}, contribution and gives no specific information. Quadrupolar splitting within anisotropic structures has no additional effect [37, 38]. Biological tissue exhibits two dominant types of sodium spectra where the isotropic motion is $\omega_0 \cdot \tau_c \approx 1$, with long correlation times τ_c, and results in the characteristic MQ coherences [35, 27, 36]. Figure 1.2 shows the relevant processes in analogy to [35, 27]. MQ signals can be measured by dedicated MRI and NMR sequences which is the core of this thesis and especially the ^{23}Na TQ coherences signal is of interest to give information about the interaction of the sodium nuclei with the surrounding environment.

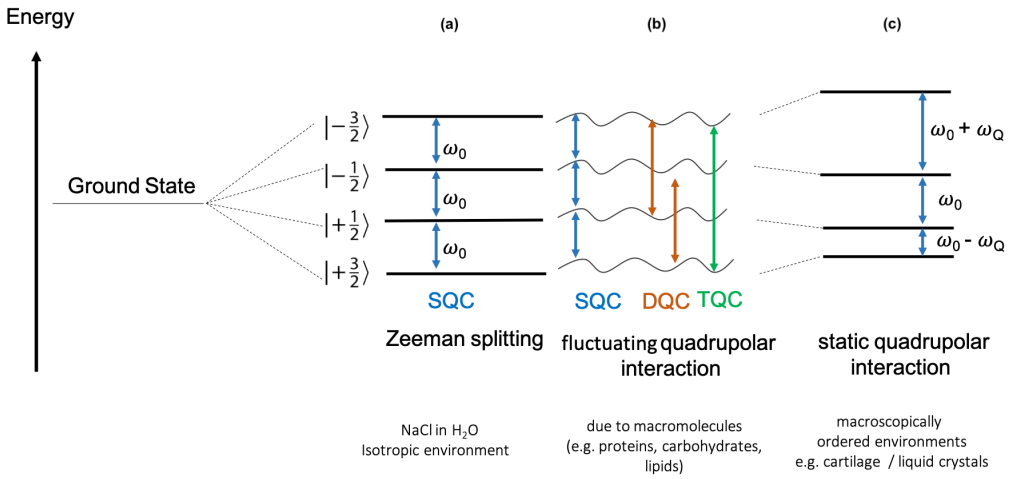

Figure. 1.2: Energy Level Splitting for Spin 3/2 Quadrupolar Nuclei: ^{23}Na spin 3/2 nuclei interaction with a magnetic field: (a) In isotropic environment, the ground state splits into the 4 different energy levels with equidistant levels. (b) In biologic environment fluctuating quadrupolar interaction leads to observation of DQ and TQ coherences. (c) Static quadrupolar interaction in ordered environments is rare in biological medium.

1.2 Thesis Structure

It is of fundamental importance to better understand the TQ signal in biological tissue studied e.g. on the cellular level as well as sequences for in-vivo measurement to evade potential pitfalls. This thesis is built on three main parts, to fully exploit the potential of the triple quantum (TQ) sodium signal for MRI: The physiological role of MQ ^{23}Na signal was investigated in a **preclinical** setup (I) a **simulation** study offered an intuitive way of understanding and comparing different phase cycling methods (II) to implement a robust and efficient **clinical** sequence for MQ sodium measurement.

The focus was to first explore and find the physiological importance of the TQ signal by leveraging the potential of ultra-high field preclinical techniques. The aim was to get a deeper insight in the TQ signal formation of cells and in addition it was investigated whether intracellular space foremost generates the TQ signal. A specially built bioreactor served for finely tuned experiments to monitor the TQ signal of signal of cells in different conditions. The hypothesis of the TQ signal as a discriminator for intra- and extracellular signal was investigated on liposomes and nanoparticles and human HEP G2 liver cells, using a spectroscopic TQ sequence. Liposomes can function as cell-phantoms to model biological membranes and study the limited freedom of ^{23}Na ion movement due to partial trapping [39, 40, 41, 42]. Nanoparticles have broad applicability in biomedical science and have been chosen as a closed compartment model of cell size without the characteristic double lipid membrane of cells [43]. Liposomes and nanoparticles were used as simplified cell phantoms in structure and size, to narrow down the TQ signal generation based on confined space. Cells can be monitored in an MR system with usage of an MR-compatible bioreactor [44, 45] which enabled the monitoring of the TQ signal of cells in a finely tunable system which allows for stimulation of the cells. A 3D cell culture served as a tissue approximation and facilitates transfer of the preclinical physiological findings into the clinic. Signal localization methods were investigated via sequence programming in the pre-clinical environment to find an optimal way of measurement for a clinical setting. Further, the transfer of the initial spectroscopic sequence to the standard 3T clinical environment showed sufficient SNR to render localization of the TQ signal a feasible investment at lower field strengths.

Ultimately the strength of simulation was used by re-formulating and transferring the complex theory into an easy to use and understandable tool to simulate dif-

ferent choices of sequence parameters. This resulted in an intuitive and pictorial understanding of the concept of phase cycling choices in the standard three-pulses-experiment.

Finally, based on the simulation results, a choice of optimal sequence design for clinical TQ imaging methods which can withstand biases was developed and implemented for clinical scanners. The 2D MQ multi-echo sequence features simultaneous measurement of TQ and SQ signals at their respective optimal echo time. Evaluation was performed on agar phantoms. Further, multi parameter fitting routines were developed to characterize the MQ signal evolution which might prove useful for tissue characterization. The developed sequence was finally tested on five healthy volunteers in brain.

Parts of the presented thesis are published in journal articles [22] and [46] as well as in international conference contributions. Relevant developments for preclinical, simulation and clinical acquisitions are available at https://github.com/MHoesl/with matching example data.

1.3 Key Results

- Viable cells exhibit a ^{23}Na TQ coherence signal whereas dead cells do not. This was found by preclinical investigations at 9.4 T with an MR compatible bioreactor using a three pulses spectroscopic sequence (“TQTPPI").
- Liposome and nanoparticle experiments with different intra - and extra-liposomal sodium showed that the TQ signal came from sodium ions within the double-lipid membrane of the liposomes. Transfer to cell measurement results could attribute the TQ signal to the interaction of sodium ions with transmembrane proteins such as the sodium potassium pump.
- Single voxel localization techniques were implemented and tested in phantom and in-vivo rat on the pre-clinical 9.7 T system. A multi-parameter fitting routine for the oscillating time domain signal was developed to retrieve the parameters of interest: T2$_{fast}$ and T2$_{slow}$ values as well as TQ to SQ signal ratio.
- The preclinical global spectroscopic sequence was successfully transferred to the clinical system. Sufficient signal strength at the clinical 3T scanner encouraged further localization of the signal.
- The simulation study simulated the most common four options of phase-cycling techniques, under the influence of biases. Especially B0 inhomogeneity was found to lead to signal nulling and two phase cycles with a phase difference of $\pi/2$ need to be used to recover an unbiased signal. Stimulated echo signal (STE)biases were can be mitigated with a B0 map but are also separated by Fourier Transform (FT).
- A multi-echo sequence, CaRtesIan Imaging of SQ and TQ signals In ^{23}NA “CRISTINA" was developed for clinical scanners to measure MQ coherence signals without biases. A fitting routine over the multi-echo signal was developed to extrapolate the SQ signal to an echo time of 0 ms, for an unbiased SQ to TQ ratio and to obtain T2 relaxation maps.
- CRISTINA was successfully used in five healthy volunteers at 7 T in the brain and showed consistent signal strength.

General Background

2

> *All science is interdisciplinary - from magnetic moments to molecules to men*
>
> — **Paul C. Lauterbur**
> Nobel Lecture 2003

Fundamentally, the concepts of nuclear magnetic resonance (NMR) and magnetic resonance imaging (MRI) can be understood using the theory of quantum mechanics. Commonly, the ^{1}H proton nuclei are utilized in clinical MRI methods. In contrast to ^{23}Na nuclei, a classical picture exists for the behavior of the proton nuclear spins. The model suffices for most proton MRI concepts and will be shortly presented as a basis for the understanding of MRI and the sequences that were developed.

2.1 Nuclear Magnetic Resonance

Magnetic Resonance is a huge scientific field nowadays with many different techniques and applications. The development of those techniques drove forward modern medical care to the state we are used to, today. None of those techniques would have been introduced if it wasn't for key findings about the very basic principles. It started in 1945, when radio-frequency signals were detected in matter by Purcell et al. Bloch et al. were doing experiments on water at the same time and observed radio signals of the nuclei. These two observations laid the groundstone for magnetic resonance and the Nobel Prize in Physics was awarded to E. M. Purcell and F. Bloch in 1952.

Atoms and Nuclei and Spin

What are we looking at? Phantoms made of liquid solutions of ions and human or animal tissue are main examples of matter studied in medical NMR and MRI investigations. Both are an assembly of atoms made of nuclei and surrounding electrons with the properties of mass and electric charge, important for binding by strong electrostatic interactions. Further properties are magnetism and spin.

Nuclear magnetism is weak and has little effect of the structure of molecules.

The concept of spin was introduced by experimental evidence by the Stern-Gerlach-Experiment. The following short explanation follows [47]. Heated silver atoms escaped through a tiny hole in form of a beam. The collimated beam was subsequently exposed to an inhomogeneous magnetic field. The silver atoms consist of a nucleus and 47 electrons. All electrons except one form a symmetrical electron cloud around the nucleus and therefore do not exhibit net angular momentum. The 47^{th} electron's spin gives the angular momentum of the whole atom and determines the magnetic moment μ. The atoms in the magnetic filed, $\vec{B_z}$, experience a force: $F_z = \frac{\delta}{\delta z}(\mu B) \approx (\mu_z)\frac{\delta B_z}{\delta z}$.The Stern Gerlach experiment measures the z-component of μ, equivalent to z-direction of the spin, by the relationship $\mu = \frac{e}{m_e c S}$. Classically a distribution of values for μ_z was expected but the experiment showed a split of the silver atom beam in two values: $S_{z,up} = \hbar/2$ and $S_{z,down} = -\hbar/2$, with Planck's constant $= \hbar = 6.5822x10^{-16}eV/s$. Sequential Stern-Gerlach experiments, with magnetic fields in different directions, showed the peculiarities of quantum mechanics and the fact, that different direction spins cannot be measured at the same time. The observation led to the introduction of spin and the representation of the spin state in a two-dimensional vector space, which must be complex to describe all spin states, in the bra and ket notation, developed by Dirac with $|S_z;+\rangle = |+1/2\rangle = |+\rangle$ and $|S_z;-\rangle = |-1/2\rangle = |-\rangle$:

$$
\begin{aligned}
|S_x;\pm\rangle &= \pm\frac{1}{\sqrt{2}}|+\rangle + \frac{1}{\sqrt{2}}|-\rangle \\
|S_y;-\pm\rangle &= \frac{1}{\sqrt{2}}|+\rangle \pm \frac{i}{\sqrt{2}}|-\rangle
\end{aligned}
\tag{2.1}
$$

The dimensionality of the vector space depends on the number of alternatives, which are just two for a spin 1/2 system. Physical states are eigenstates with eigenvalues in the form of, here for spin 1/2:

$$
\begin{aligned}
S_z|S_z;\pm\rangle &= \pm\frac{\hbar}{2}|S_z;\pm\rangle \\
S_x|S_x;\pm\rangle &= \pm\frac{\hbar}{2}|S_x;\pm\rangle
\end{aligned}
\tag{2.2}
$$

The MRI system

In general, a modern MRI scanner consists of superconducting coils, transmit-, and receive coils which establish a magnetic field, measured in units of Tesla (T). The main field strengths of the scanners available for the presented thesis were 9.7 T for pre-clinical measurements as well as 3 T and 7 T for clinical measurements. A measurement at an MRI machine is called a sequence that is carried out in different steps: one or multiple radio frequency (RF) pulses (in the order of μT) transmitted by the so called transmit coils. Further, the main magnetic field is varied spatially by gradients, in the order of mT. The resulting answer from the tissue is recorded by an analog-to-digital converter (ADC unit) with the so called receive coils. The received signal, called an “echo", is a complex signal with real and imaginary values. Usually such a sequence is repeated multiple times, either for the acquisition of a spatially localized signal (in case of an MRI image) or for averaging and therefore increasing the signal to noise ratio (typically in spectroscopy but also applied in imaging techniques). The acquired signal is post-processed to form a spectrum or an image, depending on the sequence design. The higher magnetic field strength is favorable to achieve higher signal to noise ratio (SNR) [48] which is especially valuable for sodium to compensate for the lower natural abundance compared to hydrogen.

2.1.1 The Nuclear Magnetic Resonance Signal

Protons are a spin 1/2 nuclei with two possible energy states: +1/2 and -1/2. Felix Bloch described the main processes of NMR with the so called Bloch Equations. They are a good model to understand spin 1/2 MRI and general relaxation processes and are therefore mentioned briefly:

In an external magnetic field, the spins process around its main axis, usually denoted as the z-direction in a three dimensional space. The precession frequency, called the Larmor frequency, is determined by the magnetic field strength and the gyromagnetic ratio, γ, which depends on the charge and the mass of the nuclei. The combination of the magnetic moment μ and the angular momentum $\vec{J}$ results in clockwise precession of the magnetic moment vector around the main magnetic field.

$$\text{Larmor Frequency: } \vec{\omega}_0 = \gamma \vec{B}_0 \tag{2.3}$$

$$\text{gyromagnetic ratio: } \gamma = \frac{e}{m} = \frac{J}{\vec{\mu}} \tag{2.4}$$

A sum of all individual magnetic moments, μ , leads to a net magnetization, $\vec{M}$ polarized along the external magnetic field direction. The external field exhibits a torque on the net magnetization. If the main magnetic field is static, the magnetic moment will try to line up with the direction of the magnetic field. In combination with an angular momentum, precession occurs around the direction of the static field at the Larmor frequency. The strong magnetic field, with typical clinical field strengths of 1.5 T up to 7 T, the net magnetization can be used to produce an NMR signal.

$$\vec{M} = \sum_i \vec{\mu_i} \tag{2.5}$$

$$\frac{d\vec{M}}{dt} = \gamma \vec{M} \times \vec{B} \tag{2.6}$$

2.1.2 Motion and Relaxation

Molecular motion in the order of picoseconds to the range of tens of seconds are present in the human body because molecules are not resting but vibrating about their mean position. Rotation of small molecules is faster than larger molecules e.g. proteins with picoseconds (former) compared to nanoseconds (latter) time-scale. The molecule rotation's nanoseconds time scale is in the order of the Larmor frequency's time-scale: $\omega_0 \tau_0 \approx 1$, e.g. with sodium at 7 T $1/(2\pi 11.262 MHz/T \cdot 7\,T) \approx 2ns$. NMR has the ability to probe molecular motion. An NMR signal decay is due to two independent relaxation mechanisms: Longitudinal relaxation, by spin-lattice interaction, resulting in a regrowth of z-axis magnetization and the transversal relaxation, by spin-spin interaction, leading to a de-phasing of the transverse signal. Relaxation mechanisms are in the order of ms to tens of seconds. Motions at the same time scale as the Larmor frequency are the reason for the longitudinal, spin-lattice relaxation. Processes faster than Larmor frequency time-scale e.g. vibrations average the spin Hamiltonian before and processes slower than the Larmor frequency average the spin Hamiltonian after an approximation that takes only into account the components along the magnetic field direction and is called secular approximation. Relaxation is governed by the non-secular Hamiltonian terms but the NMR spectrum is governed by the secular Hamiltonian terms. In general the transverse relaxation is much faster than the longitudinal relaxation.
The net magnetization is represented in the three spatial components: $M_i(t)$ with the transverse components i= x,y and the longitudinal component i= z and the sinusoidal

precession. Bloch introduced the nowadays used relaxation time constants T1 and T2 phenomenologically to describe the longitudinal and transversal relaxations:

$$M_x(t) = M_0\, e^{-t/T2}\, sin(\omega t) \tag{2.7}$$
$$M_y(t) = M_0\, e^{-t/T2}\, cos(\omega t) \tag{2.8}$$
$$M_z(t) = M_0\, (1 - e^{-t/T1}) \tag{2.9}$$

Transversal Relaxation - Spin-Spin Interaction - governed by T2
After the magnetization along z-direction has been flipped into transverse plane by an RF pulse, the spins precess. The spin spin interaction leads to de-phasing of the transversal magnetization. The efficiency of this energy exchange determines the value of T2. Mutual dipole dipole interaction leads to the energy exchange. Additionally there is the effect of de-phasing, which is a loss of coherence, because of fluctuating field variations e.g. changes in precession frequency due to infrequent transitions between molecular states. These mechanisms accelerate the relaxation in the transverse plane, how much depends on the exchange rate, with higher exchange rates leading to a more rapid decay and to broader peaks in NMR spectra “motional broadening" up until the point of cross over where the two states for an exemplary two-site exchange, are indistinguishable. For even fast exchanges that occur so fast that spins do no longer accumulate extra phases due to the different environment, the transversal decay starts to slow down again and the NMR peak becomes narrower, “motional narrowing" the limit is given by the average precession of the two sites and only one NMR peak is detected. The amplitude of the transverse magnetization decreases with time (Figure 2.1).

$$\frac{d\vec{M}_{xy}(t)}{dt} = \gamma \vec{M}_{xy} \times \vec{B}_{external} = \frac{-1}{T2}\vec{M}_{xy} \tag{2.10}$$
$$\vec{M}_{xy}(t) = \vec{M}_{xy}(0) e^{-t/T2} \tag{2.11}$$

The energy exchange is most effective for slow molecular motion resulting in solids showing short T2 in contrary to long T2 values in liquids. T2 does not depend on field strength.
Magnetic field inhomogeneities result in slight deviations in the Larmor frequency causing additional de-phasing which is associated with the time constant T2’. The

resulting relaxation is given by the effective relaxation $T2^*$, which is shorter than T2 governed by only the spin-spin interactions.

$$\frac{1}{T2*} = \frac{1}{T2} + \frac{1}{T2'} \tag{2.12}$$

$$\vec{M}_{xy}(t) = \vec{M}_{xy}(0)e^{-t/T2*} \tag{2.13}$$

To measure the T2 constant instead of the T2* a “Spin Echo Experiment" featuring a refocussing π pulse after the excitation pi pulse can be carried out as invented by E.L. Hahn in 1950. However this is not within the scope of this thesis. Typical ^{23}Na T2 values are divided in two components, as will be explained in section **??** and are in the order of 0.5-5 ms(T2fast) and 15-30 ms(T2slow) except for liquids showing a single value in the range of 55-65 ms for the cerebrospinal fluid (CSF). The values were obtained from ultra short echo time experiments to measure the fast component. However a single echo experiment might be unreliable to measure the bi-exponential relaxation curve. [49]

CSF, with the longest values 50-55 ms [49].

Longitudinal Relaxation - Spin-Lattice Interaction - governed by T1
This relaxation is the result of spin interactions, that are averaged over motions faster (and not slower) than the Larmor frequency time-scale. The energy state created by excitation by a RF pulse has limited lifetime, the system relaxes to an anisotropic equilibrium under the external magnetic field. Anisotropic, because there is a net magnetization along the external magnetization which is the basis needed for NMR and MRI. The process can be described by Bloch’s equation:

$$\frac{dM_z(t)}{dt} = R1(M_0 - M_z(t)) \tag{2.14}$$

$$M_z(t) = M_0(1 - e^{-t/T1}) \text{ with } T1 = 1/R1 \tag{2.15}$$

$$\tag{2.16}$$

The energy exchange of the spins happens with the surroundings resulting a re-growth of magnetization along z direction. R1 is the longitudinal relaxation rate and T1 the longitudinal relaxation time (Figure2.1). The T1 depends on the efficiency of energy transport between the spin system and the lattice. These energy exchanges must be stimulated through dipole-dipole interactions between the spins and protons in the environment. Optimal energy exchange occurs when the tumbling of the molecules, depending on temperature, aggregation state and macromolecules, happens at Larmor frequency. This is the reason why the T1 relaxation time is field strength dependent. To measure the T1, the “Inversion Recovery Experiment" is

the gold standard, featuring an initial π pulse before the excitation π pulse. This inversion of magnetization increases the range and multi echo signal acquisition results in the signal recovery curve with zero crossing at T1ln2. However this is not within the scope of this thesis. Typical T1 values for ^{1}H white and grey matter (WM, GM) were measured to approximately 3T: (911 ms WM; 1615 ms GM) and 7 T: (1284 ms WM; 2065 ms GM) [50] ^{23}Na T1 values are much lower with (15-35 ms for WM and GM and the cerebrospinal fluid, CSF, with the longest values 50-55 ms [49].

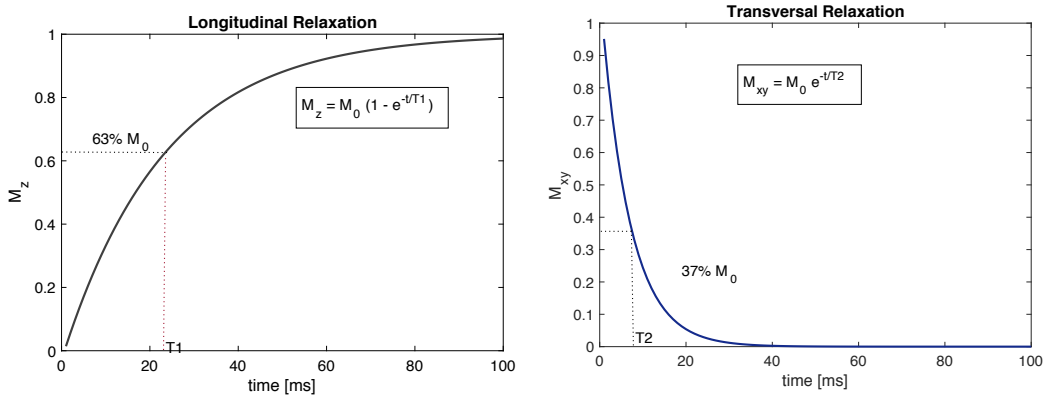

Figure. 2.1: Transversal and Longitudinal Relaxation after an excitation with a $\pi/2$ RF pulse. The two relaxation processes are independent and e.g. the regrowth of the longitudinal magnetization may take longer than the decay of the transversal magnetization. At t=$T_1$63% the magnetization M_z is approximately restored.

The combination of relaxation results in the following combined Bloch equation:

$$\frac{\vec{M}}{dt} = \gamma\vec{M} \times \vec{B}_{external} + \frac{1}{T1}(M_0 - M_z)\vec{e_z} - \frac{1}{T2}\vec{M}_{xy} \tag{2.17}$$

with the solutions:

$$\begin{aligned} M_x(t) &= e^{-t/T2}(M_x(0)\,cos(\omega_0 t) + M_y(0)\,sin(\omega_0 t)) & M_x(\infty) &= 0 \\ M_y(t) &= e^{-t/T2}(M_y(0)\,cos(\omega_0 t) - M_x(0)\,sin(\omega_0 t)) & M_y(\infty) &= 0 \\ M_z(t) &= M_z(0)\,e^{-t/T1} + M_0\,(1 - e^{-t/T1}) & M_z(\infty) &= M_0 \end{aligned}$$

2.1.3 Signal Acquisition

The signal acquisition records the precession of the magnetization vector in the transverse plane. This is achieved by a radio-frequency (RF) coil by means of signal induction. In the simplest case, the induced electric current in the receive coil, is recorded over time, $V_{induced} \propto dM_{xy}/dt$ resulting in a free induction decay signal (Figure 2.2). An RF pulse, in form of a time varying magnetic field, B1, is applied transversally by an RF coil, to interact with the precession of the nuclei. Depending on the time, strength and direction of the applied, radio-frequency (RF) pulse, the net magnetization vector is tipped away from the z-axis to the transverse plane, xy - plane. Most effective is an RF pulse at Larmor frequency acting perpendicular to the B0 field. The maximum signal in transverse plane is achieved by a $\pi/2$ pulse. The flip angle of a static B1 field is given by $\theta = \gamma B1\tau$ with precession frequency $\omega_1 = \gamma B1$. In the Laboratory frame of reference the magnetization is precessing clockwise around the static magnetic field. For easier analyses a rotating frame of reference is often used. In the rotating frame of reference, rotating at the Larmor frequency, there is no longer a precession of the magnetization around the static magnetic field. B0 and B1 field appear static in this frame of reference and the magnetization precesses around the effective magnetic field $B_{eff} = (z(\omega_0 - \omega) + x'\omega_1)/\gamma$. If we are on resonance, $\omega_0 = \omega$ and only a precession about the x' axis remains: $\frac{\vec{M}}{dt} = \omega_1 \vec{M} \times x'$ with $x' = \hat{x} cos\omega t - (\hat{y}\ sin\omega t)$ giving a circularly polarized fields by adding two linearly polarized fields with a phase shift of $\pi/2$.
The signal of a sample in the magnetic field B0 can be described by:

$$s(t) \propto \omega_0 \int d\vec{r}^{\,3}\, e^{-t/T2(\vec{r})} B_{xy}(\vec{r})\, M_{xy}(\vec{r}, t=0)\, e^{i(\Omega - \omega(\vec{r}))t + \Phi_0 \vec{r} - \theta\vec{r}} \tag{2.18}$$

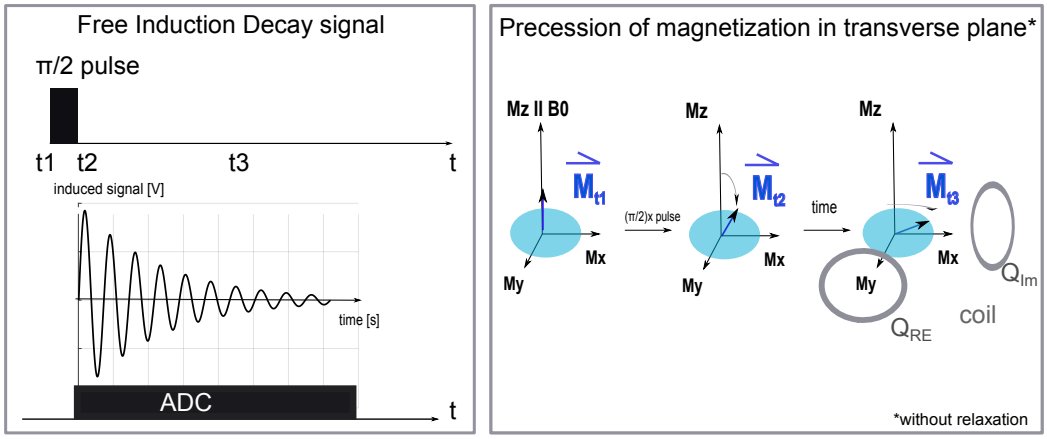

Figure. 2.2: Exemplary free induction decay signal after a $\pi/2$ pulse along acquisition time. On the right: The magnetization is schematically shown for the three time points t1, equilibrium along z direction, t2, flip of the magnetization in transversal plane, and t3, clockwise precession in the laboratory frame of reference. The rotating transversal magnetization, $\vec{M}$, induces a voltage in the perpendicular coil that acquires the signal. Signal acquisition is usually done by quadrature detection, which encodes the signal in complex numbers.

2.1.4 The Nuclear Magnetic Resonance Spectrum

In the easiest NMR experiment, the signal is acquired over time directly after one excitation pulse. By applying a Fourier Transform the time signal is transferred to the frequency domain giving the NMR spectrum. For a sodium nuclei this will lead to a Lorentzian peak at frequency Ω_0. Joseph Fourier described the mathematical relationship between real space and frequency space, known as the Fourier Transform [51]. A complex signal made out of different frequencies can be best analyzed by FT method. Exemplary, this is shown in Figure 2.3 where the a sinusoidal signal that undergoes relaxation is shown for one frequency in Figure 2.3(a) and for two different frequencies in Figure 2.3(b). The spectrum shows that it is much easier to analyze all the signal components in frequency space.

$$S(\vec{k}) = \int d\vec{r}\rho(\vec{r})e^{i\vec{k}\vec{r}} \tag{2.19}$$

$$\vec{k} = \int_0^t \frac{\gamma\delta\vec{G}'}{\delta t'}dt' \tag{2.20}$$

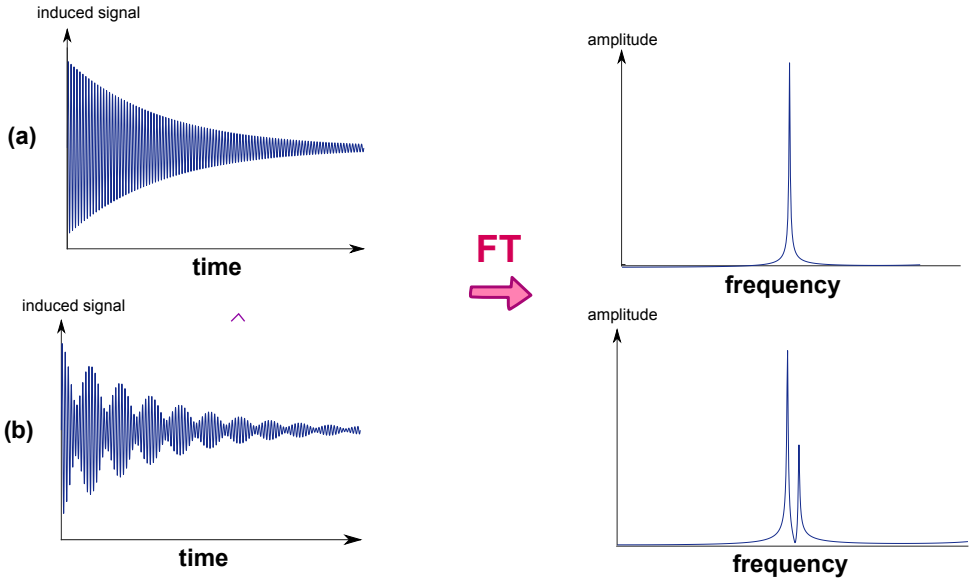

Figure. 2.3: Signal to Spectrum by FT: The connection between the Free Induction decay signal and the resulting spectrum is the Fourier Transform (FT). (a) signal and spectrum for a single frequency (b) signal and respective spectrum for a signal of two overlapping frequencies. Note that only the positive part of the spectrum is shown here.

2.2 Magnetic Resonance Imaging

The Nobel Prize in 2003 for the invention of MRI imaging was awarded in to Sir Peter Mansfield and Paul Lauterbur. In the 1970's they exploited the phenomenon of varying the main magnetic field in the three spatial dimensions, to produce spatially different frequencies which ultimately made it possible to reconstruct images from the body's interior. The differences in hydrogen nuclei in the the different tissues thereby build the basis of the nowadays well known soft tissue contrast in MRI. This undoubtedly was a break through for medical diagnostics and treatments.

2.2.1 Spatial Signal Encoding

Rather than measuring a global signal for a sample, the effective spin density for each voxel separately in the sample is of interest. This can be achieved by changing the precession frequency in space by a gradient. In particular, to the static B0 field, gradients in x, y, z direction are added. The precession frequency ω is then a function of position and time. In the simplest case of a homogeneous B0 field the Larmor frequency ω_0 is constant. Due to the additional gradients the strength of the magnetic field varies in space and this leads to a Larmor frequency that depends on position. Different mechanisms for encoding are differentiated: frequency and phase encoding and slice selection for 2D sequences.

2D Slice Selection

A slice selection Gradient, G_{ss}, is applied usually in z-direction along the sample. The excitation frequency f, has a certain bandwidth (BW) which determines the slice thickness,Δz. Within this band the spins are excited and the obtained signal comes from this slice only. The slice selection gradient is played in time with the excitation pulse. An additional phase is accumulated because of the gradient. To re-phase the signal, a re-phasing gradient is played out directly afterward. An standard pulse shape for slice excitation is a sinc pulse, which is the Fourier pair to a rectangle: f(x) = rect(x) and $F(k) = FT(f(x)) = sinc(k) = \frac{sin(k)}{k}$. The RF pulses frequency content therefore gives the shape of the excited slice. The number of zero crossings of the sinc pulse determines the quality of the profile. $B1(1) \propto sinc(\pi \delta f t)$ with the bandwidthδ f. The number of zeros is given by $N_0 = \delta f / \tau_{rf}$

$$\omega(z) = \omega_0 + \frac{\gamma}{2\pi} G_{ss} z \tag{2.21}$$

$$BW \equiv \Delta f = \frac{\gamma}{2\pi} G_{ss} \Delta z \tag{2.22}$$

$$\Delta z = \frac{BW}{\frac{\gamma}{2\pi} G_{ss}} \tag{2.23}$$

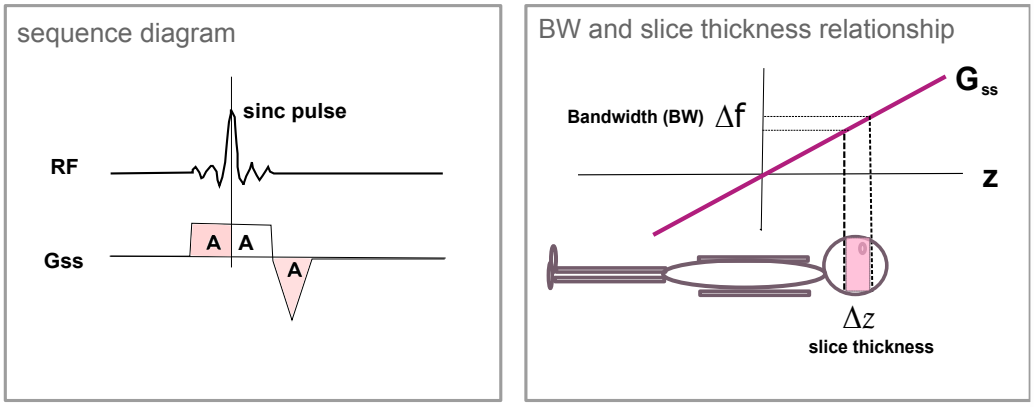

Figure. 2.4: Relationship between the bandwidth of the excitation pulse, here a sinc pulse, and the resulting slice thickness Δz. On the left the pulse sequence is drafted, showing the excitation RF pulse with the slice selecting gradient G_{ss}. On the right the gradient is depicted as linearly increasing over z position. Depending on the gradient steepness a selected Bandwidth results in a 2D slice thickness e.g. for the brain.

Frequency Encoding

$$B(x) = B_0 + xG_f \tag{2.24}$$

$$\omega(x) = \gamma B_0 + \gamma x G_f = \omega_0 + \omega_g(x) \tag{2.25}$$

Frequency encoding is accomplished in analogy to the slice selection by playing out a gradient. This time, the gradient is added during the actual measurement, the “ADC" time. For example, a linear gradient in x-direction G_f results in the Larmor frequency depending on the position x (Figure 2.5). The changing gradient fields applied in the three different spatial directions leads to a unique value of frequency, k, for every point in a sample. The frequency space is called k-space. Data reconstruction to real space is accomplished via Fourier Transform. In a two-dimensional (2D) example, the k-space values, are transformed to a 2D image via a 2D Fourier Transform.

$$M(x,y) = \int_{-\infty}^{\infty} dk_x \int_{-\infty}^{\infty} dk_y S(k_x, k_y) e^{-2\pi i(k_x x + k_y y)} \tag{2.26}$$

Phase Encoding

In a standard imaging sequence, frequency encoding is used for one direction, e.g. anterior posterior, as in Figure 2.5 and phase encoding is used for the remaining direction, e.g. head to foot direction in the image. A gradient is applied before the signal readout. This gradient momentarily changes the frequency of the signal. After the gradient is switched off, the frequency returns to the initial value, but the phase has changed. A phase-shift Φ was accumulated due to the gradient, proportional to its strength and duration of action.[52]

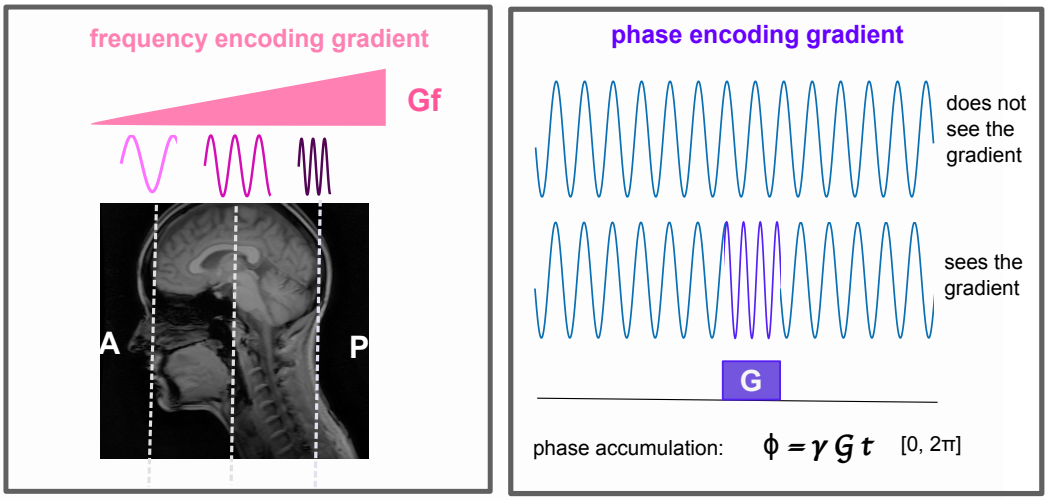

Figure. 2.5: Left: Frequency Encoding. Here on a coronal slice of a head. The frequency encoding direction is shown here in the anterior (A) posterior (P) direction. In this direction the frequency encoding gradient rises and the precession frequency increases with position A→P (anterior to posterior). Right: Phase Encoding. When phase encoding gradient switched on, the frequency changes, after switching off the gradient, the frequency returns to the initial value but the signal has a different phase compared to the signal that has not seen the gradient.

2D Imaging: Example of Gradient Echo Sequence (GRE)

The gradient echo sequence is introduced as one example of an MR imaging sequence. Also, this sequence was used as a basis for the sequence development of the ^{23}Na imaging sequence. A gradient echo sequence consists of one excitation pulse and subsequent gradients for the spatial encoding of the signal in k-space. In Figure 2.6 the sequence diagram shows an excitation pulse in time with the slice selecting Gradient. After this step a 2D plane was selected. Further the first part of the gradient G_x rapidly de-phases the transverse magnetization, M_{xy}. The gradient G_x then switches sign and is usually of double the size to re-phase the signal. This results in a “gradient echo" in the center of the gradient plateau at the echo time TE. The signal strength of the echo depends on the T2* relaxation. The echo time can be controlled by the timing of the de- and re-phasing gradients. The longer the echo time, the higher the T2* weighting of the signal. The gradient G_x encodes one direction in k-space, usually called frequency encoding direction and shown here on the right in direction kx (Figure 2.6). The second direction is encoded by a further gradient, the phase encoding gradient G_y. One run of the sequence with one phase encoding gradient strength, results in one line in k-space. The combination of the positive and negative gradient lobes allows the recovery of the signal loss that came due to the first de-phasing gradient and ultimately the acquisition of positive and negative k-space values. In a multi-echo gradient echo sequence, multiple gradients are applied after the excitation pulse. This leads to a sampling of the signal along the T2* decay. It the T2* relaxation is not strong multiple echos can be used to speed up the measurement time. Also, this method gives the possibility to measure and fit the T2* relaxation parameter.

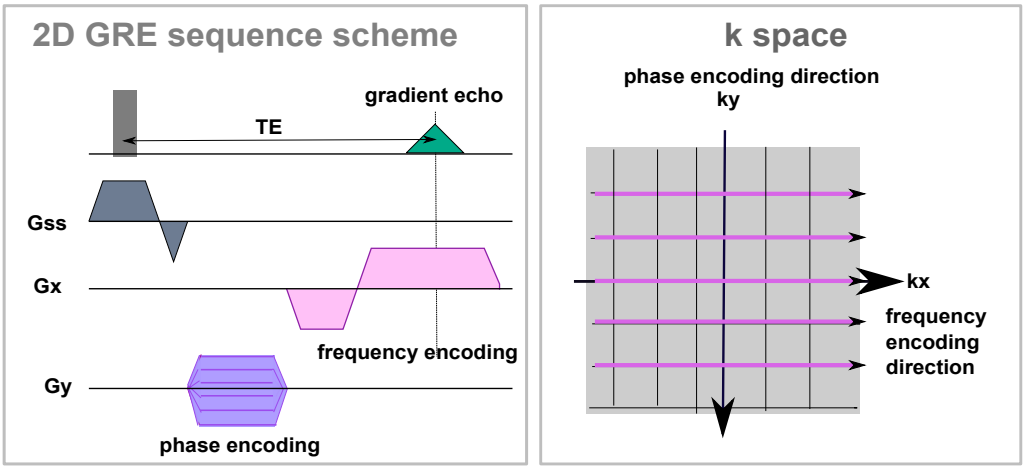

Figure. 2.6: 2D GRE Gradient Echo Sequence, using slice selection, phase encoding and frequency encoding, to spatially encode the signal in 2D k-space. A 2D FFT reconstruction of the k-space results in the desired MRI image.

Image Parameters

Gradients are used for the spatial encoding of the signal. Conventionally the k-space is acquired line by line and the MRI image can be reconstructed by inverse FT of the full k-space data. The position in k-space is determined by the total gradient area given by:

$$k_x = \gamma\, 2\pi \int_0^{\tau} G_x(t)dt$$

$k_x = \gamma\, 2\pi G_x \tau$for a rectangular gradient from t= 0 to τ

The field of view, FOV, of an image depends on the k-space sampling distance and is given by: $FOV = 1/\Delta k$. It is important to chose the FOV larger than the object size, to prevent Aliasing. According to the Nyquist theorem, the sampling frequency should be at least twice the highest frequency of the sample to reproduce the signal exactly at a finite bandwidth:

$$k_{FOV} = 2k_{max} = \frac{N}{FOV} = \frac{1}{\Delta s} \tag{2.27}$$

The same k-space size, determined by k_{max}) but with less sampling points, a higher Δ k, leads to a smaller FOV. However due to k_{max} being the same value, the pixel size does not change.
On the other hand, an experiment with equal Δk but a differing k_{max} leads to the same FOV with a different resolution (pixel size Δs). It is common to artificially increase the resolution by zerofilling Figure2.7. In the development of the imaging sequence in this thesis an asymmetric k-space acquisition was chosen for the first echo in a muli-echo train. This can be seen in Figure 2.7(a). An iterative reconstruction, “projections onto projections onto convex sets (POCS) reconstruction" [53] using a fast algorithm with a non- quadratic regularization constraint to preserve edges and de-noise recovers the k-space values with use of the conjugate symmetry of k-space. The alternative is using zero filling which however results in less information in the image.

Imaging experiments seek to optimize the signal to noise ratio, SNR, in image space. Noise is due to e.g. random fluctuations in the receive coil electronics and the sample itself and is usually uniformly distributed. The SNR can be improved a.o. by averaging multiple acquisitions leading to an improvement factor of $\sqrt{N_{acq}}$. The

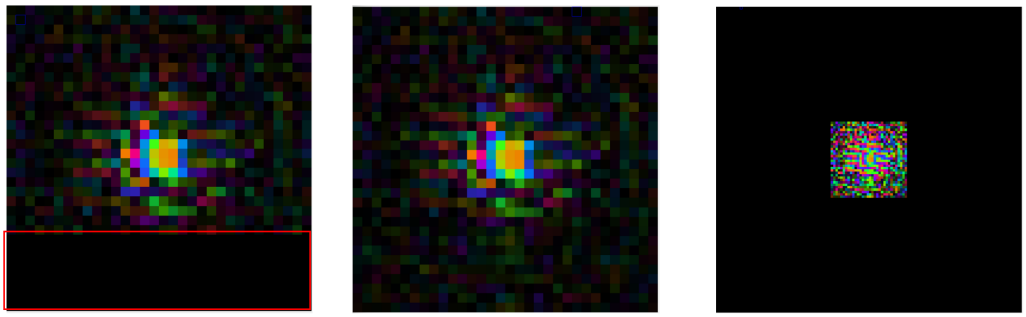

(a) Asymmetric k-space acquisition (b) Reconstruction of missing values with pocs (c) Zero filling to artificially increase resolution (Hamming filtered)

Figure. 2.7: Asymmetric K-Space Acquisition and Zero Filling: (a) the lower part of k-space, marked by the red box, was not acquired (b) after iterative POCS reconstruction the lower part of k-space is filled (c) additional zero filling around the k-space can artificially increase the resolution. It is used in combination with a hamming filter.

SNR is influenced by the bandwidth due to thermal noise and resistance in the coil, the voxel signal and averaging measurements:

$$\frac{SNR}{voxel} \propto \frac{\Delta x \Delta y \Delta z \sqrt{N_{acq}}}{\sqrt{BW/(NxNyNz)}}$$

with $\Delta t = 1/BW$ (2.28)

$Ts = Nx\Delta t$ and sampling time (2.29)

2.2.2 Current X-Nuclei Imaging Sequences

Short echo times of TE $<$500 μs are important to avoid large quantification bias in tissue sodium content (TSC) quantification [54]. In the standard Cartesian gradient echo sequence (GRE) a gradient rewinder is played out before the signal acquisition which allows to travel to outer k-space before the acquiring one full line, compare to Figure 2.6. This gradient hinders a direct acquisition of the signal. and therefore a minimization of the echo time. Non-cartesian sampling schemes were invented, that feature a minimal echo time, because the data sampling starts directly from the center of k-space in a radial lines. The lowest possible echo time is achieved by a nonselective excitation pulse along with ramp sampling on the gradient, this sequence type is called “ultra-short echo time" (UTE) [55].

The density of sampling in k-space may introduce additional noise. The gradient waveform determines the resulting k-space trajectories and hence the filling of k-space and the noise variance. An unbeatable advantage of the Cartesian gradient echo sequence is the perfectly homogeneous sampling of the k-space. The uniform density results in the best noise variance. For a standard radial sequence the density decreases in the higher frequency region, outer k-space, and therefore introduces noise. More sophisticated sampling techniques were introduced to combine homogeneous sampling of k-space with the benefit or ultra short acquisition time. Due to improvements of the gradients' hardware over the recent years, variable gradient waveforms have become possible. Aside from the standard Cartesian GRE sequence, there are currently four main methods that employ different gradient waveforms to sample the data in k-space: radial acquisition (RAD) [56], twisted projection imaging (TPI) [57, 58], density adapted 2D and 3D radial acquisition (DA-RP) [59] and cones (CON) [60, 61, 62, 63]. With the sampling method of twisted projection imaging it was possible to achieve an analytically derived dense sampling of k-space with a radial sequence. Longer readout times per RF excitation pulse seem like one idea for improved k-space coverage. However, this will impose a T2-weighting on the data which is not favorable, and overall the fast bi-exponential decay limits the readout time. To solve this issue, a spectral weighting function was introduced for the TPI sampling scheme to decrease the sampling density at high spatial frequencies. This reduces the readout time and therefore mitigates T2 signal attenuation for the high spatial frequencies [64, 65, 66, 55]. TPI-SENSE further allows for scan time reduction by undersampling [67, 68, 69]. The density adapted radial acquisition (DA-RP) enables uniform k-space sampling on radial spokes. By changing the gradient waveform such that the gradient strength is high in the k-space center and after a plateau the gradient strength decreases resulting

in more closely sampled points in outer k-space. 3D and 2D sampling methods have been established. Trajectories were optimized by golden angle acquisition which is favorable in motion sensitive regions [59, 70, 32]. Cone shaped k-space acquisitions have the flexibility of a nonuniform field of view along with an SNR efficient reduction of scan time. The trajectories are favorable in terms of SNR and aliasing problems compared to 3D radial sequence. The “FLORET" trajectory uses Fermat’s spirals that are projected onto the surface of a unique cone, determined by the cone angle. The trajectory design was shown to be comparable to DA-RP and density compensated cones trajectory. [62, 63] Acquisition weighted stack of stars samples data in k-space in form of stack of stars enabling a nonuniform FOV that facilitates high in-plane resolution with increased slice thickness.[61] Eddy currents can be a problem of variable gradient waveforms that lead to deviations from the nominal trajectory [71]. Older gradient systems might not facilitate the fast gradient switches and peak strengths that are necessary for non-uniform sampling methods with high resolution.

Comparison of the trajectories

Performance of the different sequences (TPI, DA-3DRP, RAD, CON, GRE) was compared by [72] at 9.4 T. Additionally, they compared the resulting point spread function (PSF) for the different trajectories without relaxation by taking the inverse Fourier transform. Without relaxation the Cartesian gradient echo sequence gave the best PSF followed by the TPI readout, cones, DA-3DRP and lowest the RAD. Streaking artifacts were observed for the density adapted radial readout. Further, the radial readout requires more projections for an acquisition in radial spokes compared to the TPI scheme. The TPI method needs less projections to homogeneously sample k-space and therefore a time advantage is given. Comparison in image space yielded similar results for the TPI and DA-RP sequence. The standard radial sequence, without density adaptation, and acquisition in cones reported problems in areas of off-resonance.

Reconstruction

Reconstruction of the data from k-space to image space is standardly done by Fourier Transform (FT). However, for radial acquisitions the standard FT cannot be directly applied and for radial acquisitions a cumbersome reconstruction is needed. Currently there are three main methods for reconstruction: gridding with inverse FT [73], non-uniform FT and iterative methods. Sampling density compensation affects the non-cartesian image reconstruction and has to be taken into account [74, 75]. For spiral acquisition schemes de-blurring methods were reported [76, 77]. Using prior information of proton images for SNR improvement was proposed by [78]. A self-gating method for lung imaging based on center of k-space data [79].

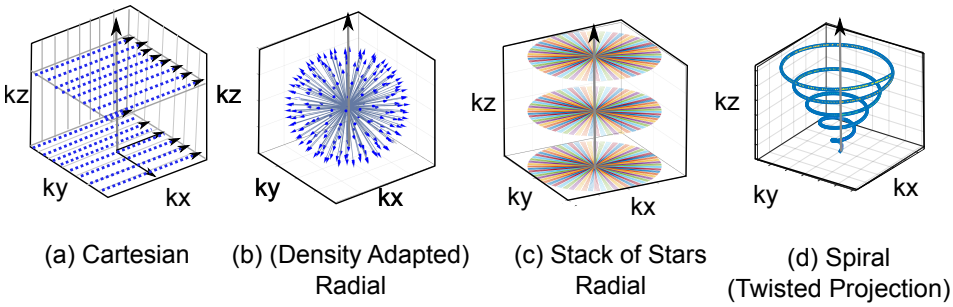

(a) Cartesian (b) (Density Adapted) Radial (c) Stack of Stars Radial (d) Spiral (Twisted Projection)

Figure. 2.8: XNuclei kspace trajectories: Currently used different sampling schemes for acquisition of single-quantum coherence images

Deep convolutional neuronal networks have achieved impressive results in the field of image reconstruction for proton MR images. Reuse of ideas for the reconstruction of sodium radial images could improve current image quality. Current and important multi-quantum ^{23}Na sequences will be presented in detail in part II, by simulation (Section 5).

2.2.3 Spin Hamiltonian

To describe the dynamics of the nuclear spin, the time-dependent Schrödinger equation is used with the wave function describing the quantum states of the spins and the Hamiltonian describing all interactions in the system. However for the use in NMR the description of only the nuclear spin states and the nuclear spin Hamiltonian suffices.

$$\frac{d}{dt}\left|\Psi_{spin}(t)\right\rangle \approx -i\hat{\mathscr{H}_{spin}}\left|\Psi_{spin}(t)\right\rangle \tag{2.30}$$

$$\text{with} \mathscr{H}_{spin} = \mathscr{H}_{spin}^{electric} + \mathscr{H}_{spin}^{magnetic} \tag{2.31}$$

The terms of the nuclear spin Hamiltonian only depend on the directions of the nuclear spin polarizations. Electrons are moving very rapidly so that the nuclei are affected by a time average of their generated fields, therefore a simplification called “spin Hamiltonian hypothesis" only considers the average magnetic and electric effect of electrons. The other way around, the nuclear spin energies are not enough to influence the electronic motions. However, this remains a simplification because even for the effect of longitudinal relaxation, where relaxation ends in an asymmetric equilibrium state with a net magnetization along the external magnetic field direction, an influence of the nuclear spin states on the motion of molecules is needed.

Electromagnetic interactions of nuclei with their environment in form of translations or rotations occurs, because of their electric charge interacting with electric fields and their magnetic moment interacting with magnetic fields. The effect of rotational motions of the nuclei with their magnetic moment and surrounding electrons in the external fields are important mechanisms for NMR. The Hamiltonian has two parts in general, the electric spin Hamiltonian and the magnetic spin Hamiltonian which give the changes of the nuclear electric energy and nuclear magnetic energy with rotation of the nucleus. The charge distribution of nuclei is not necessarily spherical and can be decomposed in multipole components written as superposition: $\mathscr{C}(\vec{r}) = \mathscr{C}^0(\vec{r}) + \mathscr{C}^1(\vec{r}) + \mathscr{C}^2(\vec{r}) +$ higher orders. The components are, the spherical (total electric charge) plus dipolar(electric dipole moment) plus quadrupolar(electric quadrupolar moment) component, etc. Nuclei are in an electric environment given by an electric potential. The electric potential V(r) can also be represented as a superposition: $V(\vec{r}) = V^0\vec{r} + V^1\vec{r} + V^2\vec{r}...$ with the first term giving the electric charge at the center of the nucleus and the the second component giving the electric

potential gradient and the third giving the gradient of the electric potential gradient which quals the the gradient of the electric field (denoted EFG). A symmetry property links the nuclear shape to its nuclear spin, I: $\mathscr{C}^n(\vec{r}) = 0$ for n > 2I. This has the effect, that independent of the electrical environment, the nuclear electric energy of spin 1/2 nuclei is independent of the spatial orientation of the nucleus and the spin 1/2 nucleus can be represented by a spherical shape. The electric interactions vanish for spin 1/2 nuclei, giving $\mathscr{H}_{spin}^{electric} = for\, I = 1/2$. However, for spin 3/2 nuclei, charge is distributed asymmetrically and the nuclei's electric energy depends on its orientation with respect to the field. The main electric term is the interaction of the electric quadrupole moment with the surrounding EFG and the electric part of the hamiltonian is: $\mathscr{H}_i^{electric} = \mathscr{H}_i^Q$, for $I \geq 1$ and for a nuclei i.

Magnetic interactions

The nuclear magnetic dipole moment is given by the multiplication of the gyromagnetic ratio and the spin angular momentum, for a nuclei i:

$$\hat{\mu}_i = \gamma_i \hat{I}_i \tag{2.32}$$

The energy can be described by the magnetic Hamiltonian and depends on the magnetic field and the gyromagnetic ratio:

$$\mathscr{H}_i^{magnetic} = -\hat{\mu}_j \cdot \vec{B} \tag{2.33}$$

The energy is minimized, when the magnetic moment aligns with the magnetic field.

In summary, the nuclear spins experience electric and magnetic fields from the MRI system (external interactions) and their position in matter (internal interactions). The external interactions are magnetic in MRI and NMR due to the applied magnetic fields and are much stronger than the internal interactions and can be expressed by the external Hamiltonian, summed over all nuclei i in the sample:

$$\hat{\mathscr{H}}_{external}(t) = \hat{\mathscr{H}}_{static\,B0\,field}(\vec{r},t) + \hat{\mathscr{H}}_{gradients}(\vec{r},t) + \hat{\mathscr{H}}_{B1\,RF fields}(\vec{r},t)$$

with the nuclear Zeeman interaction:

$$\hat{\mathscr{H}}_{static\,B0\,field} = -\gamma B_0 \hat{I}_z$$

with the gradient Hamiltonian, exemplary for x direction:

$$\hat{\mathscr{H}}_{gradients}(\vec{r},t) = -\gamma G_x x \hat{I}_z$$

with the transverse component of the RF field:

$$\hat{\mathscr{H}}_{B1\,RF\,fields}(t) = -\omega_{nut}[cos(\omega_r eft + \Phi)\hat{I}_x + sins(\omega_r eft + \Phi)\hat{I}_y]$$

The RF field oscillates at a reference frequency $\omega_r ef$ of the spectrometer when an RF pulse is played out during an NMR or MRI sequence. The nutation frequency $\omega_{nut} = |1/2\gamma B_{RF} sin(\theta_{RF})|$ with maximum amplitude B_{RF}.

For internal interactions, a difference has to be made between the nuclei of different nuclear spin value. Spin 1/2 nuclei show only magnetic interactions because the electric Hamiltonian vanishes. For quadrupolar nuclei with spins greater than 1/2 the quadrupolar interaction remains in the electric Hamiltonian and the interaction overall is magnetic and electric. The internal spin interactions comprise chemical shift, quadrupolar couplings, dipole-dipole couplings and J-couplings which will not be discussed in detail. However it should be noted that the quadrupolar coupling in the internal, electric Hamiltonian, which vanishes for spin 1/2 nuclei, has the greatest magnitude and the greatest internal effect for spin$>$1/2 nuclei.

2.3 Quadrupolar Nuclei

Quadrupolar nuclei are nuclei with spin greater than 1/2. The nuclear spin of even mass isotopes exhibit an integer spin. If moreover, there are as many protons as neutrons in the nuclei, the ground state nuclear spin is I=0. This is the case for ^{16}O. Spin 0 nuclei are NMR silent. If number of protons and number of neutrons are both an odd number, the nuclear ground state spin is greater than zero, e.g. deuterium ^2H with one proton and one neutron has ground state spin 1. Odd mass numbers lead to have-integer spin.

The sodium nucleus with spin I = 3/2 belongs in the group of nuclei of I $>$ 1/2, that exhibit an electric quadrupole moment. It is positively charged with 11 protons and 12 neutrons in the nucleus and with 10 electrons in the shells around it. The electric quadrupole moment leads to an additional strong interaction of the nuclear electric quadrupole moment with the local electric field of the surrounding which is given by the electron clouds of e.g. molecules in biological material. As the field of quadrupolar nuclei is in itself large, the focus of this section lies on the main concepts important for understanding the behavior of sodium nuclei (in biological environments). The electric quadrupole moment of $^{23}Na^+$ is $10.4/10^{-28}m^2$. Although this magnitude is rather large, it does not give directly the electric quadrupole

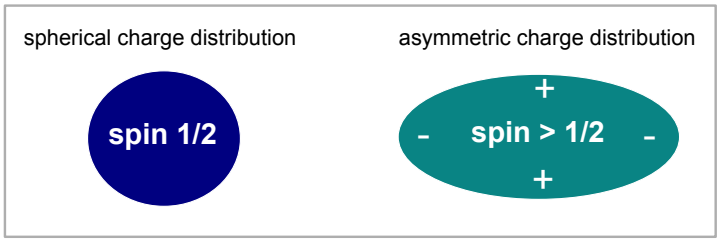

Figure. 2.9: In contrast to spherical charge distribution of spin 1/2 nuclei, spin >1/2 nuclei exhibit an asymmetric charge distribution. The quadrupole does not couple to a symmetric field in contrast to a dipole. For spin 1/2 nuclei interaction with the electric field gradient (EFG) is independent of direction whereas for spin >1/2 the EFG interacts with the quadrupolar nuclei. The strength of interaction depends on the quadrupolar moment.

interaction because the external molecules generating an asymmetry in the electric field are needed. In a symmetric environment, such as liquid saline solution there is no quadrupolar coupling. The resonance frequency, $\omega_0 = \gamma B_0$, depends on the respective nuclei with the gyromagnetic ratio. The value for sodium is $\gamma(^{23}Na) = 11.279$ MHz/T, the value for protons is four times higher with $\gamma(^1H) = 42.577 MHz/T$. The electric field gradient tensor at each nuclei site has principal values in the three symmetry axes, which sum to zero: $[V_{XX} + V_{YY} + V_{ZZ} = 0$. The tensor, **V**, can then be described by the 'largest principal value' eq and the bi-axiality in range of 0 to 1, of the tensor at the point of nucleus:

$$\eta_Q = \frac{V_{XX} - V_{XX})}{V_{ZZ}} \quad \text{anisotropy parameter} \quad 0 \leq \eta \leq 1$$

$$V(\Theta) = R_Q(\Theta) \cdot \begin{pmatrix} V_{XX} & 0 & 0 \\ 0 & V_{XX} & 0 \\ 0 & 0 & V_{ZZ} \end{pmatrix} \cdot R_Q(\Theta)^{-1}$$

with $R_Q(\Theta)$, a 3x3 rotation matrix, describing the orientation of the static magnetic field to the electric field gradient. ζ is the molecular orientation angle.

2.3.1 Nuclear quadrupole Hamiltonian

$$\hat{\mathscr{H}}_Q(\Theta) = \frac{eQ}{2I(2I-1)\hbar} \hat{I} \cdot V(\Theta) \cdot \hat{I}$$

In the case of sodium nuclei in biological environment the quadrupolar interaction is much smaller than the Zeeman interaction. The first order Hamiltonian is a sufficient approximation to describe the system:

$$\hat{\mathscr{H}}_Q^{(1)} = \omega_Q^{(1)} \times \frac{1}{6}(3\hat{I}_z^2 - I(I+1)\hat{1})$$

with the 1^{st} order quadrupolar coupling $\omega_Q^{(1)} = \frac{3\pi C_Q}{(2I(2I-1)}(3cos^2(\theta_Q - 1))$

Q = quadrupolar moment, I = nuclear spin, $C_Q = e^2qQ/h$ quadrupole coupling constant, $\hat{1}$ is the unity operator.

In isotropic liquids, there is no quadrupolar coupling between the nuclei and the external electric field gradient ($\omega_Q^{(1)} \approx 0$). The motional average of the 1st order quadrupolar Hamiltonian is in this case zero: $\hat{H}_Q^{(1)} = 0$.

In contrast to quadrupolar coupling, dipole-dipole coupling is the main interaction process in ^{1}H MR, which is a constant and does not depend on the molecular orientation.

Electric Quadrupole Coupling

The dynamics of the system, constituted of isolated and noninteracting sodium nuclei, can be quantum mechanically described in the form of eigenstates. According to quantum theory, spin 3/2 nuclei exhibit 4 eigenstates. With application of a magnetic field, splitting occurs into the four Zeeman eigenstates: +3/2, +1/2, -1/2, -3/2.

Spin Hamiltonian: $\hat{\mathscr{H}}^0 = \omega_0\hat{I}_z$, with $\omega_0 = -\gamma B^0(1+\delta)$

$$\hat{I}_z \left|\frac{3}{2}, m\right\rangle = \hbar m \left|\frac{3}{2}, m\right\rangle$$

$$\hat{I}^2 \left|\frac{3}{2}, m\right\rangle = \hbar I(I+1) \left|\frac{3}{2}, m\right\rangle$$

Transitions between states $\frac{3}{2} \leftrightarrow \frac{1}{2}$ and $-\frac{1}{2} \leftrightarrow -\frac{3}{2}$ are called satellite transitions, while the remaining transition between the two inner energy levels: $\frac{1}{2} \leftrightarrow -\frac{1}{2}$ is called central transition. The Zeeman eigenstates $\left|\frac{3}{2}, m\right\rangle$ are eigenstates of the quadrupolar Hamiltonian. Therefore, if the quadrupolar coupling is not positive and does not average over timescale of inverse larmor frequency, then the equidistantly spaced energy levels of the Zeeman splitting are shifted. Specifically, the $\pm$3/2 states are shifted up whereas the $\pm$1/2 states are shifted down.

$$\hat{\mathscr{H}}_Q^{(1)} \left|\frac{3}{2}, m\right\rangle = E \left|\frac{3}{2}, m\right\rangle$$

$$\hat{\mathscr{H}}_Q^{(1)} \left|\frac{3}{2}, \pm\frac{3}{2}\right\rangle = +\frac{1}{2}\omega_Q^{(1)} \left|\frac{3}{2}, \pm\frac{3}{2}\right\rangle$$

$$\hat{\mathscr{H}}_Q^{(1)} \left|\frac{3}{2}, \pm\frac{1}{2}\right\rangle = -\frac{1}{2}\omega_Q^{(1)} \left|\frac{3}{2}, \pm\frac{1}{2}\right\rangle$$

2.3.2 Coherence Orders and Populations

The density matrix describes the state of a system. In the thermal equilibrium the density matrix elements are determined by Boltzmann distribution. The 12 off-axis elements correspond to the coherences. Coherences are not present in the equilibrium state. Thermal equilibrium is the starting point in any NMR and MRI experiment, where a sample is put into the static magnetic field. At this point, the coherences between the states are zero. Populations are real, diagonal elements of the density matrix ($\rho_{ii} = |i\rangle \langle i|, i = 1, 2, 3, 4$), with coherence order zero. The Zeeman populations are in the diagonal elements which are determined by the Boltzmann distribution. The lower energy state is favorable and therefore higher populated, in case of positive gyromagnetic ratio γ. The populations sum to 1: $\sum_i \rho_{ii} = 1$.

$$\rho = |\Psi\rangle \langle\Psi| = \begin{pmatrix} \rho_{11} & \rho_{12} & \rho_{13} & \rho_{14} \\ \rho_{21} & \rho_{22} & \rho_{23} & \rho_{24} \\ \rho_{31} & \rho_{32} & \rho_{33} & \rho_{34} \\ \rho_{41} & \rho_{42} & \rho_{43} & \rho_{44} \end{pmatrix}$$

=

$$\begin{pmatrix} \rho_{11} & SQC & DQC & TQC \\ SQC & \rho_{22} & SQC & DQC \\ DQC & SQC & \rho_{33} & SQC \\ TQC & DQC & SQC & \rho_{44} \end{pmatrix}$$

The off-diagonal elements give the coherences, with SQC, DQC and TQC the single-, double-, and triple-quantum coherences for the kets $|-3/2\rangle, |-1/2\rangle, |+1/2\rangle, |+3/2\rangle$ and bras $\langle -3/2|, \langle -1/2|, \langle +1/2|, \langle +3/2|$.

$$\rho_{ij}^{thermal\ equilibrium} = \delta_{ij}$$

$$\rho_{ii}^{thermal\ equilibrium} = \frac{e^{-\hbar\omega_i/k_BT}}{\sum_j e^{-\hbar\omega_{ij}/k_BT}}$$

$k_B = 1.38066x10^{-23}J/K$ is the Boltzmann constant and the thermal energy k_BT is in the order of $4x10^{-21}$J.

Coherences between energy levels can be probed. Coherences are complex and each pair $(\pm1, \pm2, \pm3, \pm4)$is connected by complex conjugate. Also, density operators are hermitian and therefore coherence transfers happen in pairs. The four energy levels (denoted $|i\rangle$, with i= 1,2,3,4) have distinct angular momenta:

$$\hat{I}_z |i\rangle = \hbar m_i |i\rangle$$

Coherence orders, p, of non interacting spin $^3/_2$ spins can have the coherence levels of -3, -2, -1, 0, 1, 2, 3, denoted in the following way:

$$
\begin{aligned}
p_{41} &= m_4 - m_1 = +\frac{3}{2} - \left(-\frac{3}{2}\right) = +3 \\
p_{31} &= m_3 - m_1 = +\frac{1}{2} - \left(-\frac{3}{2}\right) = +2 \\
p_{12} &= m_1 - m_2 = -\frac{3}{2} - \left(-\frac{1}{2}\right) = +1 \\
p_{21} &= m_2 - m_1 = -\frac{1}{2} - \left(-\frac{3}{2}\right) = -1 \\
p_{13} &= m_1 - m_3 = -\frac{3}{2} - \left(+\frac{1}{2}\right) = -2 \\
p_{14} &= m_1 - m_4 = -\frac{3}{2} - \left(+\frac{3}{2}\right) = -3
\end{aligned}
$$

For example, for the spin 1/2 system a coherence between the up and down state means that there is a net spin polarization perpendicular to the magnetic field B_0. The difference in the +1/2 ($|\uparrow\rangle$) and -1/2($|\downarrow\rangle$) population gives the net spin polarization along the direction of the magnetic field, which occurs e.g. when a sample with hydrogen ions enters the static magnetic field of an MRI scanner. The complex coherences can be written as magnitude and phase values ($p_{ij} = |\rho_{ij}| \exp\{i\Phi\}$) where the phase gives the direction of the transverse spin polarization. The phase of the coherence level -1 corresponds to the angle of the polarization of the transverse magnetization. Not individual spins are polarized in the "up" and "down" state. Most of the spins are in a superposition of the two states: $\frac{1}{2}\left(\sqrt{|\uparrow\rangle \pm |\downarrow\rangle}\right)$. As coherence levels appear in pairs, the +1 coherence level always accompanies the -1 coherence level but is often neglected because it does not carry extra information. Comparing energy differences, given by $\omega_0 = -\gamma B_0 \approx 1.4610^{-}32J$ for protons at 3T. The difference in energy between the Zeeman eigenstates is much smaller than the thermal energy the population difference in thermal equilibrium is small:

$$
\rho^{1H}_{equilibrium} \approx \begin{pmatrix} \frac{1}{2} + \frac{1}{4}\mathbb{B} & 0 \\ 0 & \frac{1}{2} - \frac{1}{4}\mathbb{B} \end{pmatrix}
$$

with the Boltzmann factor $\mathbb{B} = \dfrac{\hbar\gamma B_0}{k_B T}$. The approximation is valid for temperatures above a few Kelvin.

2.3.3 Irreducible spherical tensor operators for spin 3/2

An equivalent way to describe and follow the change of the density operator and Hamiltonians of spin 3/2 nuclei is the irreducible spherical tensor operator basis, written$T_{nm} = T_{rank,\,order}$, with the coherence order denoted by m. For this thesis the tensor basis is solely used in the coherence transfer graphs as the goal of this thesis was to present an easy to understand formalism (refer to 5) but nevertheless for completeness the tensor description shall be mentioned briefly, following [49]. The spin operators $I_{\pm} = I_x \pm iI_y$ and I_z are used. There are two main points:

1. A nonselective RF can change the coherence order m ($|m| < n$)
2. The rank n changes due to relaxation and effects of quadrupolar coupling (dipolar, J-coupling). The coherence order m stays the same.

There are 16 tensors, given by Table 2.1:

Table. 2.1: Irreducible spherical tensor operators for spin 3/2

T_{nm}	value	definition
T_{00}	1	Identity matrix
T_{10}	I_z	Longitudinal magnetization
T_{20}	$1/\sqrt{6}\ \ (3I_z^2 - I(I+1))$	Quadrupolar magnetization
T_{30}	$1/\sqrt{10}\ \ (5I_z^3 - (3I(I+1)-1)I_z)$	Octopolar magnetization
$T_{1\pm1}$	$\mp 1/\sqrt{2}\ \ I_{\pm}$	Rank 1 SQ coherence
$T_{2\pm1}$	$\mp 1/2\ \ [I_z, I_{\pm}]_+$	Rank 2 SQ coherence
$T_{3\pm1}$	$\mp 1/4\ \ \sqrt{3/10}\ \ [5I_z^3 - I(I+1)\,,\, I_{\pm}]_+$	Rank 3 SQ coherence
$T_{2\pm2}$	$1/2\ \ I_{\pm}^2$	Rank 2 DQ coherence
$T_{3\pm2}$	$\sqrt{3}/4\ \ [I_z, I_{\pm}^2]_+$	Rank 3 DQ coherence
$T_{3\pm3}$	$\mp 1/(2\sqrt{2})\ \ I_{\pm}^3$	Rank 3 TQ coherence

The anticommutator is defined as $[A,B]_+ = AB + BA$. SQ = Single Quantum, DQ = Double Quantum, TQ = Triple Quantum. DQ filtering techniques can detect $T_{2,\pm1}$ and $T_{3,\pm1}$ in matter of residual quadrupolar interaction. However in this case the interesting part is only the $T_{2,\pm1}$ component and a magic angle second, third pulse (54.7°) has to be used. (refer to 5) for the coherence transfer pathway diagram along the three pulses sequence.

Hamiltonians in Tensor basis:

- $\mathscr{H}^0 = \omega_0 T_{10}$ Zeeman Hamiltonian
  with $\mathscr{H}^0 = 0$ in rotating frame

- $\mathscr{H}_Q = \omega_Q \sum_{m=-2}^{+2} (-1)^m F_{2,-m} T_{2m}$ Quadrupolar Hamiltonian
  with $\omega_Q = \dfrac{e^2 qQ}{g\hbar}$
  and $F_{2,0} = \sqrt{3/2}, F_{2,\pm 1} = 0, F_{2,\pm 2} = \eta/2$
  $\eta = \dfrac{V_{xx} - V_{yy}}{V_{zz}} \quad 0 \leq \eta \leq 1$

- $\mathscr{H}_{RF} = \omega_{RF} I_x = \omega_{RF}\ 1/\sqrt{2}\ (T_{1-1} - T_{1+1})$ RF pulse Hamiltonian
  with $\omega_{RF}(t) = \gamma_{Na} B1(t)$

In the rotating frame of reference, at Larmor frequency, the total Hamiltonian is given by: $\mathscr{H} = \mathscr{H}_Q + \mathscr{H}_{RF}$. For ^{23}Na spin dynamics, the Redfield regime is assumed, which results in a second order perturbation theory for the relaxation and an analytical solution. The Debeye model describes the relaxations with the assumption that random EFG fluctuations can be described by one correlation time τ_c on the basis that ions are in a single compartment without exchange.
In human tissue, the following motion regimes are considered:

- $\omega_0 \tau_c << 1$, Isotropic motion with motional narrowing with no quadrupolar interaction (liquids)

- $\omega_0 \tau_c \sim 1$, macromolecuar motion isotropic in the order of the Larmor frequency, quadrupolar interaction dominates. Satellite and central transitions show different relaxation times (e.g. biologic tissue)

- $\omega_0 \tau_c > 1$ Anisotropic motion where a residual quadrupolar interaction is not averaged out over time, depending on the level of the anisotropic motion, the quadrupolar coupling the resulting spectrum ranges from a broadening of the SQ linewidths (human cartilage) to a splitting in central and satellite transitions (liquid crystal).

When exchanges between compartments shall be allowed, the Discrete Exchange Model is used which allows exchange of ions to sites with different quadrupolar properties, which is a more realistic model for biologic tissue but very difficult to analyze in practice. Further complex models exist which remain difficult to interpret and are beyond the scope.

Strong RF pulses for MQ transfer

For the coherence transfer, sequence strong RF pulses $\omega_{RF} \gg \omega_Q$ are needed given for example by rectangular block pulses. A rectangular RF pulse, of a certain amplitude and time duration τ_{pulse} results in a flip angle $\theta = \omega_{nutation}\tau_{pulse}$. With strong pulse no off-resonance effects are assumed which can be fulfilled if the interaction with the RF field is much greater than the chemical shifts and 1^{st} order quadrupolar interaction. For sodium nuclei in biological environment due to small quadrupolar interaction along with a hard RF pulse the condition can be fulfilled. Calculations are done in the rotating frame of reference and the spectrometer of the MRI hardware system has the reference frequency ω_{ref} equal to the frequency of the rotating frame, usually at Larmor frequency. Rotating frame populations are the same as in the fixed frame and the coherences relationship is given by a phase.

The sodium nuclei are the second in the order of NMR signal strength, after protons, in biological tissue although their concentration is about 2000 times lower. Also ^{23}Na sensitivity compared to ^{1}H is only 9.2 %, the gyromagnetic ratio,γ_{23Na}, is only 26% of protons (11 MHz/T compared to 46 MHz/T), resulting in a lower signal to noise ratio (SNR) in the order of 3000-20000. This lower SNR withheld sodium MRI, starting in the 1970s [80, 81], to become a clinical tool so far but with increased available field strengths, up to 7T, as well as double tuned RF coils and better post-processing methods sodium MRI is recently starting to get again increased attention although still remaining a research tool. ^{23}Na MRI has been conducted in multiple organ sites, with the most prominent being brain, cartilage, heart and kidney. Sodium nuclei undergo quadrupolar interaction in solids but this interaction is averaged out in liquids. The regime in the middle, e.g. biological tissue the fluctuating quadrupolar interaction has the effect of a bi-exponential transversal relaxation time, which will be called T2fast and T2slow but is equivalently often called T2short and T2long with values in the order of 0.5-5 ms(T2fast) and 15-30 ms(T2slow) obtained from ultra short echo time experiments. However a single echo experiment might be unreliable to measure the bi-exponential relaxation curve.

3 Methods I: Preclinical at 9.4T - Physiological investigations of ^{23}Na triple quantum signal

3.1 The Three Pulses Sequence - TQTPPI

All data were acquired at field strength of 9.4 T (Biospec 94/20, Bruker, Ettlingen, Germany). We used an in-house built planar single-loop sodium transmit-and-receive surface coil. The following experiments build on the existing knowledge of a three pulses sequence that uses time proportional phase increments (TQTPPI) [82, 37, 38, 29]. It features a simultaneous measurement of all coherences of the ^{23}Na spectrum (Fig.3.1). The spectroscopic sequence is characterized by three subsequent 90° pulses: the excitation, mixing and observation pulses, as well as a 180° refocusing pulse (Fig.3.1). The delay between the excitation and mixing pulse is called evolution time (t_{evo}), the delay between the mixing and observation pulses is the mixing time (t_{mix}). The pulses were repeatedly played out while incrementing the phase of the first two pulses. A 180° pulse between the excitation and mixing pulse was played out to re-focus and increase robustness against B_0 inhomogeneities [29]. A phase-list consisting of 16 entries, each averaging over two successive acquisitions was chosen to cancel out double quantum signals. Although double quantum signals are suppressed, the signal can still be visible at twice the single-quantum frequency due to imperfect pulses with respect to the flip angle and short TR time. The sequence block was repeated while incrementing the evolution time. Phase correction was performed so that the phase cycling in the evolution time domain starts with phase zero. The phase correction value was found by the Fourier transformation of the first FID to yield a spectrum with no phase shift. With this value, all FIDs were corrected before Fourier transformation and reconstruction to an FID along the evolution time domain. A second Fourier transformation results in the TQTPPI spectrum. Sequence parameters are presented in table (3.1).
A nonlinear fit of the signal (Eq.(3.1)) in the evolution time domain was performed [4, 83, 29]. Fourier Transformation of the fitted time signal gives the fitted spectrum in frequency domain. All obtained spectra were normalized to their respective

single-quantum (SQ) peak amplitude signals. We report the triple-quantum peak amplitude signal from the measurement data relative to the SQ signal. Additionally, as well as the amplitudes of triple-quantum (TQ) and SQ single-quantum transition and the T2 long and short component obtained from the fit are reported. We report the triple-quantum peak amplitude signal from the measurement data, as well as the amplitudes of triple- and single-quantum transition obtained from the fit. The nonlinear fit was performed with GlobalSearch in Matlab using fmincon solver to find a minimum of the nonlinear multivariable function [84]. TQTPPI spectra baselines were corrected. The fit error of the variables was approximated by the resulting standard deviation for running the fit 100 times with different starting values.

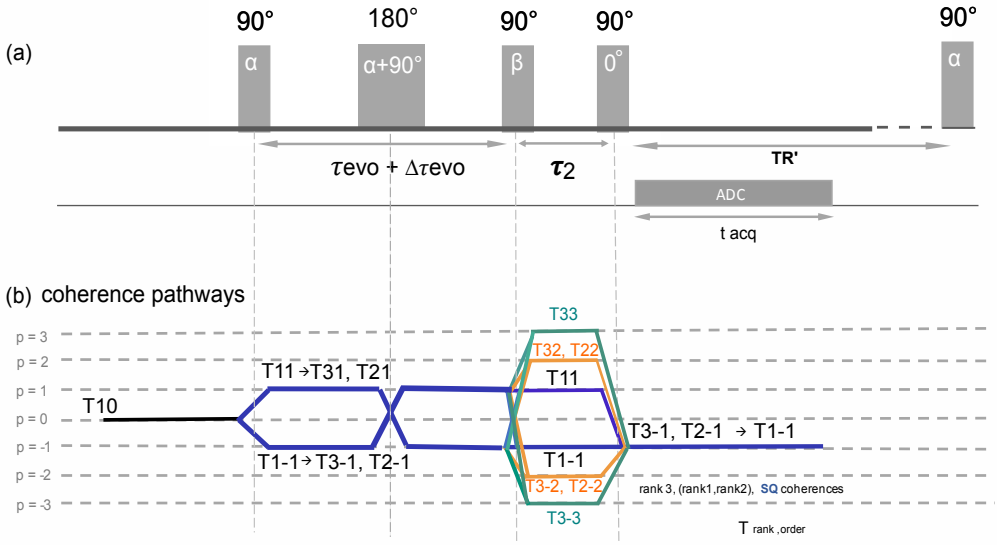

Figure. 3.1: (a) Three $\pi/2$ pulses TQTPPI sequence scheme with a 180° re-focussing pulse between the 1^{st} excitation pulse and the 2^{nd} mixing pulse to mitigate B0 inhomogeneity effects. (b) The coherence pathway scheme (using the tensor description $T_{rank,\,order}$). The starting point is longitudinal magnetization, T10. With the first pulse, the order is changed, from T10 to T11 transversal magnetization. Relaxation and effects as well as quadrupolar coupling can change the rank and e.g. create third order single quantum coherences during the evolution time $\tau_{evo} + \Delta\tau_{evo}$. The mixing pulse then creates a.o. rank three triple-quantum coherences which are made observable by the third $\pi/2$ pulse.

Table. 3.1: TQTPPI sequence parameters

B_0	9.4 T	Acquisition points	2048
TR	140 ms	$t_{acq}^{1stdimension}$	102 ms
$t_{evo}(t=0)$, $\Delta\ t_{evo}$	0.5 ms , 200 μs	BW	20 kHz
90° pulse duration	60 - 160 μs †	t_{acq}	6min
t_{mix}	60 - 160 $\pm$ μs	spectral resolution	3.1 Hz/points
Phase cycles	100	$\Phi_{1,t=0}$, $\Delta\Phi$	90°, 45°

The table states the relevant parameters of the TQTPPI sequence. † The calibration of the transmitter voltage is done before every experiment and depends on the phantom size.

3.2 Development of a Multiparameter Fitting Routine

The TQTPPI signal reconstruction pipeline can be appreciated in Figure 3.2. The data are acquired after each 3-pulses sequence block. Two successive measurements are averaged, carried out with the same phases as for the previous measurement plus a 180° phase difference for the second pulse to suppress DQ signals. The SNR is visibly increased by averaging Figure 3.2. The next step is the first Fourier Transform. The center amplitudes are then plotted against the increasing evolution time to construct the TQTPPI FID. Finally another FT yields the TQTPPI spectrum with TQ and SQ peaks.
The Signal equation for the fit in evolution-time domain is given in Equation [3.1]. A_{SQL}, A_{SQS} are the long and short component amplitudes of the single-quantum, A_{DQ}, A_{TQ} are the respective amplitudes for the double- and triple-quantum signals. Possible phase shifts are accounted for in the phase terms ϕ_i. Long and short component of the T2 relaxation time, T_{2L}, T_{2S}, are fitted. The additional relaxation term with T_D in double quantum part was introduced to achieve a better fit of the not fully suppressed double-quantum transition. The DQ transition showed a broader line shape and appeared phase shifted in the TQTPPI spectrum. Offsets were incorporated by the DC parameter.

$$\begin{aligned} S =& A_{SQL}\ sin(\omega t + \phi_1)\ e^{\frac{-t}{T_{2L}}} + A_{SQS}\ sin(\omega t + \phi_1)\ e^{\frac{-t}{T_{2S}}} + \\ &+ A_{DQ}\ sin(2\omega t + \phi_2)\ (e^{\frac{-t}{T_{2L}}} - e^{\frac{-t}{T_{2S}}})\ e^{\frac{-t}{T_D}} + \\ &A_{TQ}\ sin(3\omega t + \phi_3)\ (e^{\frac{-t}{T_{2L}}} - e^{\frac{-t}{T_{2S}}}) + DC \end{aligned} \tag{3.1}$$

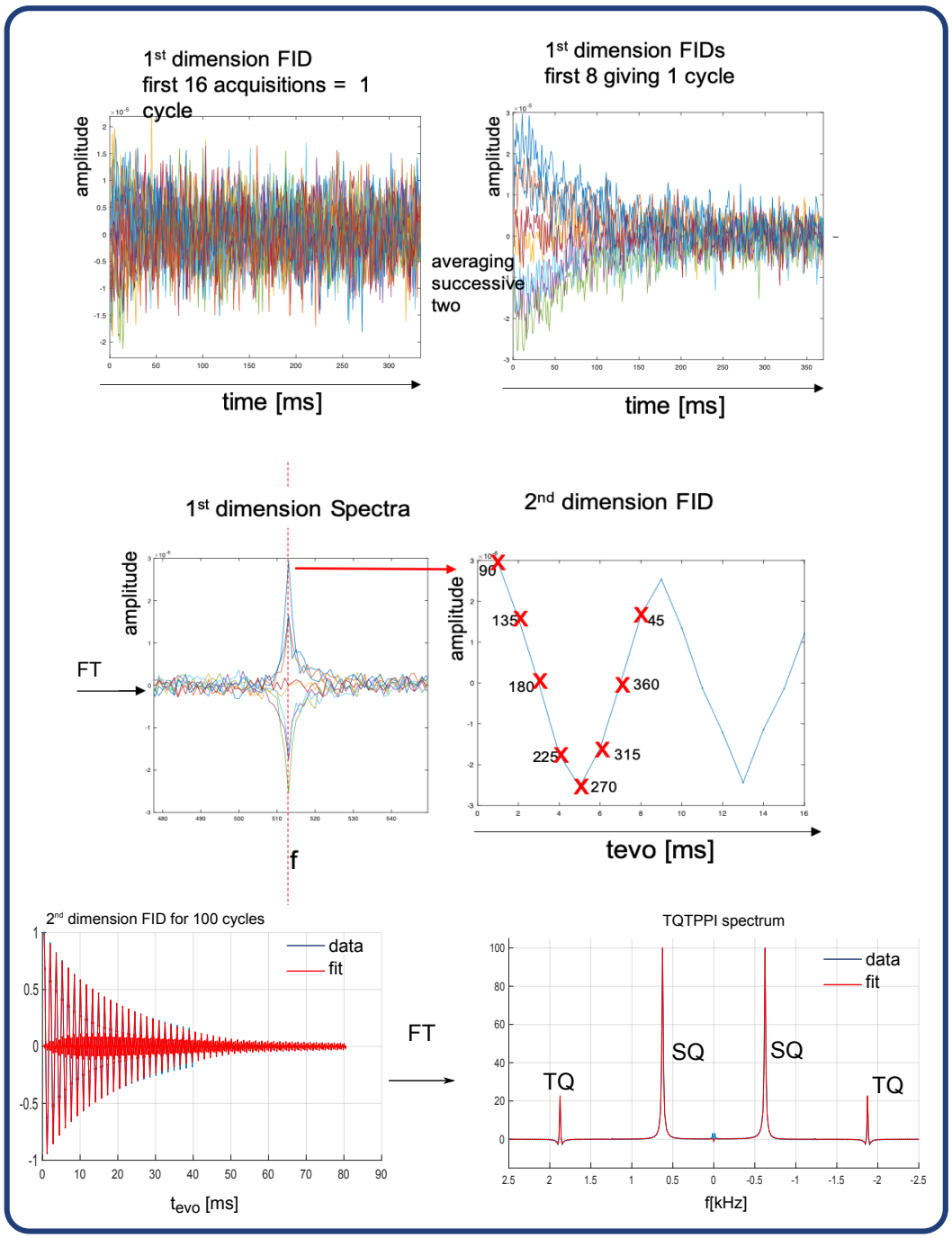

Figure. 3.2: TQTPPI Pipeline and Fit: Upper row: Pipeline steps, for one cycle exemplary. First data before averaging, followed by averaging two successive acquisitions. First Fourier Transform enables evaluation of the center amplitudes, plotted against the increasing evolution time results in the TQTPPI FID. Second row: TQTPPI FID for 100 cycles with Fit. Characteristic TQ signal rise and fall can be appreciated. Finally, second FT yields the TQTPPI spectrum with TQ and SQ peaks. DQ peaks were suppressed by the averaging mechanism.

3.3 Liposomes and Nanoparticles as Cell Phantoms

Cell membrane models in the form of liposomes (II) and nanoparticles (III), comparable in size to cells, provided either a double lipid membrane (liposomes) or a single-layer membrane (nanoparticles). Four different kinds of liposome emulsions, as well as a nanoparticle emulsion were produced, names L1-L4. (Figure 3.3).

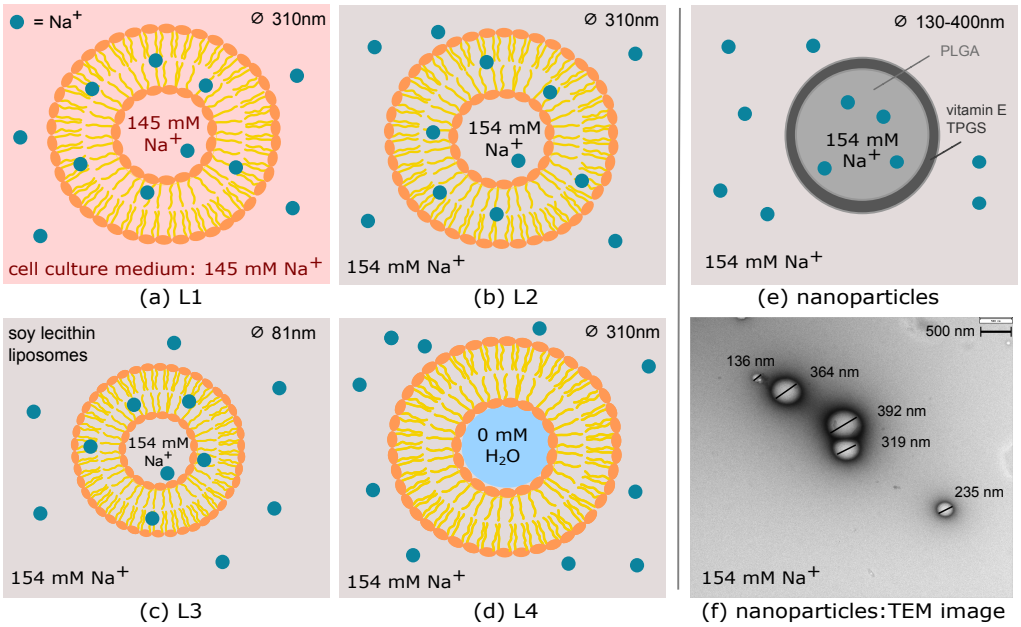

Figure. 3.3: Liposome and Nanoparticle sketches: (a) - (d) Liposome sketches of the double lipid membrane and the sodium ion solution either with MEM cell culture medium,145mM Na^+ solution, or 154 mM Na^+ solution. (e) sketch of the PLGA nanoparticles and (f) Transmission electron microscopy (TEM) image of the produced nanoparticles.

Cell phantom preparation

(a) L1: 145 mM Na^+ MEM inside and outside

(b) L2: 154 mM Na^+ inside and outside

(c) L3: 154 mM Na^+ inside and outside, liposomes from soy-lecithin

(d) L4: 0 mM Na^+ inside with H_2O filling, 154mM Na^+ outside

(e) nanoparticles: 154 mM Na^+ inside and outside

The ingredients for liposome preparation were; 14 ml solution (L1: minimum essential medium (MEM), L2: 154 mM Na^+ solution, L4: H_2O), 310 µL safflower oil, 202 µL glycerin and 1.5 µL vitamin E (Thermo Fisher Scientific) [85]. L3 liposomes were produced from soy lecithin. 100 % pure soy lecithin-granulate was obtained from a local drugstore. 0.2 g soy lecithin was dissolved in 100 ml 154 mM Na^+. For the production of all types of liposomes each solution was stirred for 10min at 5000 rpm. Subsequently, the solution was placed in a sonication bath, alternating between sonication and cooling for one minute each. This procedure was repeated for the duration of an hour to produce stable liposomes. The liposome diameter was obtained by fixed-angle dynamic light scattering (Wyatt Technology, DynaPro Nanostar), to be 310 nm $\pm$ 75 nm for L1,L2 and L4 and 81 nm $\pm$ 46 nm for L3. TQTPPI measurement was performed the following day.

Poly(lactic-co-glycolic acid) (PLGA) nanoparticles encapsulating 154 mM Na^+ solution were prepared following the recipe from [42]. 100 mg of PLGA was used with ethyl acetate as a solvent (1 ml) and Vitamin E-TPGS (141 mg) as an emulsifying agent, diluted in 154 mM Na^+ solution (47 ml). After the production the solution containing the nanoparticles was centrifuged and put into a 2 ml plastic tube with 154 mM Na^+ solution to increase the density of the nanoparticles within the measured phantom. Nanoparticle diameter was measured by transmission-electron-microscopy(TEM) the day after production and resulted in 130-400 nm. TQTPPI measurement was also performed the following day. The diameter of liposomes (310 nm $\pm$ 75 nm) and nanoparticles (200 nm $\pm$ 100 nm) was smaller than the HEP G2 cell diameter, approximately 12 µm [86].

3.4 The MR-compatible Bioreactor System

An MR-compatible bioreactor enabled the measurement of living cells while providing optimal conditions for the cell culture to remain vital. An organotypic 3D culture was obtained by cultivating the cells on a collagen coated microcavity array chip (Fig. 3.4 (b)). The resulting 3D cultures had a thickness of $200\,\mu m$. The collagen coating mimiced the extracellular matrix (ECM) with collagens presenting the majority of the proteins within the ECM [34]. After initial cultivation of the microcavity array chip in an incubator the chip was placed inside the MR-compatible bioreactor (Fig. 3.4). The cell culture specific medium was directly aerated with O_2, CO_2 and N_2. The bioreactor temperature was maintained at 37°C and the medium was steadily renewed by a perfusion pump operating at 0.4 ml/min (Fig. 3.4). Due to the finely tunable conditions concerning temperature, oxygen level and cell medium renewal by perfusion, the bioreactor system provides optimal conditions for cell culture monitoring in MR [44].
With this setup the TQ signal of two main cell lines was investigated by means of the priorly established TQTPPI global spectroscopic NMR method.

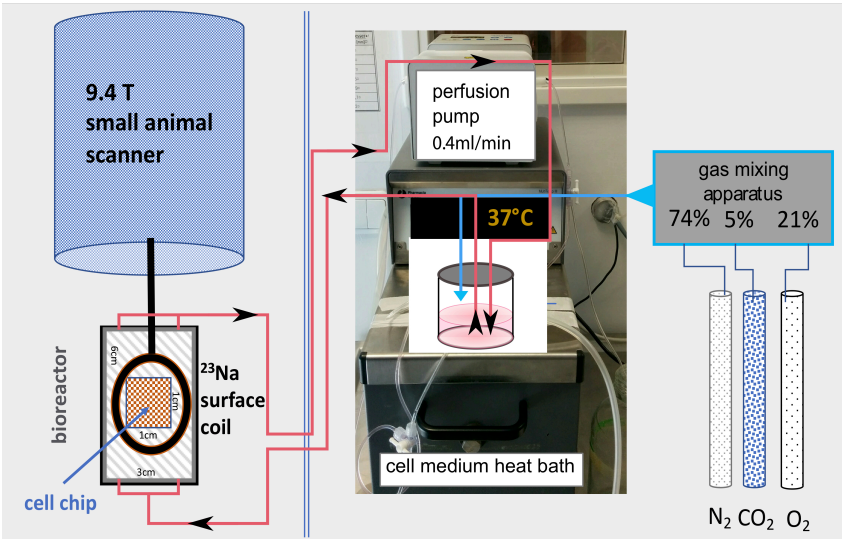

(a)

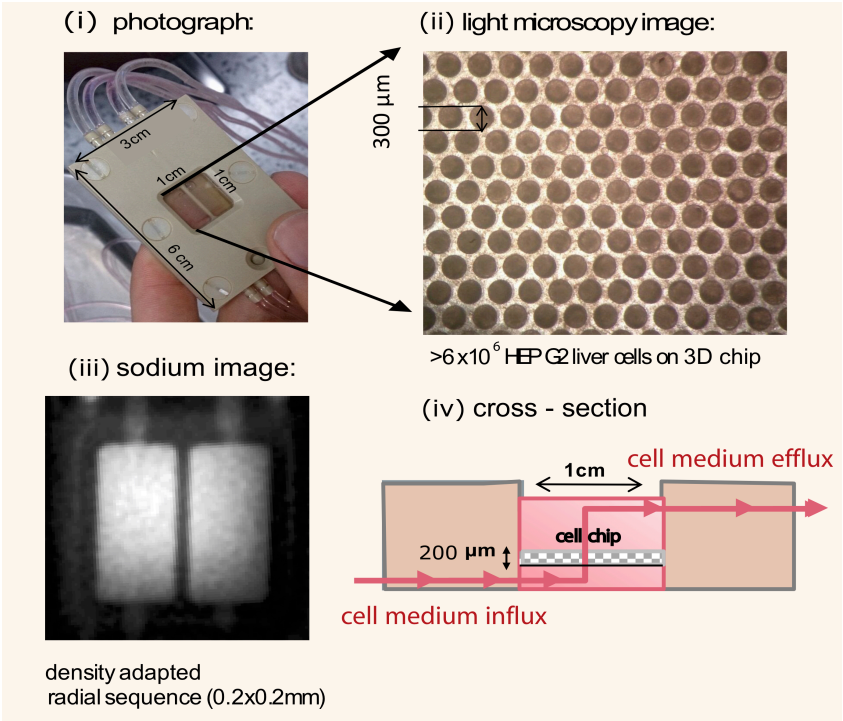

(b)

Figure. 3.4: (a) Experimental setup: The MR-compatible bioreactor is positioned on a heated animal bed. The bioreactor is connected with a system of tubes, leaving the MR room. Outside, the peristaltic pump the heat bath and gas mixing apparatus are positioned. (b) (i) shows the bioreactor. Through the glass window, the microcavity array chip is visible. (ii) under the microscope the cavities filled with cells are visible. (iii) shows a sodium image acquired in the setup using a density adapted radial sequence. (iv) shows the perfusion mode through the bioreactor.

3.4.1 Triple Quantum Signal in Human Liver Cells

Triple quantum (TQ) coherence signal measurement of human HEP G2 liver cells (ATCC, HB-8065, Manassas, VA, USA), over an extended time in an MRI system is challenging. The temperature needs to be maintained and nutrient exchange is important for keeping a cell culture alive over time periods of 1 to 3 days. An MR-compatible bioreactor developed [44] for this purpose facilitated the experiment. Prior to measurement, the cell culture was cultivated on a microcavity array chip (2 days preparation time) and inserted into the bioreactor on the day of measurement. For cultivation a drop containing 6x10^6 HEP G2 cells was placed on a collagenized microcavity chip of size 1x1cm filled with $300\,\mu m$ diameter cavities. Microscope inspection confirmed successful cultivation on the 3D microcavity array. Cell culture medium provided important nutrients and is cell line specific. For HEP G2 cells Minimum Essential Medium (MEM) with L-Glutamine, 10 % FCS (fetal bovine serum) and 1 % penicillin, streptomycin, 1 % glutamax, 1 % essential amino-acids (Thermo Fisher Scientific) was used. The special setup of the bioreactor allows to perfuse the cell medium, heated to body temperature (37°), through the bioreactor and cell chip. The HEP G2 liver cell chip data were measured on three successive days, named “C1" for cells on day one, “C2" for cells day two and “C3" for cells on day three. A perfusion stop experiment was carried out for 9 hours from day 2 to day 3 to simulate the situation of finite glucose, amino-acids and oxygen level (C_{PS}). Additionally the TQTPPI spectrum of a second cell chip was measured, (C4), that is expected to have a dead cell culture due to keeping in hostile environment without cell medium in air for at least 30 minutes at approximately 20 °C. For reference a collagenized chip in cell culture medium was inserted into the bioreactor without any cells and the TQTPPI spectrum was measured (“BR Ref").

3.4.2 Triple Quantum Signal in Neonatal Cardiomyocytes

The sodium-potassium pump plays an important role to maintain the electrochemical gradient across the cell membrane and enable repeated cell contractions which is especially important for the repeated contractions of cardiomyocytes [87]. Cardiomyocytes have a high energy metabolism and feature high endurance, maintained by an increased mitochondrial density resulting in faster adenosin triphosphat (ATP) production. Mitochondria are the cells energy factory. ATP is needed amongst other processes for running the ion exchange of sodium-potassium pump. Therefore, cardiomyocytes are an ideal cell line to study the sodium triple-quantum signal, which might be attributed to sodium-potassium pump activity, in normal conditions

and under stimulation. Human myocardial infarction, is a serious disease where increased tissue sodium concentration (TSC) has been measured by sodium MRI SQ methods in the hope to provide cell viability information [9, 88, 10]. Myocardial infarction is followed by irreversible cell injury if the interruption of blood and hence oxygen flow in the myocardium lasts too long, the result is necrosis of the tissue. Reduced oxygen level in cells has a direct effect on the energy supply which also affects the sodium potassium pump and can result in cell death. Neonatal cardiomyocytes are used to study molecular mechanisms in the heart e.g. the interplay of the two cell types, cardiomyocytes and pacemaker cells, which generate and transfer electrical impulses to neighboring cells [89, 90, 91]. Cell connection and coordinated contraction intercalated disc connections allow diffusion of sodium, potassium and calcium ions. A beta-adrenergic agonist, such as Isoprenaline [92] can be used to stimulate the contraction of cardiomyocytes. TQ signal under normal conditions and stress was studied with the TQTPPI sequence in the MR-compatible bioreactor. Therefore, 10 Mio neonatal cardiomyocytes, were cultivated on two 800 μm diameter micro cavity chips after successful isolation. A bigger diameter micro cavity chip was chosen by previous tests on cultivation of the cardiomyocytes on the cells. By giving more space within each cavity the cells seemed to more easily exhibit coordinated contractions. The cell culture medium for cardiac cells was DMEM (ThermoFisherScientific). After placing the cell culture drop on the chip, the chips rested in an incubator for two days before inspecting them under standard light microscopy. 3D-aggregates formed in the microcavities of the chips and synchronized beating of the cell compounds confirmed viability of the cells. The viable microcavity arrays were inserted into the MR compatible bioreactor for inspection of TQ signal by TQTPPI measurement at 9.4T (Biospec, Bruker, Germany). The same in-house built transmit, receive ^{23}Na surface coil was used as for the HEP G2 liver cells. A sodium image was acquired to verify correct placement of the coil on the bioreactor. TQTPPI signal for 10 Mio cells on two microcavity arrays was measured at 31°C in:

1. Normal perfusion
2. Isoprenaline stimulation
3. Perfusion stop
4. Reperfusion

For stimulation 44.4mg Isoprenaline was added to 35.9 ml 0.9% saline solution to attain a 5mM solution, further diluted 1:5 with cell-medium to achieve a 1mM solution. In 30 ml cell medium 40 μl of the 1 mM solution of Isoprenaline was added. After

the bolus ran through the system(1h), it was diluted in the 100ml overall medium reservoir. Cardiomyocytes stimulation by Isoprenaline was confirmed prior to the experiment on an additional microcavity array with 4 Mio cells and increased beating rate was observed under the microscope.

3.5 Sequence Design for Single Voxel Localization

The TQTPPI sequence is a global spectroscopic method, which can be used to study the sodium metabolism of cells in-vitro with the foremost interest in the occurrence of the triple-quantum signal. This spectroscopic analysis could offer precise knowledge of sodium metabolic processes in pathology versus healthy tissue. To address clinical questions, we aim for transferring this method to in-vivo patient acquisitions where the need for a localization arises. Two different localization strategies, which preserve the quantum coherences, were successfully implemented and tested in-vitro and in-vivo on a rat using a 9.4T small-animal scanner. To address clinical questions, the global TQTPPI method has to be localized. Two different strategies for “Single Voxel Localization" techniques, that preserve the coherence transfer, are presented in the following. An evaluation was done of both sequences on agar-phantoms and in-vivo on a healthy rat.

Sequence Design

The global spectroscopy sequence (TQTPPI) uses triple quantum time proportional phase increments to study the ^{23}Na NMR spectrum, detecting single-quantum (SQ) and triple-quantum coherences (TQ) simultaneously.4 The TQTPPI sequence was extended with three extra 180° block pulses with simultaneous gradients “LOC”. Alternatively, we added a slice selection gradient in time with the first 90° excitation pulse of the TQTPPI sequence and only two additional 180° pulses “LOC-S” (Figure 3.5). Crusher gradients around the localizing gradients were implemented for both sequences. The three spatial directions were used for each crusher and a maximal strength of 15% of the localizing gradient strength was used. The additional pulses were added on purpose after the TQTPPI sequence block to not disturb the three pulses quantum coherence pathway. Additionally, the effect of increased evolution time for optimizing the normalized TQ signal in-vivo and in agar-phantom was investigated. TQS peak height normalized to its respective SQ peak height served as a first qualitative measure.

Data Acquisition

Data were acquired on a 9.4 T small-animal scanner (Bruker, Karlsruhe, Germany) using an in-house-built transmit/receive $^{2}3$Na- surface-coil. An ultra-short echo time sequence was used for agarose phantom to obtain a sodium image for voxel positioning. For in-vivo rat measurement, we acquired a ^{1}H T1 weighted gradient echo image with a volume transmit, receive coil, saving the isocenter position for the $^{2}3$Na- surface-coil.A 45ml agar-phantom, 135 mM $^{2}3$Na with 4% agarose used for initial sequence testing. Subsequently, we tested the localization in-vivo on a

rat, scanned in the head region. Additionally, a phantom stack of 5ml-phantoms containing 6 %, 4 % and 2 % agarose and 154 mM ^{23}Na was measured to investigate the possibility of tracing back agarose content based on TQS values.

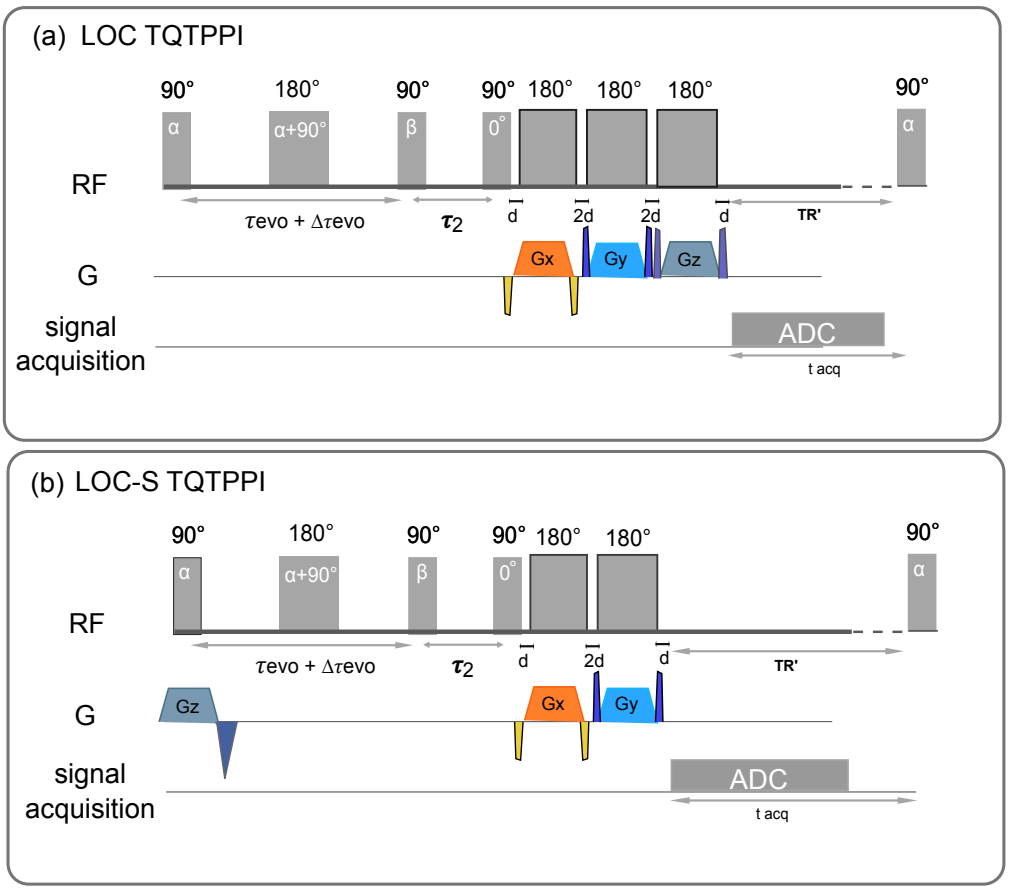

Figure. 3.5: Preclinical Single Voxel Localization of TQTPPI Sequence in two different ways: (a) Three subsequent 180° degree pulses were implemented with Gradients in the three spacial directions: Gx, Gy, Gz. To not disturb the quantum coherence pathway the Localization was done after the global sequence to spoil away all signal not coming from the selected voxel of interest. (b) The second method was done by implementing a slice selection gradient in line with the first pulse, Gz. The two further directions to accomplish the voxel selection were played out after completion of the TQTPPI sequence.

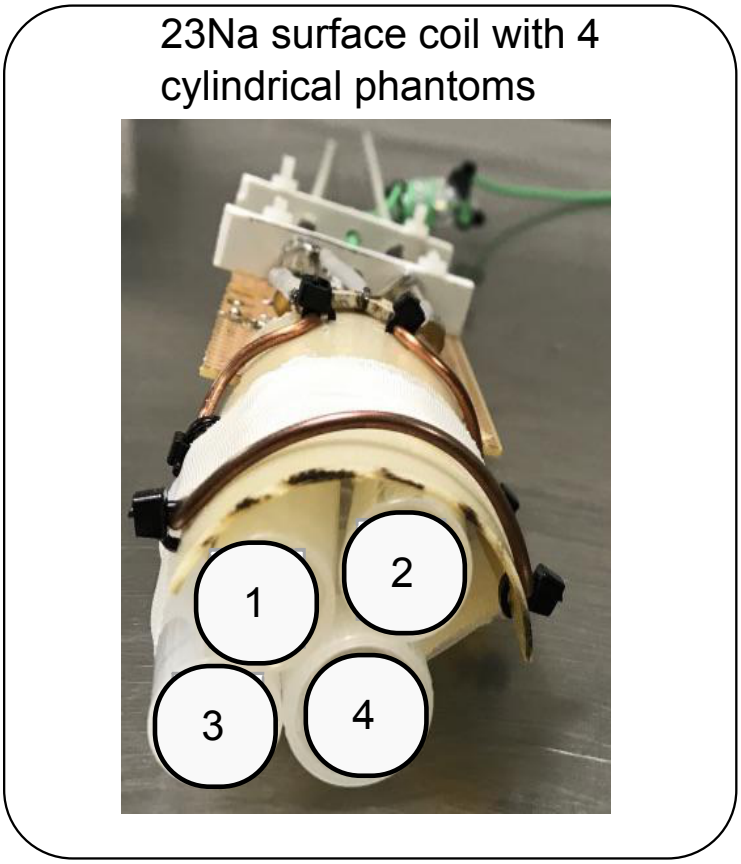

Figure. 3.6: Phantom and Coil for Single Voxel Acquisition Experiment. Voxel selection size was 10x10x40mm^3, The phantoms have a volume of 5ml each filled with 1: 6%, 2: 4% , 3: 2% and 4: 0% agar and 154mM Na.

4 Results I: Preclinical Results at 9.4 T

4.1 Liposome and Nanoparticle Results

The resulting spectra of the four different liposomes are shown in Fig. (4.1). The L1 and L2 liposomes, showed a triple-quantum amplitude of [0.37 %, 0.16 %, 0.34 %] with the noise level at 0.01 %, the confidence level exceeding 20 σ. In contrast, for L4 liposomes, with H_2O filling, the triple-quantum amplitude was [0.02 %] at the same noise level resulting in a signal of only 2 σ above the noise level. The triple-quantum amplitude of the nanoparticles resulted in [0.08 %], which deviated from the noise by $< 4\,\sigma$.

Fitting results gave a triple-quantum ratio of 0.8 for L1 and L3, 0.5 for L2 and 0.1 for the water filled liposomes L4 (Fig. 4.1). The liposome T2 slow and fast component was 24.1 ms ($\pm$ 3.2 ms) and 12.6 ms ($\pm$ 1.8 ms) with the maximum triple quantum signal at 17.0 ms ($\pm$ 2.3 ms). For the nanoparticles the fitted T2 values were 41.1 ms and 24.5 ms with maximum triple quantum signal at 29.4 ms.

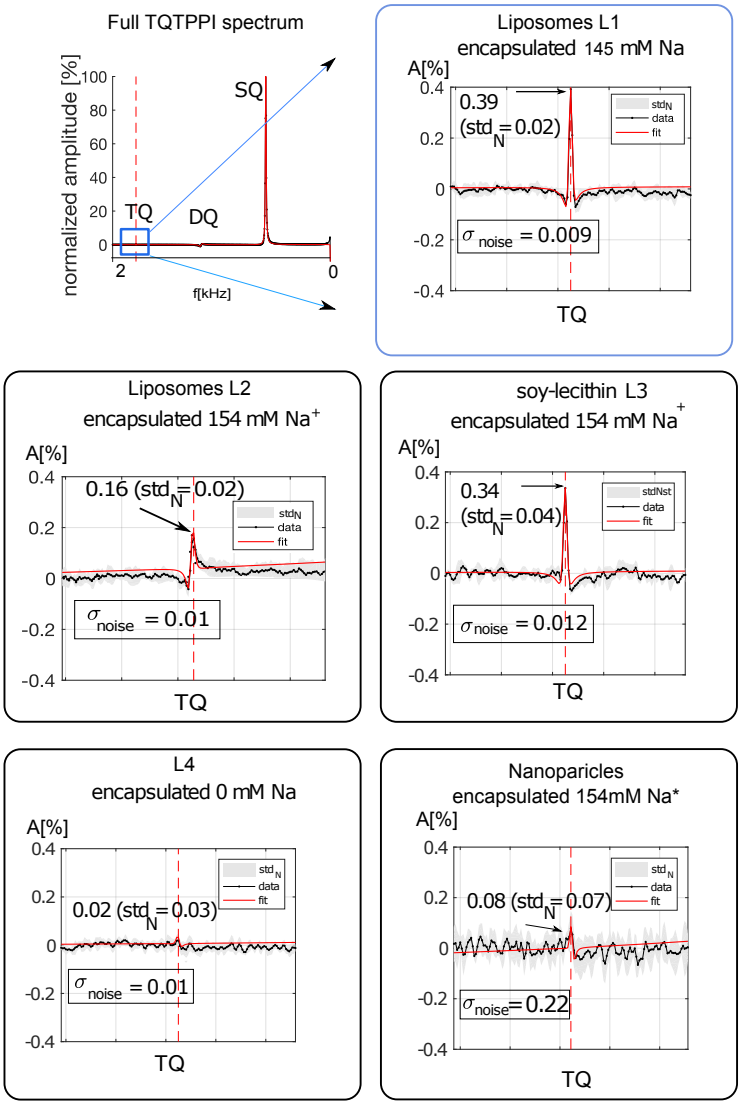

Figure. 4.1: TQTPPI spectrum result of liposomes and nanoparticles. The triple-quantum (TQ) signal is visible in the zoomed part of each spectrum, placed on the right as indicated in (I). In all spectra the TQ-signal amplitude is given along with the std_N over N measurements and the standard deviation σ_{noise} of the noise area to determine how well the TQ signal can be separated from noise. The fit is shown as solid line in red. Liposomes (L1,L2,L3) show a triple quantum signal that can be well distinguished from the noise level. L4 liposomes did not show a TQ signal within the resolution of our experimental data. In (V) Nanoparticles filled with sodium ion solution showed a low TQ signal.

4.2 MR-compatible Bioreactor Results

4.2.1 Human Liver Cells Results

The TQTPPI spectra consistently showed single- and triple-quantum (TQ) signals, as well as sub-optimally suppressed double-quantum signals (Figure 4.2). The triple-quantum transition region of the spectrum is shown enlarged to enhance visibility and the resulting nonlinear fit is shown (Figure 4.2). The cell chip measured on three successive days in bioreactor system, under optimal conditions for cell survival (C1, C2, C3), showed a TQ amplitude signal of [0.26 %, 0.17 %, 0.24 %]. The standard deviation in the noise region was [0.017 %, 0.018 %,0.015 %] resulting in a confidence level exceeding 9 standard deviations (Table 4.1). In the perfusion stop experiment the triple-quantum signal amplitude amounted to 0.15 %. The standard deviation of the noise region was 0.006 %, which was lower due to the higher averaging (N = 59), and resulted in a TQ signal of 24 σ. Setting the triple-quantum signal of the first day of 0.26 % to 100 % the signal level on the second day was 65 %, the signal in perfusion stop was 56 %. The signal on the third day where cells were again standardly perfused with oxygenated cell medium was 92 %. The TQ signal amplitude results are supported by the nonlinear fit results (Table 4.2). The ratio A_{TQ}/A_{SQ} amounted to [0.9 %, 1.0 %] for the cells C1 and C3. For C2 and in perfusion stop C_{PS} the fit resulted in a ratio of 0.6 % for the cell chip in unfavorable conditions for survival(C4) the ratio amounted to 0.14. For C4 a TQ signal was not observed (-0.02 %). T2 slow and fast component for the HEP G2 cells were 35.0 ms ($\pm$ 1.3 ms) and 20.9 ms ($\pm$ 1.9 ms) and the maximum triple-quantum signal was found by the fit to be at 26.2 ms ($\pm$ 1.3 ms).

The reference measurement of the bioreactor with MEM cell culture medium and the collagenized microcavity array, excluding cells, gave a triple-quantum signal of 0.06 % which exceeded the noise level only by 1 σ and a A_{TQ}/A_{SQ} ratio of 0.3 % which was half the ratio of the cells in perfusion stop (C_{PS}) and a third of the value of the cells on day 1 (C1). The T2 long and short component as well as the timepoint of the maximum of the triple-quantum signal were within the range of the cell experiment results. Within the resolution of our experimental data a clear triple-quantum signal exceeding 1 σ was not measured for the second cell chip, C4, nor the reference measurement without cells, BR Ref.

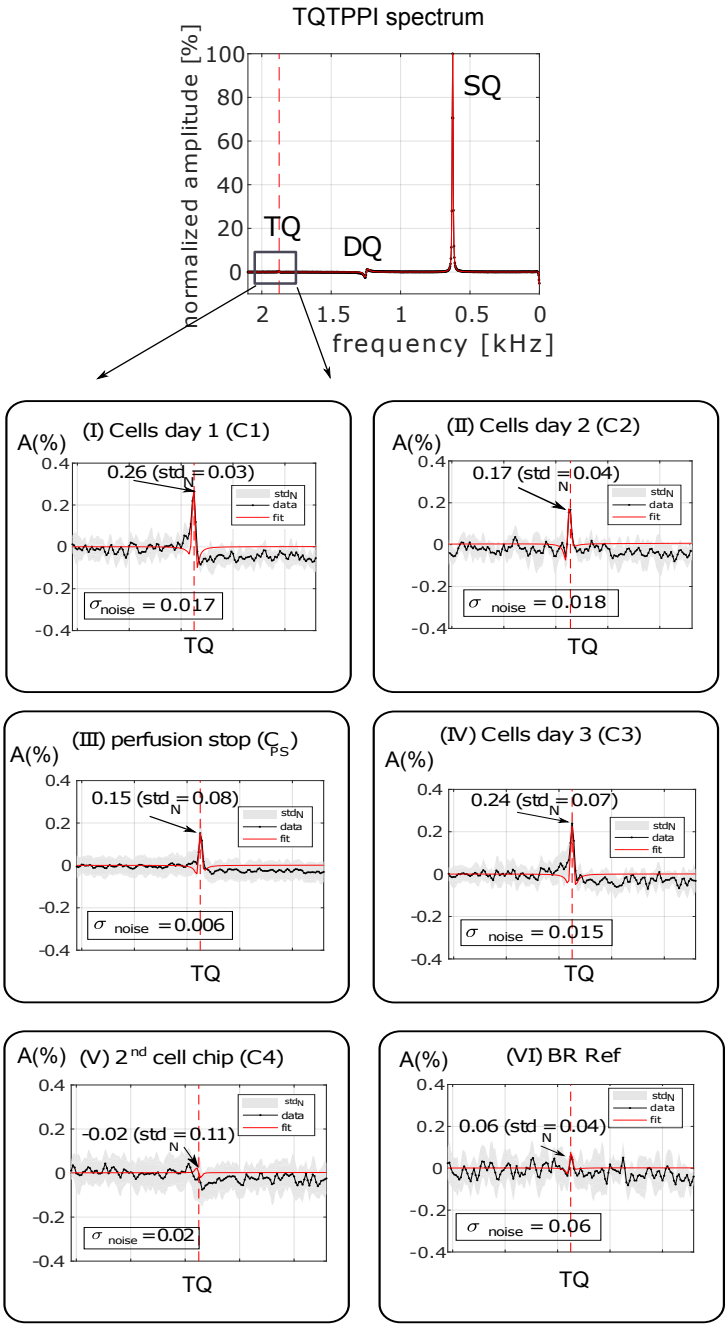

Figure. 4.2: TQTPPI spectrum, zoomed into the TQ position for the result of the first chip of HEP G2 liver cells (I)-(IV), the second chip (V) and the reference measurement (VI). TQ-signal amplitude is given along with the std_N over N measurements and the standard deviation σ_{noise} of the noise area to determine how well the TQ signal can be separated from noise. The fit is shown as solid line in red. TQ signal was obtained for (I)-(IV). In perfusion stop (III) the signal amplitude was lower but recovered after re-perfusion (IV). (V) sresulting spectrum from the second cell chip (C4). (VI) BR Ref: TQ signal for the collagenized chip, without cells.

Table. 4.1: TQ Signal Results in Spectrum Domain

Phantom	N	TQ_{peak} [%] $\pm$ std$_N$	σ[%]	$\frac{TQ_{peak}}{\sigma}\sigma$
C1	8	0.26 $\pm$ 0.03	0.017	15 σ
C2	8	0.17 $\pm$ 0.04	0.018	9 σ
C$_{PS}$	59	0.15 $\pm$ 0.08	0.006	25 σ
C3	8	0.24 $\pm$ 0.07	0.015	16 σ
C4	20	-0.02 $\pm$ 0.11	0.016	1 σ
BR ref	6	0.06 $\pm$ 0.04	0.060	1 σ
L1	6	0.37 $\pm$ 0.02	0.009	41 σ
L2	5	0.16 $\pm$ 0.02	0.007	23 σ
L3	3	0.34 $\pm$ 0.01	0.010	34 σ
L4	5	0.02 $\pm$ 0.03	0.010	2 σ
Nano	5	0.08 $\pm$ 0.07	0.022	4 σ

Phantoms are given by: the cells, C1-C3, the dead cells, C4, the bioreactor reference without cells, BR ref, the liposomes, L1-L4, and the nanoparticles, Nano. TQ_{peak} gives the average peak value of the triple-quantum (TQ) signal amplitude with respective standard deviation, std$_N$, for the number of experiments N. The standard deviation of the averaged signal in the noise region around the TQ peak gives σ denoted σ_{noise} in the corresponding figures. The TQ signal and the standard deviation are given in $\%$ of the SQ signal. The TQ signal can then be expressed in terms of σ to state the signal strength against the background.

Table. 4.2: TQTPPI Fit Results

Phantom	$\frac{A_{SQS}}{A_{SQ}}$ $\pm$ 4.0 [%]	$\frac{A_{TQ}}{A_{SQ}}$ $\pm$ 0.01 [%]	$T_{2,slow}$ $\pm$ 1.5 [ms]	$T_{2,fast}$ $\pm$ 1.5 [ms]	t_{max}^{TQ} $\pm$ 1.0 [ms]
C1	19.6	0.9	35.8	18.7	26.2
C2	24.8	0.6	35.3	19.1	24.4
C$_{PS}$	19.4	0.6	35.8	22.4	26.5
C3	20.8	1.0	35.2	23.0	28.1
C4	19.4	0.14	32.6	21.5	25.9
BR ref	20.0	0.3	34.7	22.2	26.8
L1	24.8	0.8	25.8	11.7	16.9
L2	25.3	0.5	23.3	13.5	18.0
L3	24.5	0.8	20.0	10.5	13.9
L4	19.8	0.1	27.3	14.6	19.2
Nano	22.7	0.3	41.1	24.5	29.4

Phantoms are given by: the cells, C1-C3, the dead cells, C4, the bioreactor reference without cells, BR ref, the liposomes, L1-L4, and the nanoparticles, Nano. The values of the time domain fit are shown including the long and short component of the single quantum amplitude (A_{SQ} = A_{SQL} + A_{SQS}) and the T$_2$ relaxation $T_{2,fast}$, $T_{2,slow}$. The TQ amplitudes are normalized by the single quantum amplitudes.t_{max}^{TQ} gives the evolution time at which the TQ signal is maximal.

4.2.2 Neonatal Cardiomyocytes Results

Neonatal cardiomyocytes were successfully cultivated on the microcavity arrays and spontaneous, synchronized beating was observed via light microscopy. The beating mechanism confirmed before and after the experiments in the MR compatible bioreactor, that cells were vital. For the stimulation of the beating, Isoprenaline was added to the cell culture medium. Isoprenaline stimulation was first performed on an additional cell chip outside of the MR compatible bioreactor and showed increased beating frequency under light microscopy. The measurement of the TQ signal was carried out in the following steps: (a) standard perfusion, (b) standard perfusion and Isoprenaline stimulation, (c) perfusion stop, (d) re-perfusion (Figure 4.3). Cardiomyocytes in the bioreactor with standard cell culture and under standard perfusion of 0.4ml/min, showed a significant mean TQ signal-amplitude of 0.15%($>$10 σ). During the following Isoprenaline stimulation, the mean TQ signal was 0.17% ($>$10 σ). In the subsequent perfusion stop, the mean TQ signal decreased to 0.06%(7σ) which was still significant. Subsequent re-perfusion showed a mean TQ signal return to the signal before perfusion stop with 0.15% (9σ). The fit in evolution time domain resulted in a T2fast of 22ms($\pm$1ms) and a T2slow of 32.5ms($\pm$2ms) with the maximum triple quantum signal at 26.7ms($\pm$1ms). Further, the fitted triple quantum signal amplitude, A_{TQ}, confirmed the decrease in TQ signal during perfusion stop (Figure4.3,Table and Table). Reference measurement results without cells showed a mean TQ signal of 0.04%(2σ) with A_{TQ} about one-fourth compared to cells under standard perfusion conditions.

Table. 4.3: Cardiomyocytes TQTPPI Results Spectrum Domain

cardiomyocytes @31°C	N	TQ_{peak} [%] $\pm$ std$_N$	σ_{noise}	$\frac{TQ_{peak}}{\sigma_{noise}}$
normal perfusion	32	0.15 $\pm$ 0.07	0.01	14 σ
isoprenaline additive	26	0.17 $\pm$ 0.05	0.01	17 σ
perfusion stop	31	0.06 $\pm$ 0.05	0.009	7 σ
reperfusion	6	0.15 $\pm$ 0.05	0.017	9 σ
reference without cells	34	0.04 $\pm$ 0.1	0.018	2 σ

TQ_{peak}: averaged amplitude value of the TQ signal with standard deviation, std$_N$, of the individual measurements N. The standard deviation of the averaged signal in the noise region σ_{noise}, gives the confidence level c.

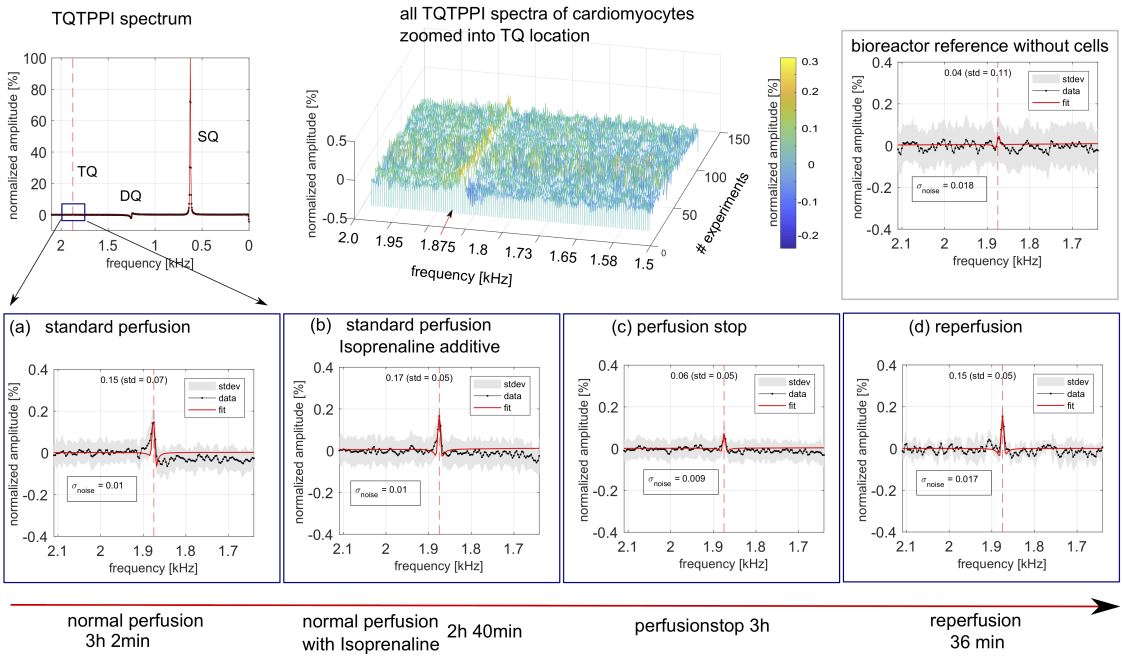

Figure. 4.3: Cardiomyocytes TQTPPI Result

Table. 4.4: Cardiomyocytes TQTPPI Fit Results

cardiomyocytes @31°C	A_{SQL}	A_{SQS}	$\frac{A_{TQ}}{A_{SQ}}$ [%]	$T_{2,slow}$ [ms] ± 2 ms	$T_{2,fast}$ [ms] ± 1 ms	t_{max}^{TQ} [ms]
normal perfusion	0.77	0.25	0.80	34.0	23.2	27.9
isoprenaline additive	0.80	0.20	0.82	31.3	22.2	25.8
perfusion stop	0.77	0.25	0.35	32.0	22.4	26.6
reperfusion	0.81	0.20	0.76	32.7	22.4	26.6
reference without cells	0.87	0.25	0.23	31.3	22.0	26.1

A_{SQ} = A_{SQL} + A_{SQS} and the fast and slow component of the T2 relaxation $T_{2,fast}$, $T_{2,slow}$, the triple quantum amplitude normalized by the single quantum amplitude gives a measure of TQ signal strength. Further the maximum time point of the TQ signal is given.

4.3 Single Voxel Localized TQTPPI results

Localization measurements preserved the quantum coherences for both sequences. Agar-phantom result and in-vivo rat result is given in Figure4.4, 4.5 respectively. Compared to the global TQTPPI sequence with the LOC-S and LOC a drop of 1% and 3.3% of TQS was measured respectively when choosing a global voxel size of 100x100x100mm^3 . Resulting normalized TQS values can be found in Figure3. TQS decreased with smaller voxel sizes, a voxel size of 10x10x40mm^3 is 16% in volume of the voxel size 25x25x40mm^3 and TQS dropped by 22% for LOC-S and by 26% for LOC(Figure 4.4, 4.5). Figure 4.6 illustrates results of the agar-phantom-stack with a voxel size of 10x10x40 mm3. The resulting spectra for the 6%, 4% and 2% agar tubes show a decreasing TQS for both sequences (Figure 4.6). Therefore, it was possible to distinguish the tubes based on their relative result in TQS with both sequences.

(a) 4% agar phantom

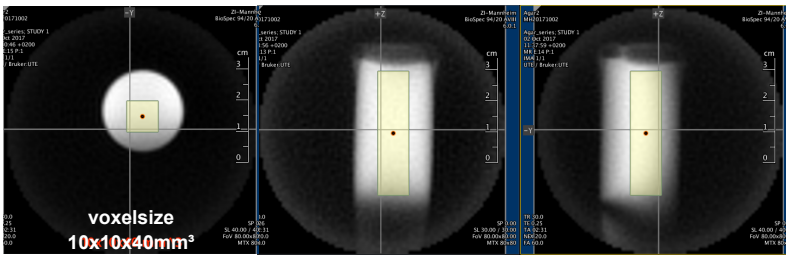

(b) healthy in-vivo rat head

Figure. 4.4: Single Voxel Localization Placement in Phantom and In Vivo Rat: (a) 4% agar phantom in transversal, coronal and sagittal view with voxelsize 10x10x40mm^3. In vivo rat the voxel size was 25x25x40mm^3 choosing the brain region.

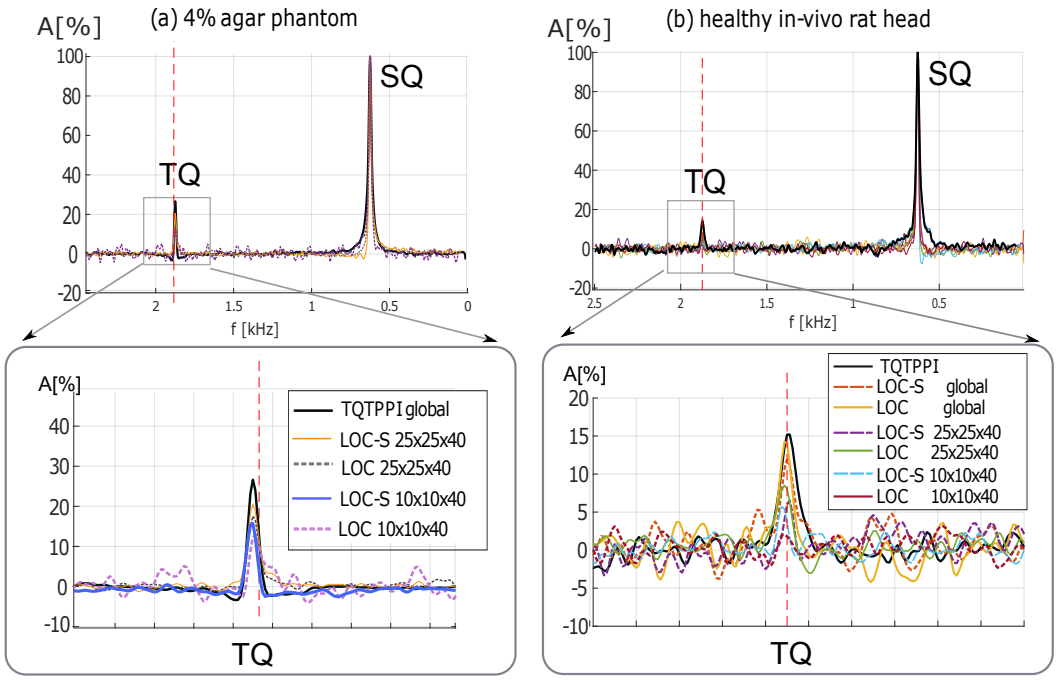

Figure. 4.5: The figure shows the sodium TQTPPI spectrum result of

Table. 4.5: Single Voxel TQTPPI - TQ signal Result

sequence	voxel size	4% Phantom TQ Signal	In vivo Rat TQ signal
TQTPPI	global	26.6%	15.2 %
LOC-S	global	-	14.2 %
LOC	global	-	11.9 %
LOC -S	25x25x40 mm^3	20.4 %	8.5 %
LOC	25x25x40 mm^3	17.6%	6.3%
LOC-S	10x10x40 mm^3	16.0%	5.7%
LOC	10x10x40 mm^3	13.0%	2.1%

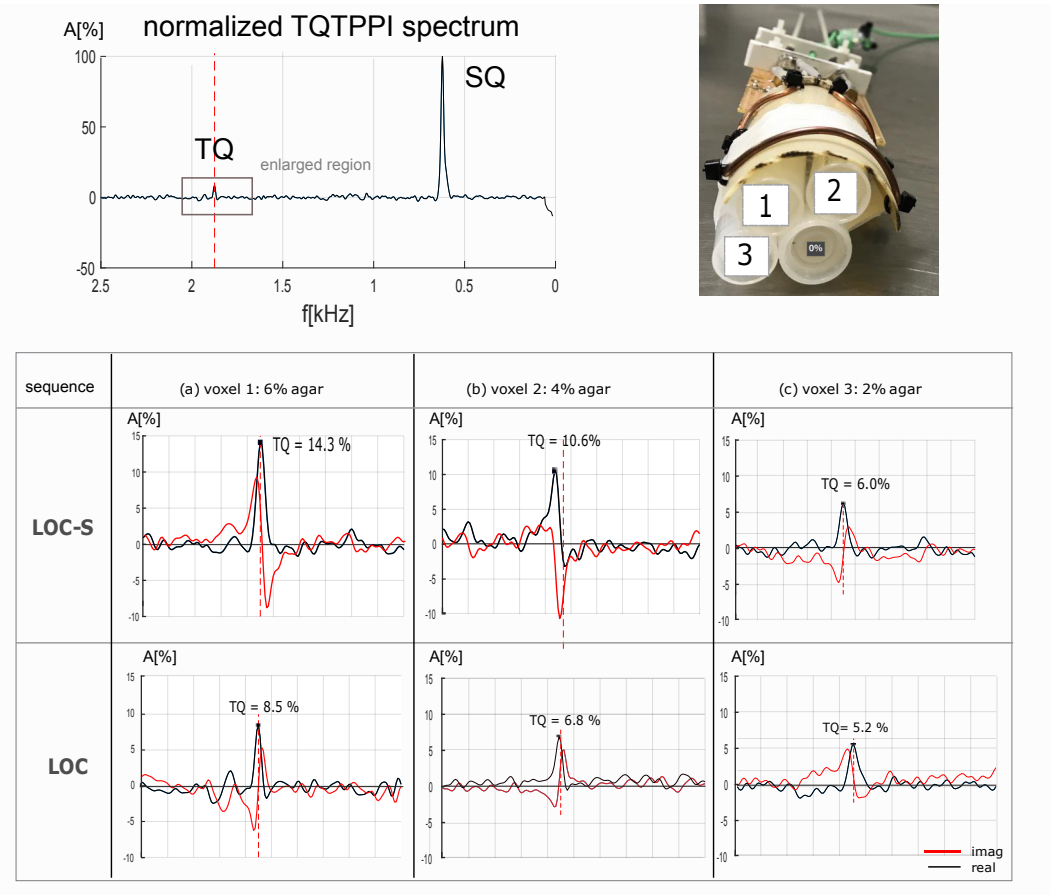

Figure. 4.6: Comparison of Single Voxel TQTPPI sequences: LOC-S and LOC for three different agar phantoms. TQ signal was highest for the 6% agar phantom, followed by the 4% and then the 2% phantom as expected by agar content. This showed that voxel localization in a phantom of combined vials did work correctly. The fourth phantom vial had 0% of agar and TQ was in the order of noise and is not shown here. The sequence, LOC-S, using the slice selecting gradient resulted in a higher TQ signal compared to the three 180° pulses at the end.

4.4 Preclinical Insights

The preclinical investigations on the different cells types and in various conditions resulted in a deeper understanding of the TQ signal behavior in cells and showed that the signal is connected to the cell vitality. This direct measurement and getting this information was only possible by the MR compatible bioreactor setup and cell culture measurement. Healthy cells in the bioreactor showed a TQ signal. A lack of oxygen was connected to a decreased TQ signal, which is explainable by the necessity of oxygen in the energy production of cells. Dead cells did not show a TQ signal. These results are important before a transfer of methods to the clinic to interpret tissue signals in vivo. However, it has to be taken into account, that in the preclinical bioreactor setting, the cells did not have their common extracellular surroundings. Further, first signal localization methods showed its feasibility and were encouraging for a clinical localized TQ sequence development. However, it has to be noted that in a clinical setting the use of 180° pulses for localization is unfavorable due to high specific absorption rate (SAR) problem because 180° pulses are achieved by high peak voltages (or longer pulses, which are not favored due to relaxation) and can lead to heating of the body.

5 Methods II: Simulation of the coherence transfer signal

To measure and filter for different coherence pathways in general a three-pulse sequence is needed along with phase cycle to select the coherence of interest [3]. The conventional three pulses sequence is depicted in Figure (5.1a) along with the coherence pathway scheme (Figure 5.1b). The experiment features three time parameters which impact the eventual measured signal. Among these three, τ_2, the time between the second and third pulse, is usually minimized to avoid relaxation of the created MQC signals. In the following simulation relaxation between those two pulses is therefore neglected. However, evolution time, τ_1, as well as echo time, TE, are in strong relation with the bi-exponential relaxation which separates SQ from DQ and TQ coherences. The first pulse's phase, Φ_1, cycles through a defined cycle while the second pulse's phase is shifted by "phase-shift, ξ" relative to the first. The third pulse's phase as well as the receiver phase are set to 0°. The method of sequence repetition while cycling the phases of the RF pulses ultimately results in constructive and destructive interference of the MQC pathways depending on the selected phase cycling scheme by utilizing the different evolution frequencies of the MQCs.

Different phase cycling options have been proposed to eliminate potential biases. The original 6 step phase cycle by [4] builds the basis. This is followed by the triple-quantum (time) proportional phase increments (TQTPPI) sequence to measure the TQC signal without any prior relaxation knowledge [82, 29]. Biases due to B0 inhomogeneity, relaxation processes and stimulated echo signals are presented with the proposed phase cycling options by [93] and [94]. The following four cases are highlighted, which sample the 2π interval in different steps. The second pulse phase will be given in relation to the first by $\xi = \Phi_1 - \Phi_2$. The start phase, the first point in the phase cycle, is denoted by $\Phi_{1,t=0}$:

1. Option 1: the original 6 step phase cycle
2. Option 2: the 2x8 step phase cycle of the TQ(TP)PI sequence
3. Option 3: the 2x6 step Fleysher phase cycle for B0 inhomogeneity signal recovery

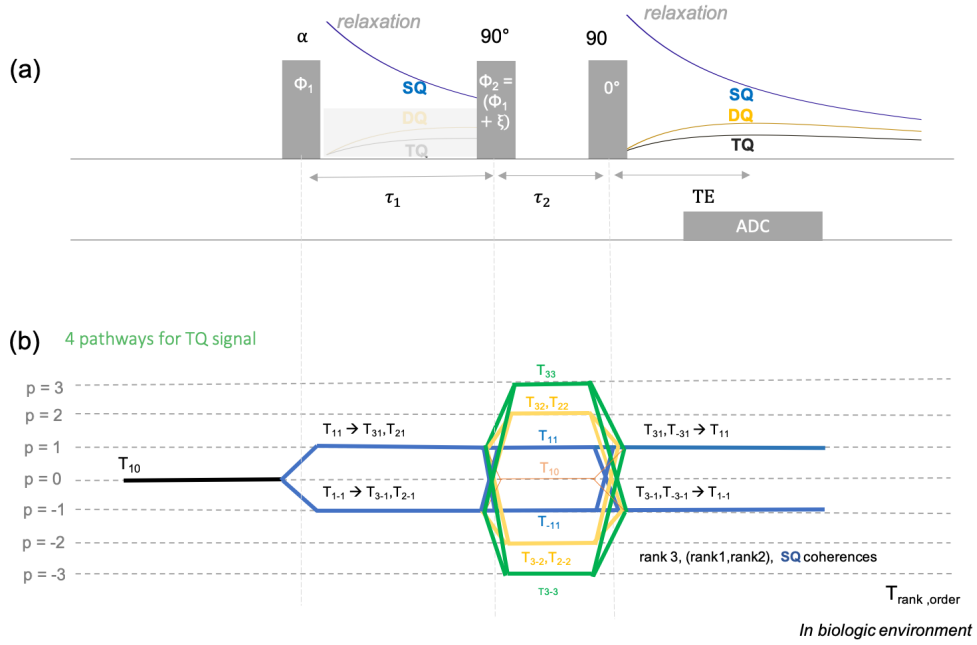

Figure. 5.1: Three-pulses sequence and Coherence Transfer Pathway Diagram: (a) Three pulses experiment. The time between the first excitation pulse and the second pulse is called evolution time (τ_1). The time between the second and third pulse is the mixing time (τ_2). (b) Coherence transfer pathway diagram. After RF pulse the tensor $T_{rank,order}$ can change the order whereas relaxation and quadrupolar coupling can change the rank of the tensor. In perfect quadrature detection only coherence level of -1 is observable however in MRI not imperfect quadrature detection is common and signals can end up in this pathway.

4. Option 4: the 4x6 step SISTINA phase cycle with an option to suppress signal bias due to stimulated echo signal

First, the originally 6-step phase cycle was introduced and samples the 2π interval with a phase increment of $^{2\pi}/_{6}$. The second pulse is phase shifted by $^{\pi}/_{2}$ to the first pulse and the third pulse as well as the receiver phase are 0°.

Second, the priorly introduced TQTPPI NMR method, which stands for TQ time proportional phase increments [82, 29]. It features capturing of the relaxation constants, $T2^*_{slow}$ and $T2^*_{fast}$ without the need to set the optimal evolution and echo time, as they are sampled by starting from a minimum time and increased along with stepping through the phase cycle. Its advantage is a signal acquisition free of assumptions on relaxation parameters without setting an optimal evolution time which might not be perfect. The TQ(T)PPI method with and without incrementing the evolution time was reported by [4, 29] with a phase increment $\Delta\Phi_1$ of $^{2\pi}/_{8}$. An

additional phase cycle was proposed to eliminate DQC [29].

Option 2:

- $\Delta\Phi_1 = {}^{2\pi}/_{8}$
- 1^{st} cycle: $\Phi_{1,t=0} = {}^{\pi}/_{2}$, $\xi = +{}^{\pi}/_{2}$
- 2^{nd} cycle: $\Phi_{1,t=0} = {}^{\pi}/_{2}$, $\xi = -{}^{\pi}/_{2}$

Third, [93] presented an additional phase cycle to recover the signal that is cancelled due to B0 inhomogeneity. In MRI, B0 inhomogeneity can be severe and lead to spins de-phasing which results in MQC signal loss. The proposed solution consists of a second, independent, phase cycle, in addition to the original phase cycle. Using gradient spoiling would be an alternative to eliminate the impact of B0 inhomogeneity with the disadvantage of lowering the SNR due to the spoiling of half the coherence pathway contributions. Fleysher's additional 6 step phase cycle features equal pulse phase of first and second pulse with the following parameters:

Option 3:

- $\Delta\Phi_1 = {}^{2\pi}/_{6}$
- 1^{st} cycle: $\Phi_{1,t=0} = {}^{\pi}/_{2}$, $\xi = {}^{\pi}/_{2}$
- 2^{nd} cycle: $\Phi_{1,t=0} = 0$, $\xi = 0$

Fourth, signal bias due to stimulated echo signal was discussed and a solution was proposed by [95, 94], employed in the SISTINA sequence. In general, a three-pulse sequence can form a stimulated echo signal which was described in detail in the literature [96, 97, 98]. The magnetization is sent to the transverse plane with the first RF pulse and returned to the z-axis by application of the second RF pulse, without phase memory. The third pulse tips the magnetization again to the transverse plane, where the spins de-phase and refocus to form the stimulated echo. For the presented three pulses sequence to obtain multi-quantum coherences signal, a stimulated echo signal could possibly give an unwanted bias. An additional phase cycle was introduced:

Option 4:

- $\Delta\Phi_1 = {}^{2\pi}/_{6}$
- 1^{st} cycle: $\Phi_{1,t=0} = {}^{\pi}/_{12}$, $\xi = {}^{\pi}/_{2}$
- 2^{nd} cycle: $\Phi_{1,t=0} = {}^{7\pi}/_{6}$, $\xi = {}^{-\pi}/_{2}$
- 3^{rd} cycle: $\Phi_{1,t=0} = {}^{2\pi}/_{3}$, $\xi = {}^{\pi}/_{2}$
- 4^{th} cycle: $\Phi_{1,t=0} = {}^{5\pi}/_{3}$, $\xi = {}^{-\pi}/_{2}$

The SISTINA sequence (Figure 5.2) chose the above specified phase cycles for the in vivo measurements with the priority to eliminate stimulated echo signal. For phantom measurements B0 inhomogeneity was eliminated by additional phase cycling according to Option 3. In the following, the impact of stimulated echoes versus B0 offset was investigated to make a founded choice for optimal measurement parameters for in-vivo.

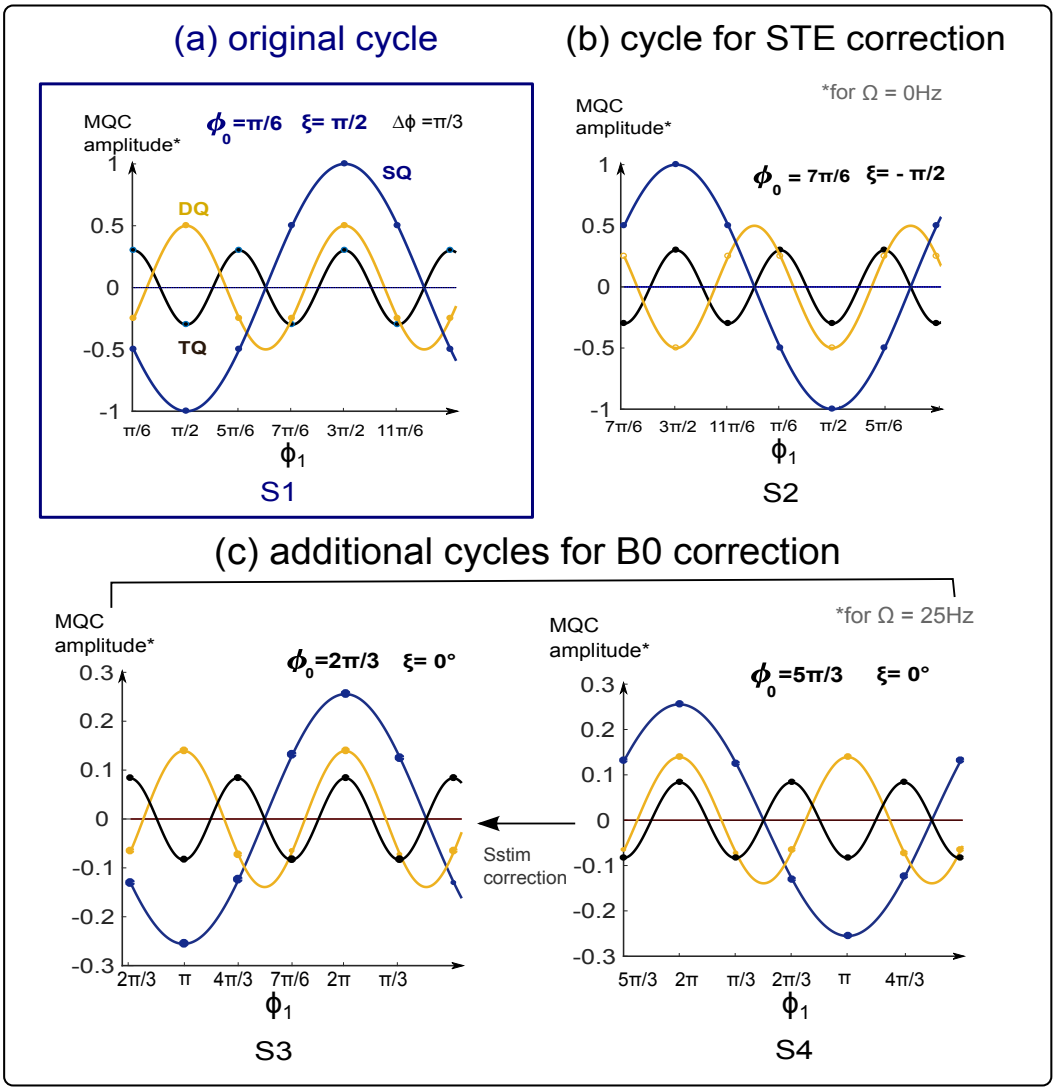

Figure. 5.2: (a) shows the three pulses experiment. The time between the first excitation pulse and the second pulse is called evolution time (τ_1). The time between the second and third pulse is the mixing time (τ_2). (b) shows the coherence transfer pathway diagram. After RF pulse the tensor $T_{rank,order}$ can change the order whereas relaxation and quadrupolar coupling can change the rank of the tensor. In perfect quadrature detection only coherence level of -1 is observable however in MRI not imperfect quadrature detection is common and signals can end up in this pathway.

Table. 5.1: Phase-cycle Options Summary

Option	$\Delta\Phi_1$	N cycles	1^{st} cycle $\Phi_{1,t=0}$, ξ	2^{nd} cycle $\Phi_{1,t=0}$, ξ	Alias
1	$2\pi/6$	1	$\pi/2$, $+\pi/2$	-	Original
2	$2\pi/8$	2	$\pi/2$, $+\pi/2$	$\pi/2$, $-\pi/2$	TQTPPI
3	$2\pi/6$	2	$\pi/2$, $\pi/2$	0, 0	Fleysher
4	$2\pi/6$	4	$\pi/12$, $\pi/2$ 3^{rd}: $2\pi/3$, $\pi/2$	$7\pi/6$, $-\pi/2$ 4^{th} : $5\pi/3$, $-\pi/2$	SISTINA
5	$\pi/6$	2	$\pi/2$, $\pi/2$	0, 0	CRISTINA

5.1 Simulation of coherence transfer pathway signals

5.1.1 Excluding Relaxation Terms

For the development of the simulation formalism, the signal equations by Fleysher et al. [93] was followed. The coherence levels after the first and second excitation are denoted by p1 and p2 respectively. Matrix $A_{p1,p2}$ contains the amplitudes of the respective coherence pathway:

$$A\,(p1,p2) = \begin{array}{c|cccccc} \frac{p2\rightarrow}{p1} & -3 & -2 & -1 & +1 & +2 & +3 \\ -1 & -TQ/4 & -DQ/4 & -SQ/4 & -SQ/4 & -DQ/4 & -TQ/4 \\ +1 & TQ/4 & DQ/4 & SQ/4 & SQ/4 & DQ/4 & TQ/4 \end{array}$$

For the simulation, a specific amplitude was set for the signals of the MQCs: SQ, DQ, TQ. By coherence level transfer this initially set amplitude is divided into its possible pathways. For instance, there are four possibilities for the TQ coherence (compare to Figure 5.1b). Let us start with one of these four pathways, from the coherence level p1 = -1 directly after the first pulse. With the second pulse, the coherence level is transferred to p2=-3. The resulting signal is in the $T_{3\text{-}3}$. For measurement of the signal, it is crucial to transfer the signal again to “transverse plane" signal. This is achieved by the third pulse, which transfers $T_{3\text{-}3}$ into rank three SQ coherences $T_{3\text{-}1}$ which evolves into $T_{1\text{-}1}$. It will be shown that the relaxation processes after the third pulse are crucial for the received MQC signal. The received signal, S, takes into account all coherence pathways and was written as:

$$S(\tau_1,\tau_2,\Phi_1,\Phi_2,\Omega,TE) = \sum_{p1}\sum_{p2} e^{-i(p_1\phi_1+(p_2-p_1)\phi_2)} \cdot B_{Na}\,(p_1,p_2,\tau_1,\tau_2,\Omega,TE,A_{p1,p2}) \quad (5.1)$$

$$B_{Na} = e^{-i(p_1\tau_1+p_2\tau_2)\Omega} e^{i\Omega TE}\, A_{p1,p2}$$

Parameter Ω(Hz) describes the off-resonance effects which were used here for simulating magnetic field inhomogeneity. Zero values of the above signal, S, are given analytically for values of:

$$\Omega(Hz) = \frac{k\pi + \xi}{2\pi\tau_1} \quad (5.2)$$

5.1.2 Calculation of Analytical Zero Points

Starting from Equation 5.1:

$$S\left(\tau_1, \tau_2, \phi_1,\ \phi_2, \Omega, TE\right) / e^{i\Omega TE} = \sum_{p1} \sum_{p2} e^{-i((p_1\phi_1 + (p_2 - p_1)\phi_2) + (p_1\tau_1 + p_2\tau_2\ )\Omega)}\ A_{p1,p2}$$

The phase values are factorized in the following:

$$((p_1\left(\phi_1 - \phi_2\right) + p_2\phi_2) + (p_1\tau_1 + p_2\tau_2\ )\,\Omega) = (p_1\left(\Omega\tau_1 - \xi\right) + p_2\left(\phi_2 + \Omega\tau_2\right))$$

Considering the table of the multiple quantum magnitudes $A_{p1,p2}$ 5.1.1, the three different quantum coherences can be considered equivalently and the triple quantum computation was chosen. However, replacing $p_2 = \pm 3$ with $p_2 = \pm 2$ or $p_2 = \pm 1$ will lead to identical results.

$$\begin{aligned} S_{TQ} / \left(TQ / 4e^{i\Omega TE}\ \right) = & -e^{-i(-1(\Omega\tau_1 - \xi) - 3(\phi_2 + \Omega\tau_2))} \\ & + e^{-i(1(\Omega\tau_1 - \xi) - 3(\phi_2 + \Omega\tau_2))} \\ & - e^{-i(-1(\Omega\tau_1 - \xi) + 3(\phi_2 + \Omega\tau_2))} \\ & + e^{-i(1(\Omega\tau_1 - \xi) + 3(\phi_2 + \Omega\tau_2))} \end{aligned}$$

The following substitution eases reading: $L = e^{i(\Omega\tau_1 - \xi)}$ and $M = e^{i3(\phi_2 + \Omega\tau_2)}$

$$\begin{aligned} \frac{4\ S_{TQ}\left(\tau_1, \tau_2, \phi_1,\ \phi_2, \Omega, TE\right)}{TQe^{i\Omega TE}} &= -LM + L^*M - LM^* + L^*M^* \\ & - L\left(M + M^*\right) + L^*\left(M + M^*\right) \\ & = \left(M + M^*\right)\left(L^* - L\right) \end{aligned}$$

Thus, signal nulling for all quanta occurs for:

$L^* - L = 0$, which corresponds to $L = e^{ik\pi}\ = 1\ for\ k \in \mathbb{Z}$

This corresponds to: $\Omega\tau_1 - \xi = k\pi\ for\ k \in \mathbb{Z}$

and therefore: $\Omega_0 = \frac{k\pi+\xi}{\tau_1} \quad for\ k \in \mathbb{Z}$
or $\Omega_0 = \frac{k\pi+\xi}{2\pi\tau_1}$ for Ω in Hz

5.1.3 Simulation Including Relaxation Terms

The following equations were formulated to take into account relaxation effects. Transverse relaxation for the SQ signal was described by the bi-exponential decay divided into T2*slow and T2*fast components:

$$SQ = SQ_0 \left(\frac{3}{5} e^{-\frac{(TE+\tau_1)}{T2*_{slow}}} + \frac{2}{5} e^{-\frac{(TE+\tau_1)}{T2*_{fast}}} \right) sin\left(\theta_{exc}\right) \tag{5.3}$$

For the DQ and TQ coherence signal the relaxation terms are given by:

$$MQ = MQ_0 \left(e^{-\frac{TE}{T2^*_{slow}}} - e^{-\frac{TE}{T2^*_{fast}}} \right) \left(e^{-\frac{\tau_1}{T2^*_{slow}}} - e^{-\frac{\tau_1}{T2^*_{fast}}} \right) e^{-\frac{\tau_2}{T2^*_{slow}}} sin^5\left(\theta_{exc}\right) \tag{5.4}$$

$$MQ = DQ, TQ$$

5.1.4 Stimulated Echo Signal Bias

The stimulated echo signal (STE) depends on the flip angle, relaxation effects, B0 inhomogeneity and was described as follows:

$$S_{STE} = \sum_{p1} \sum_{p2} e^{-i(p_1\phi_1+(0-p_1)\phi_2)} B_{STE}\left(\tau_1,\tau_2,\Omega,TE,\xi,T_1,T2^*_{slow},T2^*_{fast},A(m,n)\right) \tag{5.5}$$

$$B_{STE} = \frac{|A_{p1,p2}|}{2} e^{-\frac{\tau_2}{T_1}} cos\left(\xi - \Omega\tau_1\right) e^{i\Omega TE} \left(\frac{3}{5} e^{-\frac{(TE-\tau_1)^2}{2(T2^*_{slow})^2}} + \frac{2}{5} e^{-\frac{(TE-\tau_1)^2}{2(T2^*_{fast})^2}} \right) \tag{5.6}$$

The maximum of B_{STE} with respect to echo time is given analytically for TE = τ_1.

5.1.5 Signal reconstruction

MQC signals can be separated by their scaled evolution frequencies, as defined by their phase term:
$e^{-i(p_1\Phi_1+(p_2-p_1)\Phi_2)} = \mathbf{e^{-ip_2\Phi_1}}e^{i(p_2-p_1)\xi}$. The spectrum signal is thus reconstructed by Fourier Transformation (FT) along the phase dimension Φ_1. According to Fleysher, the signals, S, of the two phase-cycles, are transformed independently:

$$\hat{S}_{\xi=n} = FT\left(S_{\xi=n}\right) \;\; n = \frac{\pi}{2}, 0 \tag{5.7}$$

$\hat{S}$ denotes the Spectrum, normalized to the size of Signal to obtain correct FT values. In the next step, the two Spectra are combined:

$$\hat{S}_{\pm} = \frac{1}{2}\left(\hat{S}_{\xi=0} \pm i\hat{S}_{\xi=\frac{\pi}{2}}\right) \tag{5.8}$$

To recover the signal, knowledge of the B0 offset, Ω , that lead to a dephasing during the evolution time,τ_1 , and echo time,TE, is used to rephase the signal:

$$\hat{S}|_{t=TE,\;\; B0offset=\Omega} = \frac{1}{2}\left(\left(\hat{S}_+|_{TE,\,\Omega}\right)\right)e^{+i\Omega\tau 1} - \left(\hat{S}_-|_{TE,\,\Omega}e^{-i\Omega\tau_1}\right)e^{-i\Omega TE} \tag{5.9}$$

In SISTINA, a total of four phase cycles was proposed (4x6steps) to accomplish a full signal recovery, correcting both, STE and B0 offset biases (compare to Figure 5.2). The individual signals for the n = 4 phase cycles are Fourier transformed. As reported, the Spectra are then reconstructed from the Fourier transformed signal:

$$\hat{S}_n = FT\left(S_n\right)\; n = 1,2,3,4 \tag{5.10}$$

$$\hat{S}|_{invivo} = \sqrt{\hat{S}_1^2 + \hat{S}_2^2} \tag{5.11}$$

$$\hat{S}|_{total} = \sqrt{\hat{S}_1^2 + \hat{S}_3^2 + \hat{S}_2^2 + +\hat{S}_4^2} \tag{5.12}$$

5.1.6 Simulation parameter settings

The following parameter values, in accordance with realistic measurement values were used: τ_1=10 ms, τ_2= 100 s, $T2^*_{slow}$= 30 ms, $T2^*_{fast}$= 4 ms, T1 = 70 ms. The three flip-angles were set to $\pi/2$. The matrix $A_{(m,n)}$, was set to 1.0, 0.5 and 0.3 for the SQ, DQ and TQ coherences amplitudes respectively. Under the assumption of T1 in the order of 70ms and the usage of long TR values, $>$120 ms to comply with specific absorption rate (SAR) limitation the longitudinal relaxation was further neglected in the simulations.

Results II: Simulation Results

6

6.1 The original cycles

First, the simulation of the original 6-steps phase cycle with neither B0 inhomogeneity, Ω, nor relaxation effects is shown in Figure 6.1. The choices for the 6 samples appear relevant to measure the full amplitude of the TQ signal, whereas DQ is not optimally sampled. Also, the choice for 6 samples places the TQ signal at the Nyquist limit. Fourier Transformation along the evolution phase Φ_1 recovers the amplitudes of the mixed coherences signal of (SQ, DQ, TQ) = (1.0, 0.5, 0.3) (Figure 6.1b). The amplitudes in the spectrum do not have a Lorentzian shape because the phase cycle does not capture relaxation processes.

6.2 Phase increment and double quantum signal suppression

Second, regardless of the time-increments (hence the name TQ(T)PPI), the TQPPI samplings for the two phase-cycles with $\xi = \pm\pi/2$ can be seen in Figure 6.2, and Figure 6.3. It is demonstrated that phase increment choices (45° increment) oversample the TQ signal. The 45° phase increment samples the maximum of the TQ signal only in 2 out of 8 points, with 4 points falling short of measuring the maximum point. In contrast, the sampling points measure optimally the maximum amplitude of the DQ signal, which is opposite in signal for the two cycles and hence cancels out when the signals are combined. Without considering B0 offset, the SQ and TQ signal is equivalent for the two cycles with the signal ending up only in the imaginary channel. When relaxation processes and B0 offsets (100 Hz range) are included, an oscillatory pattern for all quantum coherences was observed with occurrences of complete signal loss matching the analytical result. Signal cancellation was be observed for the two phase-cycle signals S1, S2 and the reconstructed spectra $\hat{S}$ at the same frequency offset (25 Hz and 75 Hz). Further, it can be observed that the DQ signal suppression is also achieved when relaxation processes are considered, and a B0 offset alters the signal. Whereas the MQC

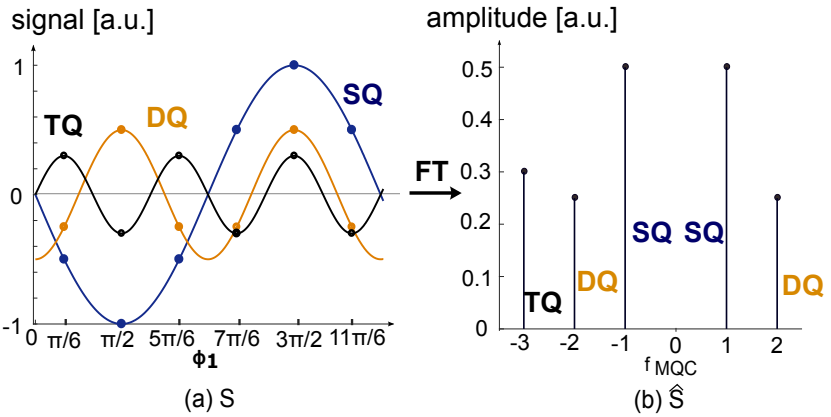

Figure. 6.1: Original Three-pulses Phasecycle with phase increment of $2\pi/6$ and start phase of $\pi/6$. The phase cycling points are indicated with the circles at the respective phase values. (a) Signal of the different coherence contributions for arbitrarily chosen amplitudes (b) corresponding Spectrum after FT

magnitude signal is equivalent for the two cycles, the phase images show opposite signs for the DQ signal.

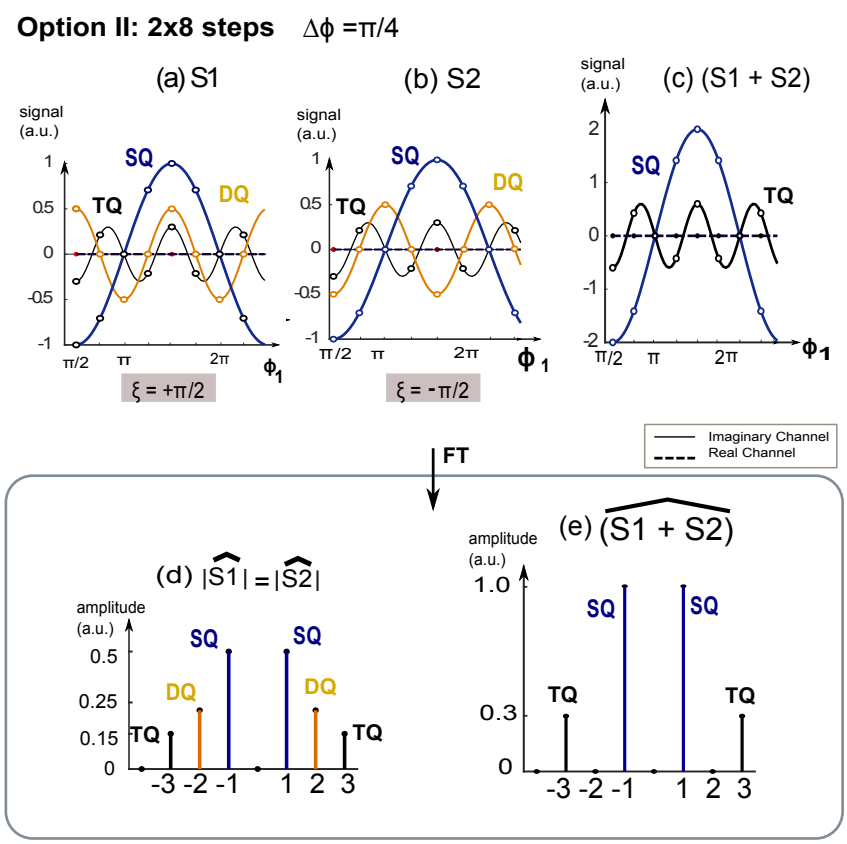

Figure. 6.2: Option 2 Phase Cycle without Relaxation Processes: TQ(T)PPI phase cycling signal over Φ_1 dimension for the two different phase cycles with $\xi = \pm\pi/2$. Optimal measurement points at the maximum occurs for SQ and DQ but TQ maximum is sampled at only 2 out of 8 points. Sampling steps are indicated in circles. Evolution time increment and relaxation have been discarded. The sum of the two cycles signals effectively cancels out DQ signal. In the resulting spectra the DQ cancellation can be observed, and oversampling leads to TQ being split in 2 components.

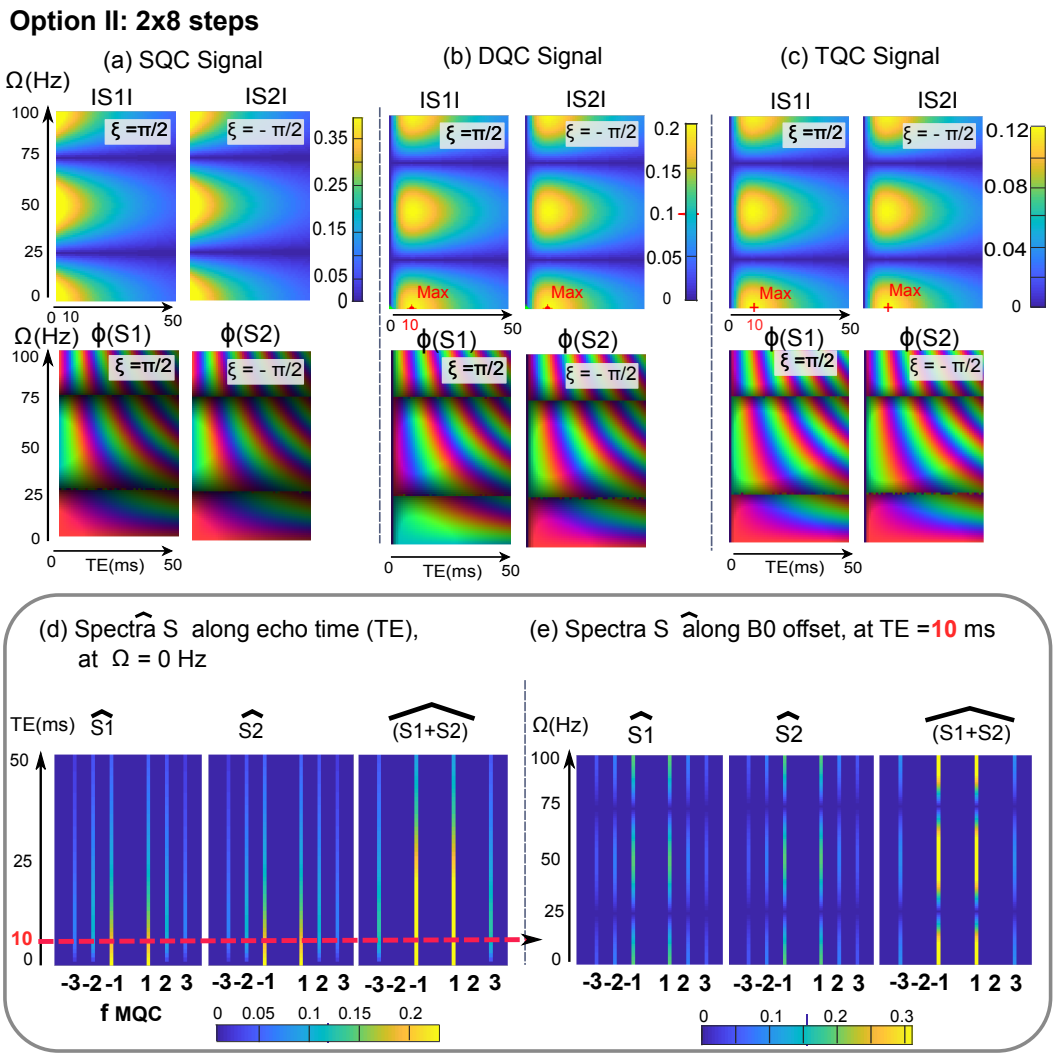

Figure. 6.3: Option2 Signal and Spectral results under B0 Offset Influence and Relaxation Effects: TQ(T)PPI simulation including relaxation and B0 offset. The magnitude and phase of the signals at Φ_0 are shown independently for the three quantum coherences, (a)SQ, (b)DQ and (c)TQ. The complex DQ signal (Row II.) shows signal cancellation due to opposite phases for the two phase-cycles. For the SQ and TQ signals, signal addition is constructive. (d) and (e) show the spectra for the individual phase cycles ($\xi = \pm\pi/2$) as well as for the added signals in (d) along the B0 offset and (e) along the echo time. Signal cancellation at 25Hz and 75Hz can be observed.

6.3 Magnetic field inhomogeneity bias

The third phase cycling option, called Fleysher's, recognized the possibility of extreme signal loss in the presence of B0 inhomogeneity. Fleysher's two cycles along with its reconstruction are presented in Figure 6.4 exemplary for an offset of 10 Hz. The full signal recovery (neglecting relaxation) can be appreciated in the amplitudes of the spectrum $\hat{S}_{reco}$. The full simulation, including relaxation and a range of 100 Hz offsets shows again an oscillatory pattern for the MQC signals along the B0 offset with occurrences of complete signal loss. The key point is that the two cycles are complementary in exhibiting signal cancellation and signal maximum (Figure 6.5). For our set of simulation parameters e.g. at an offset of Ω = 25 Hz the signal is recovered in the second phase cycle while being completely cancelled in the original phase cycle. The oscillation of the original signal thus has a counterpart in the additional phase cycle.

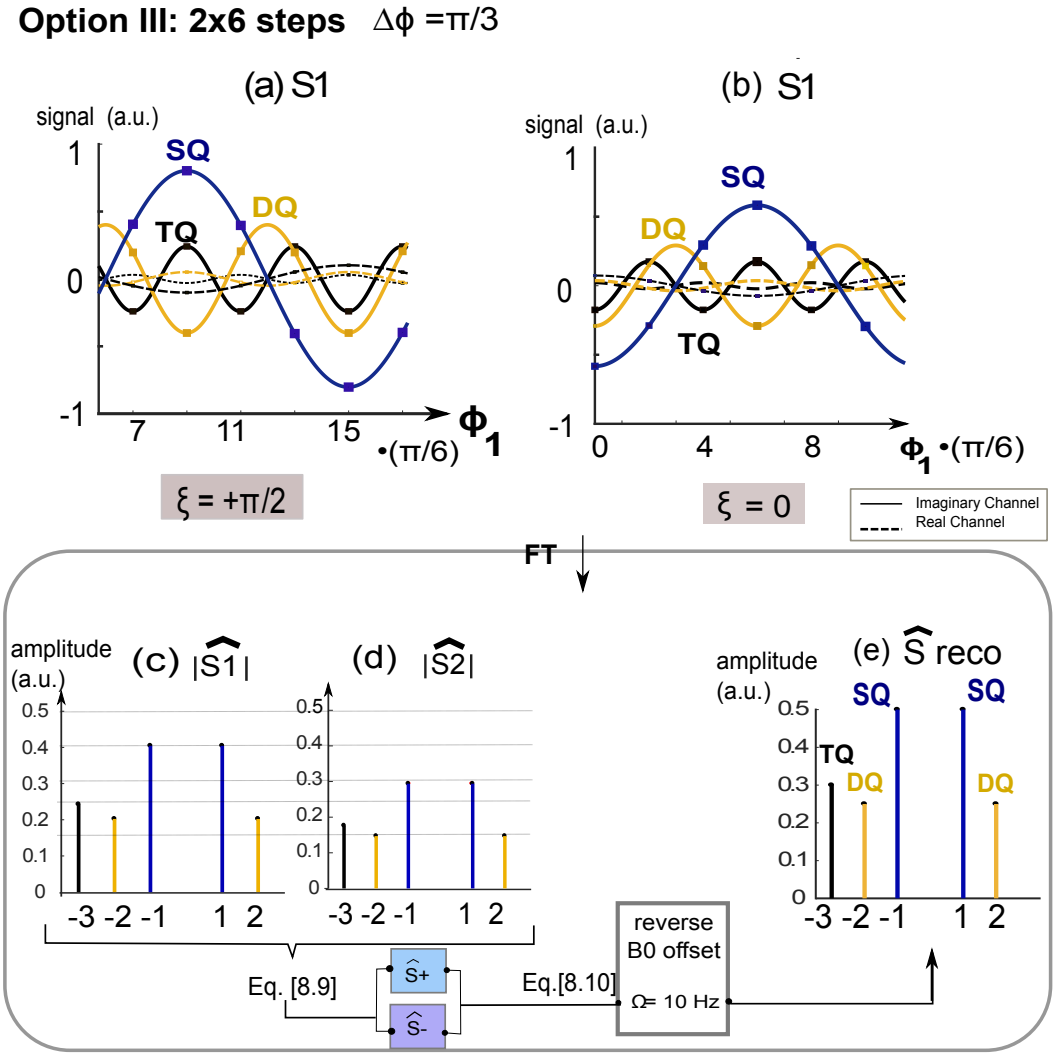

Figure. 6.4: Option3 Phase Cycle and Reconstruction without Relaxation under B0 Offset: To recover from B0 offset bias two cycles were chosen (a) $\xi = \pi/2$, the original phase cycle (b) ξ=0, the additional 6-step phase cycle with the resulting spectra in (c), (d). Their addition and subtraction $\hat{S}_+ + \hat{S}_-$, in combination with a reverse of the known B0 offset results in the recovered Spectrum (e). The amplitudes in e) are the initially set values for the simulation which shows that the signal was effectively recovered, independently of the B0 offset.

Option III: 2x6 steps

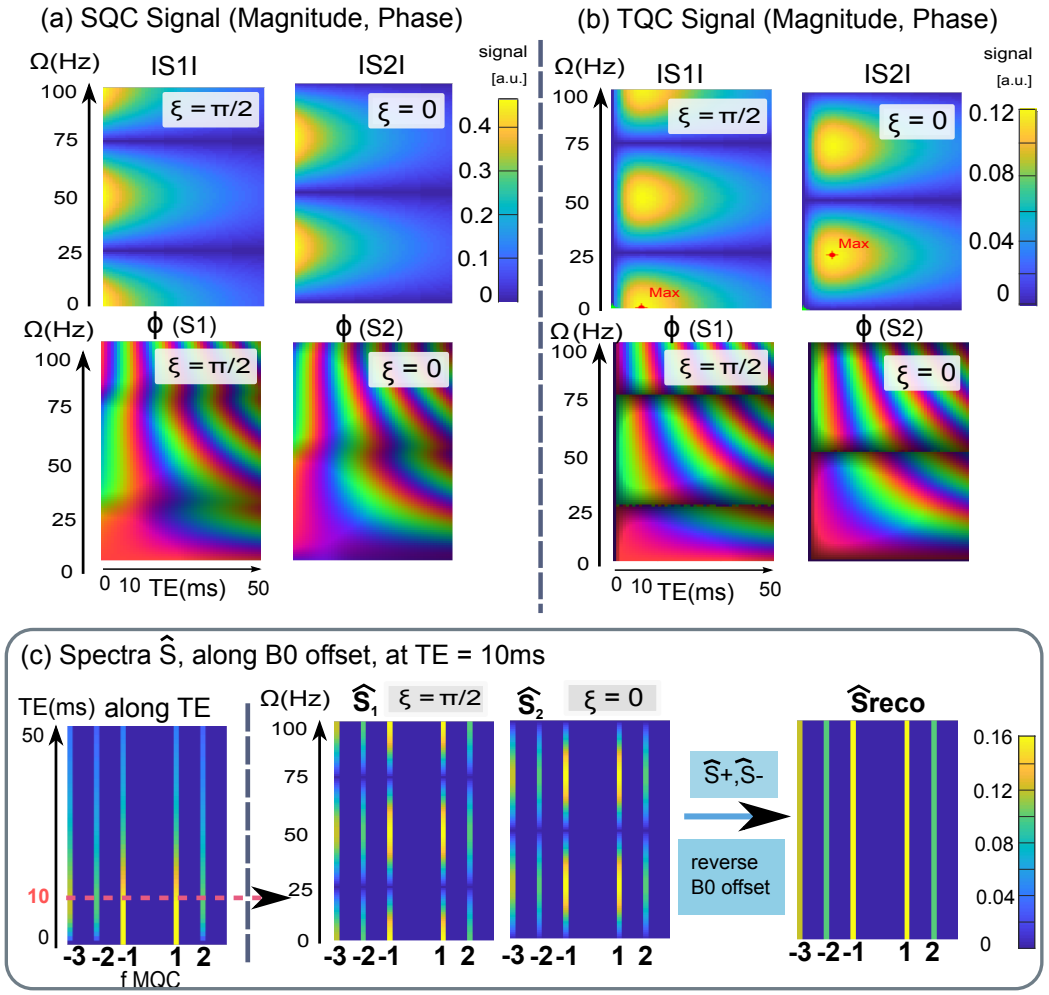

Figure. 6.5: Fleysher cycle, along echo time and varying B0 offset from 0Hz up to 100Hz: Magnitude and phase signal are shown for the SQ and TQ to show the differing oscillation due to B0 offset. This offers the possibility of signal reconstruction, shown in the spectra data below. Further, the second dimension shows the signal evolution with differing signal maxima of SQ and TQ signal along echo time (f). For our set of parameters, the signal in (a) vanished at 25 Hz and 75 Hz offset. In (b) the signal vanished at 0, 50 and 100 Hz. Eventually, the reconstructed spectrum is independent of the B0 field offset.

6.4 Stimulated echo bias

Fourth, the phase cycles for stimulated echo (STE) mitigation, proposed for the SISTINA sequence, were simulated (Figure 6.6). The STE signal can potentially bias SQ signal measurement. The STE signal overlaps with SQ signal and showed a relative maximum signal of 0.16 (red cross) at an echo time of TE= 10 ms which coincided with the maximum signal of the TQ signal. This was analytically expected due to the maximum signal at TE equal evolution time τ_1. STE phase signal is opposite for the phase cycles that were proposed by SISTINA and thus the sum of the complex STE signals in the form of $S_{STE} = \sqrt{(S_{1stim} + S_{2stim})^2}$ indeed, cancels out.

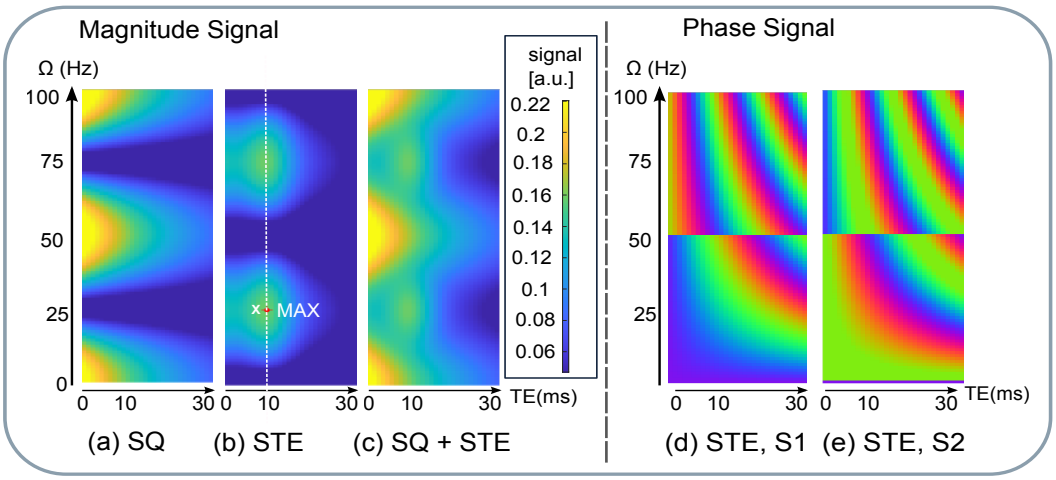

Figure. 6.6: Stimulated Echo Signal Biases under B0 Inhomogeneity and Relaxation: SQ and Stimulated echo (STE) signal for varying echo time (TE) from 0ms to 30ms (x-axis) and varying B0 offset from 0 to 100Hz (y-axis). (a) SQ Signal without STE signal bias, (b) shows only the STE signal, with the expected maximum at 10ms which coincided with the set evolution time tau1 (c) shows the SQ signal with STE signal bias. (d, e): for varying echo time (TE) from 0ms to 30ms (x-axis) and varying B0 offset from 0 to 100Hz (y-axis). (d), (e) show the for the phase cycle 1 and 2. It can be observed that the phases are opposite are opposite of each other.

However, considering STE signal expression, one can observe that STE is independent of Φ_1 as its phase term is $e^{?i(p_1(m)\Phi_1+(0-p_1(m)\Phi_2)} = e^{ip_1(m)\xi}$. Thus, STE signal can be considered as a “zero-quantum coherence" (ZQ) signal. For both options 3 and 4 the STE signal bias was simulated (Figure 6.7). In Figure 6.7l the STE signal bias was mitigated by reconstruction of the respective B0 offset. The alternatively proposed sum of squares magnitude reconstruction still showed the STE signal as an offset. A sum-of-squares reconstruction was performed as indicated in the SISTINA publication. Figure 6.7 shows the signal from the four SISTINA cycles as

noted in Figure 5.2. $\hat{S}_3$ and $\hat{S}_4$ appropriately compensate for the B0 offset in S1 and S2 as shown in their reconstructed combination $\hat{S}_1 + \hat{S}_3$ (Figure 6.7f). STE signal still remains as an offset after sum of squares reconstruction of S1 and S2. Finally, Figure 6.7g shows the full reconstruction using all four cycles, which shows a higher SNR due to averaging.

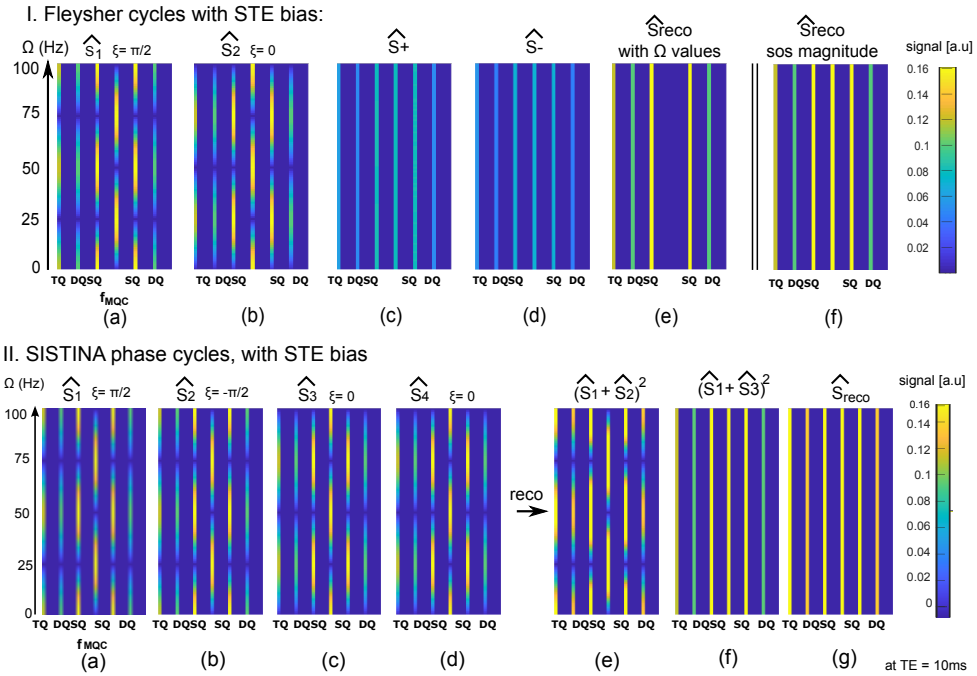

Figure. 6.7: Spectra with STE signal bias at echo time TE = 10 ms and varying B0 offset from 0 to 100Hz (y-axis). The STE signal bias appeared at the zero-frequency in Fourier domain. **I.** Fleysher cycles with reconstruction using B0 values leads to full recovery with no offset. Alternatively, a sum of squares reconstruction did not remove the STE offset. **II.** SISTINA phase cycles were simulated with STE signal. On the right of the arrow the spectra were reconstructed from the data (a-d) (e) magnitude reconstruction of S1 and S2. (f) magnitude reconstruction of S1 and S3 (g) magnitude reconstruction of all four contributions. STE signal was not removed in the reconstructions and still visible in the zero frequency.

6.5 Simulation Summarizing Thoughts

This chapter has reviewed the three key aspects of phase cycle simulation under B0 offset and relaxation effects. Recapitulating the simulation results, it appears crucial to compensate for B0 offsets while STE is inherently isolated upon Fourier transform of the MQC signals, as is DQ. An efficient choice for MQC measurements is thus Fleysher's 2x6-steps phase cycles. However, SISTINA's design offered an interesting addition by electing for a multiple-echoes readout to sample MQC signals along time albeit in a larger raster time than TQTPPI. Therefore, the combined design of 2x6-steps phase cycles and a multi-echo Cartesian Single and Triple quantum Imaging of sodium (^{23}Na) (i.e. CRISTINA) was implemented and investigated on a phantom in the following.

7 Methods III: Development of CRISTINA, a clinical multi-quantum imaging sequence

7.1 Clinical TQTPPI Spectroscopy

The preclinical TQTPPI, global spectroscopy sequence, was transferred to the human scanner and tested on agar phantom of agar concentrations (0% to 5%) with sodium concentrations in the range of 50 mM to 154 mM. Additionally the sequence was tested on 9 healthy volunteers in the brain. Measurement was done with a double resonant ^{23}Na, ^{1}H transmit, receive birdcage, head coil. The acquisiton time of the spectroscopic TQTPPI sequence was 2.3 min. $\Delta\Phi$ was set to 45° and the 2x8step phase cycle was used for comparison to the preclinical results. A total of 34 phase cycles was measured for averaging.

Table. 7.1: TQTPPI sequence parameters at clinical scanners

Parameter	7T	3T
TR	300 ms	200 ms
$\tau_1, \Delta\tau_1$	0.5 ms , 200 μs	0.5 ms , 200 μs
90° pulse duration	500 μs	200 μs
τ_2	150 $\pm$ μs	150 $\pm$ μs
Phase cycles	16	20
$\Phi_{1,t=0}, \Delta\Phi_{1,t=0}$	90°, 30°	90°, 30°
acquisition time	2min 30s	1min 36s

7.2 Imaging Sequence Requirements

The simulation insights were transferred by developing an efficient sequence for clinical scanners. Several considerations had to be made for developing a sequence with the aim to use on healthy volunteers as well as on patients. First, the specific

absorption rate (SAR) limits, defined as the absorbed RF poser per mass and is measured in watts per kg (W/kg), have to be respected and guideline limits for the head are around 3W/kg/10min. Lengthening the rectangular pulse widths of the second and third pulse reduced RF power, especially by lengthening the pulse width of the first sinc-shape pulse. The sinc-shape pulse was chosen as standard method for slice selection, to choose a rectangular slice. The Fourier Transform of the sinc is a rectangle, hence this is an optimal pulse choice for slice selection. The second point was the overall sequence acquisition time. A time proportional phase increments, is clinically not feasible due to acquisition time length. Moreover for simulation settings the optimal evolution time, τ_1, for TQC signal was in the order of 10 ms using clinical T2 relaxation values. This value can be estimated individually by a pre-measurement with the global TQTPPI spectroscopic sequence (2min) a subsequent fit. It remains an estimation due to the global sequence. The fixed evolution time, at the optimal evolution time corresponding to the TQ signal maximum, then features the optimal signal measurement.
A multi echo Cartesian MQC imaging sequence, "CRISTINA", was developed that features the possibility of easy switching between different phase cycle choices by variable Φ_0, $\Delta\Phi$ and phase shift ξ. A cartesian readout was chosen for efficiency and ease of reconstruction, as well as the fact that the TQC signal of interest is maximal at a later echo time (Chapter 6). The multi-echo implementation allows efficient signal capture of both TQC (later echo times) and SQC (early echo times). The parameters of the presented measurements can be found in Table 7.2. The full phase cycle of 2π was repeated N times. The image resolution was increased by 4 fold zero filling. The phase cycles of Option 3 were chosen. Moreover, a B0 map can be calculated directly from the multi-echo phase data: Knowledge of the B0 inhomogeneity enabled a voxel wise reconstruction with the acquisition of two phase cycles ($\xi_1 = \pi/2$ and $\xi_1 = 0$). A phantom, consisting of 8x60 ml tubes with varying concentrations of agarose (0%-5%) and sodium (50-154 mM) was imaged at 3T and 7T (Siemens Magnetom) with a 1H/23Na Head coil, 1Tx/1Rx.

7.2.1 CRISTINA Multiple echo signal acquisition

The multi-echo 2D Cartesian Imaging sequence for SQ and TQ ^{23}Na (CRISTINA) was developed (Figure 7.1). Multi echo data acquisition allowed to follow the characteristic signal evolution of SQ and TQ coherences simultaneously, and reconstruct B0 map on the same data set. A processing pipeline was designed to combine the two phase-cycles with the B0 map, then fit the multiple echo times and finally retrieve SQ, TQ amplitudes and relaxation times, free of B0 and STE biases. Sequence

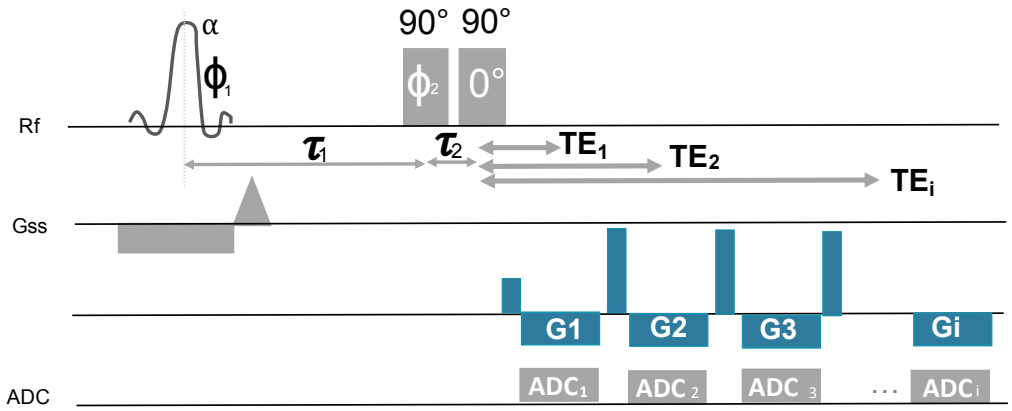

Figure. 7.1: CRISTINA 2D multi-echo sequence, multiple-coherence imaging scheme, featuring a slice selective excitation sinc pulse

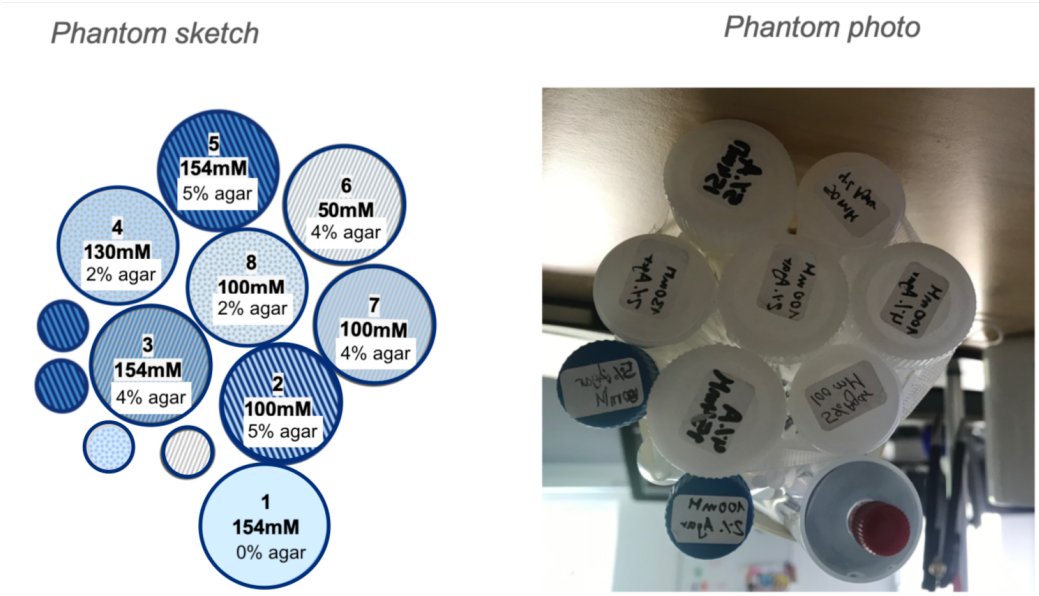

Figure. 7.2: Multi-Tubes Agar Phantom: the phantom, consisted of 8 phantom tubes of filling size 100ml and 4 phantom tubes of filling size 14ml with varying Agar and sodium concentration.

performance was assessed on agarose phantom and in 5 healthy volunteers at 7T(Siemens Magnetom) for the brain with a $^{1}H/^{23}Na$ Head coil, 1Tx/1Rx. Agarose phantom was comprised of 8x60 ml tubes with scaled agarose (0%-5%) and sodium content (50 mM-154 mM). Measurement parameters: 48x32 matrix, zero-padded to 128x128 for reconstruction, FOV=230mm^2 (250 mm^2(in vivo) for one 20 mm slice. In vivo, phantom vials were positioned next to the head: (Left:4%50 mM and 4%100 mM, Right:2%100 mM).The bandwidth was 330Hz/Px(400Hz/Px in vivo), resulting in a minimum echo time of 1.15 ms(1.13 ms in vivo) by allowing asymmetric

Table. 7.2: CRISTINA Sequence Parameters

Parameter	Phantom Scan HighResolu 7T	Phantom Scan 3T	In-vivo Scan 7T	In-vivo Scan 3T
N full phase cycles	10	30	12	30
Matrix Size	48x32	22x20	48x32	22x20 to 24x28
Matrix Size after zero filling	128x128	80x80	128x128	80x80
2D Slice thickness	20 mm	20 mm	20 mm	20 mm
$\Delta\Phi$	30°	30°	30°	30°
N Echoes	20	20	25	20
TE minimum	1.15 ms	1.13 ms	1.13 ms	1.13 ms
ΔTE	2.88 ms	2.88 ms	2.88 ms	2.88 ms
τ_1 †	13.3ms	13.3ms	10-13ms	13ms
TR	390	170-290	390	170-290
scantime per cylce	29 min	24 min	29 min	24 min

The table states the relevant parameters of the CRISTINA sequence to obtain the images presented.
† measured by TQTPPI global spectroscopy sequence with $\Delta\Phi = 30°$.

k-space acquisition. The subsequent 19(24 in vivo) echoes were fully sampled with a ΔTE of 3 ms.

7.2.2 Multiparameter Maps by Fit

Adding multiple echoes after the third pulse eases the capture of optimal TQ signal (TE =τ_1) and facilitates fitting of the signal to obtain T2* values. $T2^*_{slow}$ and $T2^*_{fast}$ maps were obtained by a subsequent voxel-wise multi-parametric fit of the SQC and TQC signal evolution Equation 5.3 and Equation 5.5 using GlobalSearch in Matlab with the fmincon solver to find a minimum of the multivariable function. The value of TQC at TE = 0 ms is zero from theory and was added to the multi-echo data to enhance the fit. The SQC signal at TE = 0 ms was obtained by extrapolation of the fit result, thus enabling an estimate of a zero-TE sodium signal.

8 Results III: Clinical Results at 3 T and 7 T

8.1 Spectroscopic TQTPPI measurement

8.1.1 Phantom Results

Figure 8.1 shows the TQTPPI spectra of three agar phantoms, 154mM Na, measured at the 3T clinical scanner. The resulting spectra of 0 % agar does not show a TQ signal, as expected. The 2 % and 5 % agar phantoms showed a TQ signal of 25.2 % and 54.0 %, normalized to the signal of the SQ transition. This result shows that TQTPPI global spectrum can be measured with sufficient signal to noise ratio on human 3T scanner.

Table. 8.1: TQTPPI spectroscopic results at 3T

Phantom	A_{SQS}	A_{SQL}	A_{TQ}	$\frac{TQ}{SQ}$ [%]	$\frac{TQ[\%]}{\sigma}$	$T2_l^*$ ms	$T2_s^* ms$	t_{TQ} ms
0 %,154 mM †	0.5	0.5	-	-	-	50.0	50.0	-
2 %,50 mM	0.33	0.73	0.27	33.0	26	30.6	8.0	14.5
2 %, 77 mM	0.27	0.71	0.26	27.5	42	36.3	10.7	17.7
2 %, 100 mM	0.31	0.7	0.24	25.2	53	41.5	11.2	19.3
4 %, 50 mM	0.36	0.62	0.31	50.1	25	28.4	4.5	9.7
4 %, 100 mM	0.34	0.66	0.36	43.6	53	21.8	6.3	11.3
5 %, 154 mM	0.42	0.6	0.39	54.0	42	22.3	4.6	9.7

The table gives the fit results after TQTPPI experiment for the individual agar phantoms. $T2_l^* = T2_{long}^*$; $T2_s^* = T2_{short}^*$, t_{TQ} gives the time for the maximum TQ signal. The $TQ[\%]/\sigma$ gives the signal to noise ratio of the TQ signal, by dividing the signal strength of the TQ signal by the standard deviation of the noise region of the spectrum. †The liquid phantom exhibited mono-exponential decay as expected from theory and agrees with the value reported for CSF [49].

Comparison of the spectroscopic result with and without incrementing the evolution time is presented in Figure 8.2. The TQTPPI signal along evolution time, showed the typical oscillating and relaxing signal. The biexponential decay rate, and the evolution time resulting in the highest TQ signal, was obtained by a fit on the TQTPPI data. The TQTPI spectrum was then measured with a fixed evolution time signal along multiple phase cycles to match the data size of the TQTPPI signal data. In

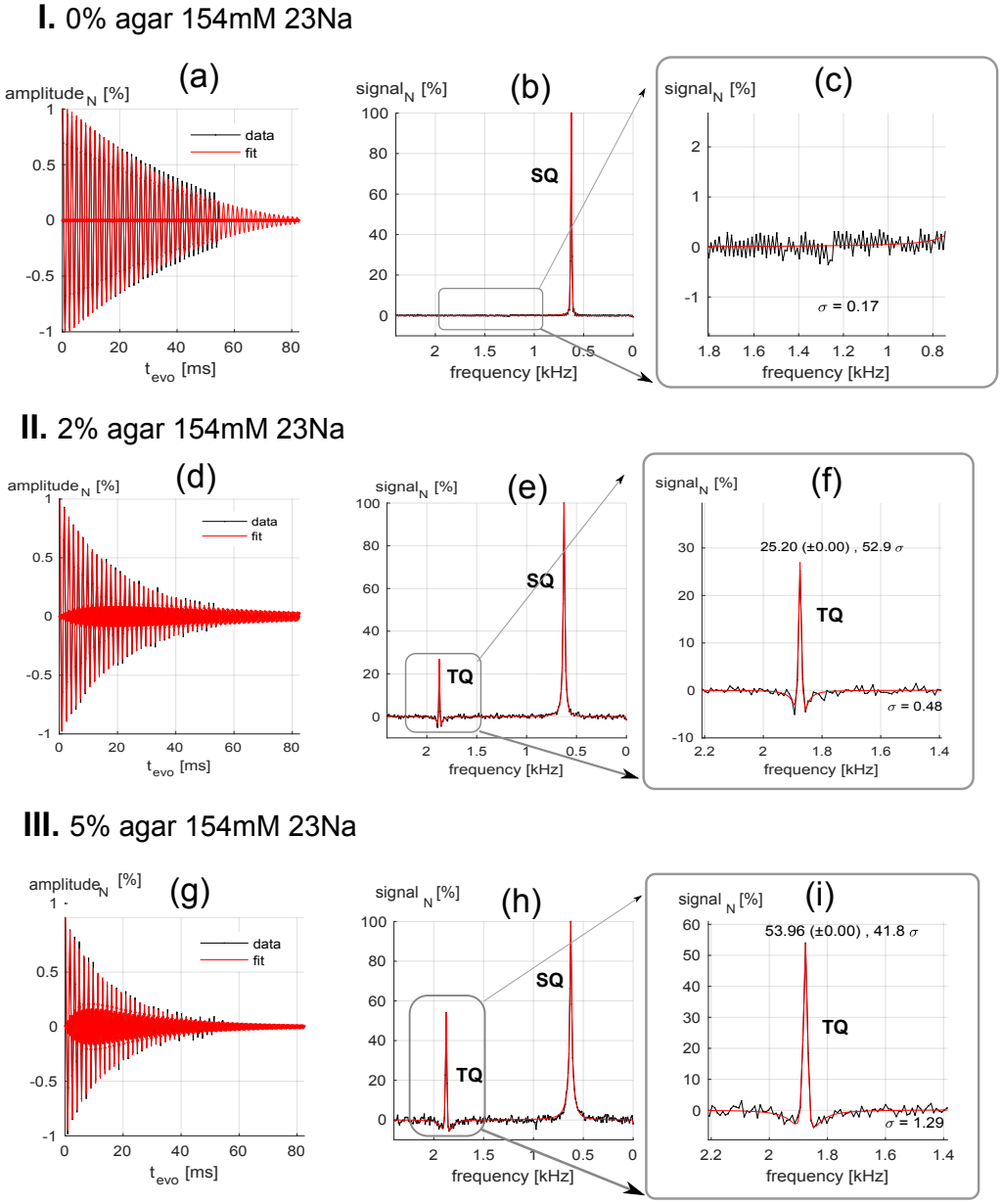

Figure. 8.1: The TQTPPI signal and spectral results along with the respective fit are shown for three phantoms at 3T: I) 0% agar and 154mM ^{23}Na, II) 2% agar and 154mM ^{23}Na, 5% agar and 154mM ^{23}Na. The left column shows the measured TQTPPI signal (black) as well as the fit result (red). The middle column depicts the spectrum with the TQ and SQ transitions. For better visibility the TQ spectrum is shown enlarged in the right column along with signal intensity, the noise level and the comparison of the TQ signal strength to the noise level.

principle one full cycle of 2π gives all information. Measurement of multiple cycles also had the effect of increasing the SNR. The resulting signal along phase-time showed an un-dampened sinusoidal signal, while stepping through the phase cycle. Finally the convolution of the bi-exponential decay with the fixed evolution time data

is depicted in the figure, showing the same signal evolution as the TQTPPI FID. In (b) the absolute and real spectra are shown. The amplitude was obtained by Fourier transform and normalization to the data size, giving the exact amplitude values. Higher signal to noise ratio was found for the fixed evolution time measurement, compared to the TQTPPI spectra and the Fourier transform of the convoluted signal.

Sinc-Pulse versus Rectangle pulse excitation:
For the development of a 2D imaging sequence a localizing first pulse is necessary. For a rectangular slice selection a sinc shape, $sinc(t) = sin(t)/t$, pulse is usually chosen due to the Fourier Transform relationship that transforms a sinc into a rectangle. The spectroscopic TQTPI sequence sequence was compared for a rectangular excitation pulse and a sinc excitation pulse. The comparison was done at 3T at the two sites, Mannheim and Marseille. It can be seen that the sinc pule excitation is less efficient in exciting the signal that is the starting point of the coherence transfer. Nevertheless signal to noise ratio is sufficiently high that the sinc pulse excitation was deemed acceptable in order to pursue the localization of the signal in an imaging sequence.

Table. 8.2: TQTPPI for SINC and RECT pulse excitation

Pulse	N	A_{SQS}	A_{SQL}	A_{TQ}	$\frac{TQ}{SQ}$ [%]	$\frac{TQ[\%]}{\sigma}$	$T2_l^* ms$	$T2_s^* ms$	$t_{TQ} ms$
45° increment measured at 3T, Mannheim									
Rect	30	0.49	0.54	0.15	17	95	29.0	5.3	11.4
Sinc	20	0.48	0.59	0.10	11	32	29.2	5.9	14.7
30° increment measured at 3T, Marseille									
Rect	20	0.53	0.50	0.15	6	35	27.1	5.72	11.4
Sinc	20	0.36	0.71	0.08	5	19	27.5	6.7	13.8

The table gives the comparison of sinc and rectangular pulse excitation measured on the agar phantom. $T2_l^* = T2_{long}^*$; $T2_s^* = T2_{short}^*$, t_{TQ} gives the time for the maximum TQ signal. The $TQ[\%]/\sigma$ gives the signal to noise ratio of the TQ signal, by dividing the signal strength of the TQ signal by the standard deviation of the noise region of the spectrum. N cycles were measured.

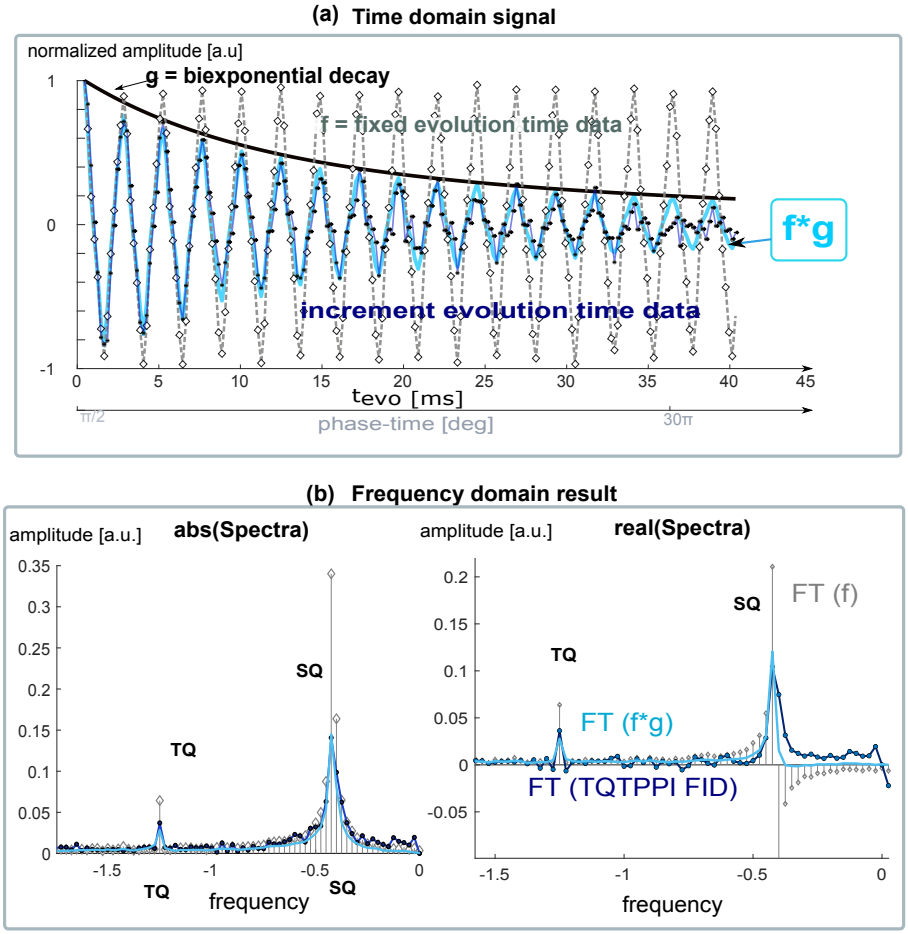

Figure. 8.2: Comparison of incrementing the evolution time and fixed evolution time: (a) the fixed evolution time is the not dampened sinusoidal signal which goes along phase-time. The unchanged evolution time results in the steady maximum amplitude for repeated phase cycles. The TQTPPI with evolution time increment shows the typical oscillating and relaxing signal. The fitted bi-exponential decay, convolved with the fixed evolution time data, results in a signal similar to the TQTPPI FID. (b) shows the absolute and real spectra. It is visible that the fixed evolution time data show a higher signal to noise ratio compared to the TQTPPI spectra and the Fourier transform of the convoluted signal. The real part of the spectra on the right highlights, the characteristic shape of the triple quantum signal, following a double Lorentzian shape has its origin in the bi-exponential decay.

8.1.2 TQTPPI fit result in-vivo Brain

Table. 8.3: TQTPPI in-vivo brain spectroscopic results at 3T and 7T

HC	A_{SQS}	A_{SQL}	A_{TQ}	$\frac{TQ}{SQ}$ [%]	$\frac{TQ[\%]}{\sigma}$	$T2_l^* ms$	$T2_s^* ms$	$t_{TQ} ms$
3T - Mannheim								
29y, f	0.5	0.5	0.10	11.0	59	33.7	4.8	11.3
28y, m	0.8	0.2	0.14	11.0	59	46.5	2.0	7.0
3T - Marseille								
27.34y, m	0.8	0.2	0.10	11.5	36	50	2.3	7.4
28.3y, f	0.7	0.3	0.11	14.2	75	43	3.3	9.0
7T - Marseille								
1. 19.6y,m	0.7	0.3	0.14	14.2	75	38.5	3.2	8.5
2. 38.5y,f	0.7	0.3	0.13	16.4	150	29.4	3.5	9.1
3. 21.0y,m	0.7	0.3	0.15	18.4	123	35.9	3.9	10.1
4. 33.5y,f	0.65	0.4	0.14	19.1	121	39.5	4.2	10.9
5. 34.9y,f	0.73	0.3	0.12	15.2	101	42.3	3.4	9.3
mean	0.7	0.3	0.13	11.9 (3T) 16.7 (7T)	57(3T) 114 (7T)	39.9	3.4	9.2
std	0.09	0.09	0.02	1.5 (3T) 2.1(7T)	16 (3T) 28 (7T)	6.4	0.9	1.4

$T2_l^* = T2_{long}^*$; $T2_s^* = T2_{short}^*$, t_{TQ} gives the time for the maximum TQ signal. The $TQ[\%]/\sigma$ gives the signal to noise ratio of the TQ signal, by dividing the signal strength of the TQ signal by the standard deviation of the noise region of the spectrum. y stands for year and f for female, m for male, HC for Healthy Control.

It can be seen that the maximum TQ time does not vary much between subjects and also for different field strengths with 9.2±1.4 ms. The global TQ/SQ signal increased by 40 % for 7T compared to 3T and also the Signal to noise level increased (σ values) by 99 %.

8.2 CRISTINA multi-echo Phantom results

Figure 8.4 shows the raw images (a) acquired from the two phase cycles, and the post-processing results with SQ and TQ images over echo time (b, c) as well as the total reconstructed SQ and TQ images with B0 map values. Further the fit results are presented in Figures 8.4 (g-j). Exemplary the reconstruction pipeline is also given for one single voxel for better comparison to the simulation results (Figure 8.5). The estimated τ_1 from a TQTPPI global spectroscopic pre-scan (scan time ≈2 min 30 s) was 13.3 ms. Two series of 4D images were obtained with the dimensions being x, y, TE and Φ_1. The Fourier transform along the repeated (x10) phase cycle dimension Φ_1 over the complex signal images showed the MQC spectrum as anticipated from the simulations. Selecting single and triple quantum coherence frequencies, the SQ and TQ images were reconstructed. Subsequently, $\hat{S}_+$ and $\hat{S}_-$ were calculated, as well as a B0 map from the phase images. Eventually, total SQ and TQ signal images were reconstructed for each TE. A subsequent multi-parametric fit for the SQ and TQ signals (Eq.5.3, Eq.5.5) was performed voxel-wise along the echo time data, enhanced by the prior knowledge of TQ being zero at TE = 0 ms. The results are presented in Figure 8.6. The SQ signal evolution fit over the multiple echo times allowed for extrapolation of the SQ signal to TE = 0 ms where tissue sodium concentration (TSC) in mM was determined by a linear fit of signal vs sodium content. The TQ signal image is shown for TE= τ_1 = 13.3 ms. Exemplary, the signal evolution measurement data with the corresponding fit results are shown for the 8 center voxels of the phantom vials along TE, in range of 0 to 60ms, separately for the SQ and TQ signal (Figure 8.6). The characteristic signal evolution of SQ and TQ signals from the simulation was confirmed. Eventually, $T2^*_{fast}$ and $T2^*_{slow}$ maps, were produced from the multi-parameter fit with values in the range of 0-12 ms for $T2^*_{fast}$ and 15-30 ms for $T2^*_{slow}$. Moreover, the fitted values were evaluated in a circular region of interest of phantom size for the 8 phantom tubes independently (ROI8). The liquid phantom vial followed a mono-exponential decay with (1.7±2.4) ms $T2^*_{fast}$ and a $T2^*_{slow}$ of (15.0±2.9) ms. The 2% agar vial in the center showed elevated $T2^*_{fast}$ values in the range of (11±2.7) ms and lower $T2^*_{slow}$ values of(21.9±3.1) ms compared to the 4% and 5% agar phantoms with $T2^*_{fast}$ in the order of 5 ms and $T2^*_{slow}$ in the order of 27 ms. Further, mean sodium concentrations and its standard deviations were evaluated in eight regions of interest(circular size, few pixels smaller than the phantom), in the SQ image at TE = 0 ms and the values were plotted against signal strength. Figure 8.6 shows a linear relationship for the SQ signal against TSC (R^2 =0.75, p-value = 0.006) as well as for the ratio TQ over SQ signal against agar

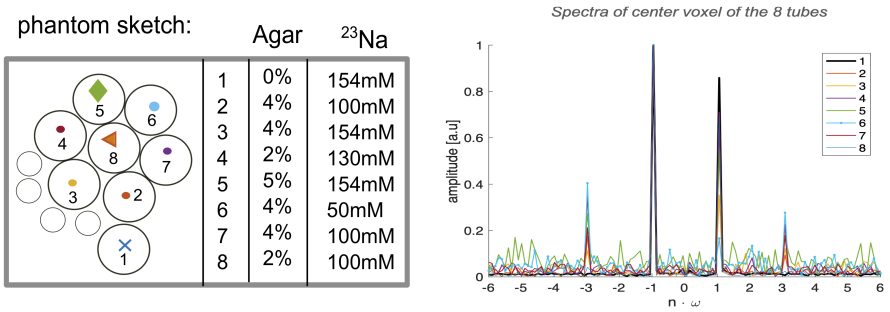

Figure. 8.3: Agar Phantom and Exemplary Spectra: The phantom composition is presented along with a representative spectrum of a center voxel of each tube, taken from the CRISTINA dataset to build the connection of understanding to the preclinical and spectroscopic results.

concentrations (R^2 =0.87, p-value = 0.0007). Higher signal strength was observed for increased agar content, regardless of the sodium concentration.

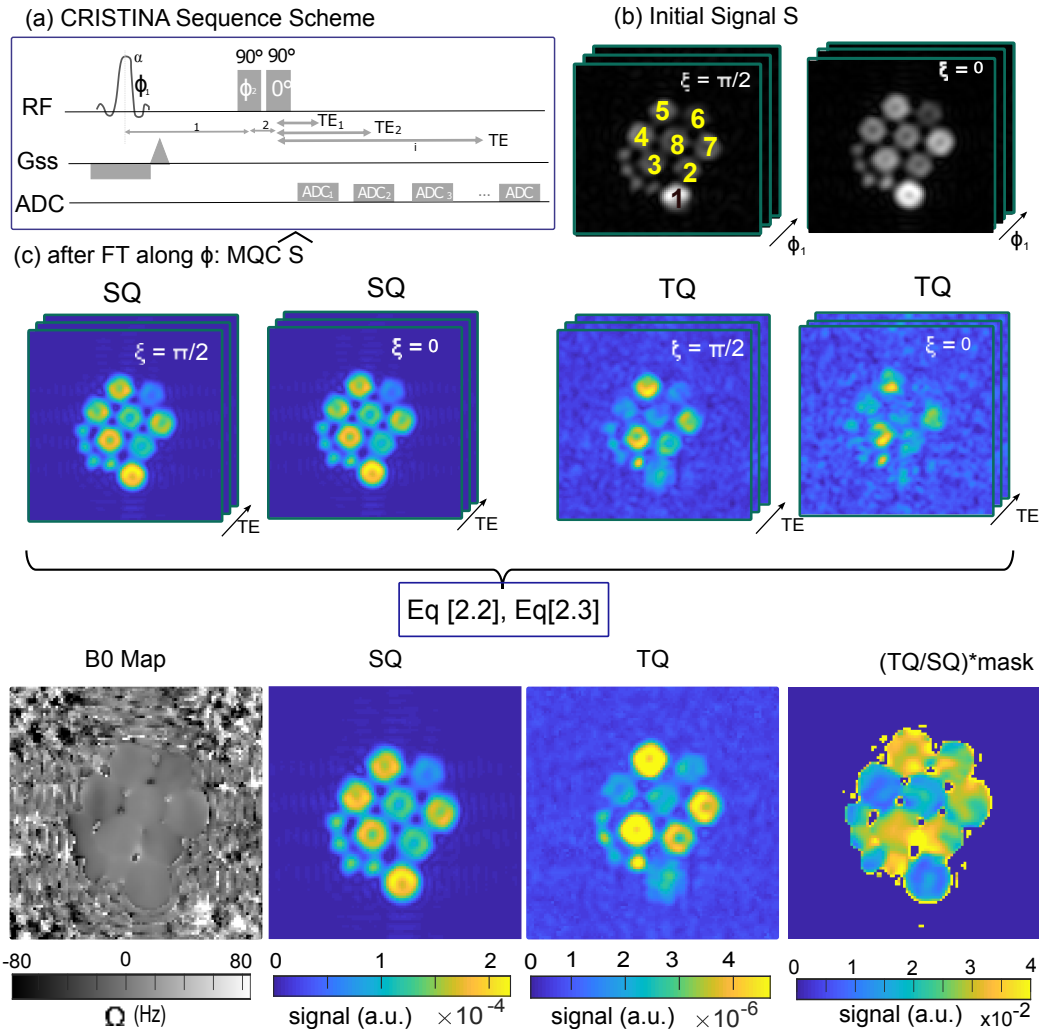

Figure. 8.4: Measurement data and subsequent post-processing pipeline: a) Initial signal of the two independent phase-cycle sets. The multiple slices indicate that the 2D slice is measured multiple times with stepping through the phase cycle for one TE. On the same height the box shows the initial, complex, sinusoidal signal for a single voxel. b) Fourier Transformation along the phase-axis. This results in a characteristic spectrum for each voxel. Here the multiple slices indicate, that the measurement is performed in multi-echo mode and giving a 4D data set (x, y, spectrum, TE). c) The B0 map reconstruction results from the multiple echo data. Finally the total SQ and TQ image is along TE shown by choosing the frequency of the SQ and TQ transitions.

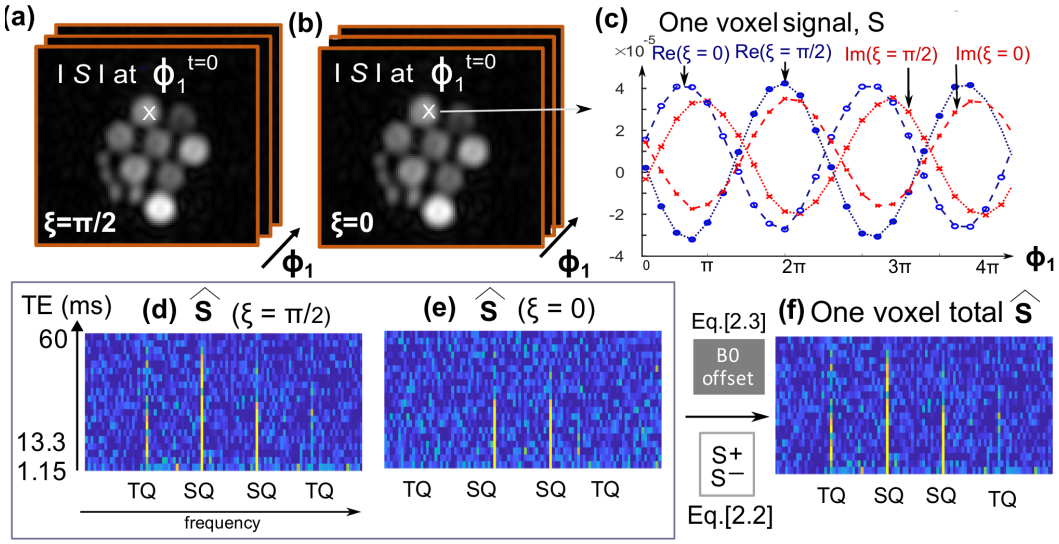

Figure. 8.5: One Pixel CRISTINA Result: For comparability to simulation results, the one pixel result shows the spectra for the two phase cycles with TQ and SQ signal along TE as well as the reconstruction. Also the difference and advantage in using POCS reconstruction can be seen by comparing images (a,b) to the images in Figure 8.4. More details are preserved using POCS. Here the signal without POCS reconstruction was shown for comparison.

Table. 8.4: CRISTINA Phantom Results

Nr	Agar(%)	Na (mM)	$T2_l^*$ (ms)	$T2_s^*$ (ms)	t_{TQ} (ms)	Ratio $(x10^{-2})$*	SQ_{TE1} **	SQ_{TE0} ***
1	0 %	154 mM	22.7 ±2.7	0.9±1.4	3.0	1.0± 0.2	19.8 ± 0.2	21.4 ± 0.2
2	4 %	100 mM	19.6 ±5.7	4.8±0.7	9.7	2.9± 0.4	11.7 ± 0.2	14.6 ± 0.2
3	4 %	154 mM	17.9 ± 2.0	5.0±0.6	12.8	3.0± 0.2	16.1± 0.2	19.7 ± 0.2
4	2 %	130 mM	25.9 ±12.0	3.7±0.5	8.4	1.1 ± 0.2	16.7 ± 0.3	22.7 ± 0.3
5	5 %	154 mM	16.6 ±1.9	4.0±1.0	12.8	3.1± 0.2	16.1± 0.2	20.7 ± 0.2
6	4 %	50 mM	28.1 ±8.4	4.3±0.5	17.0	2.6 ± 0.3	6.6± 0.1	8.3 ± 0.1
7	4 %	100 mM	17.6 ±0.8	4.7±1.2	12.8	2.6± 0.3	15.0± 0.2	19.6 ± 0.2
8	2 %	100 mM	17.6 ±0.8	3.8±2.2	15	1.7± 0.2	11.7± 0.2	13.2± 0.2

$T2_l^* = T2_{long}^*$; $T2_s^* = T2_{short}^*$, t_{TQ} gives the time for the maximum TQ signal. SQ is given at the measured first echo time TE1 = 1.13 ms and at the fitted SQ result for TE=0 ms. *The linear regression model result: R^2 = 0.87 (p-value = 0.0007) . **The linear regression model result: R^2 = 0.81 (p-value = 0.0022) . ***The linear regression model result: R^2 = 0.75 (p-value = 0.0058)

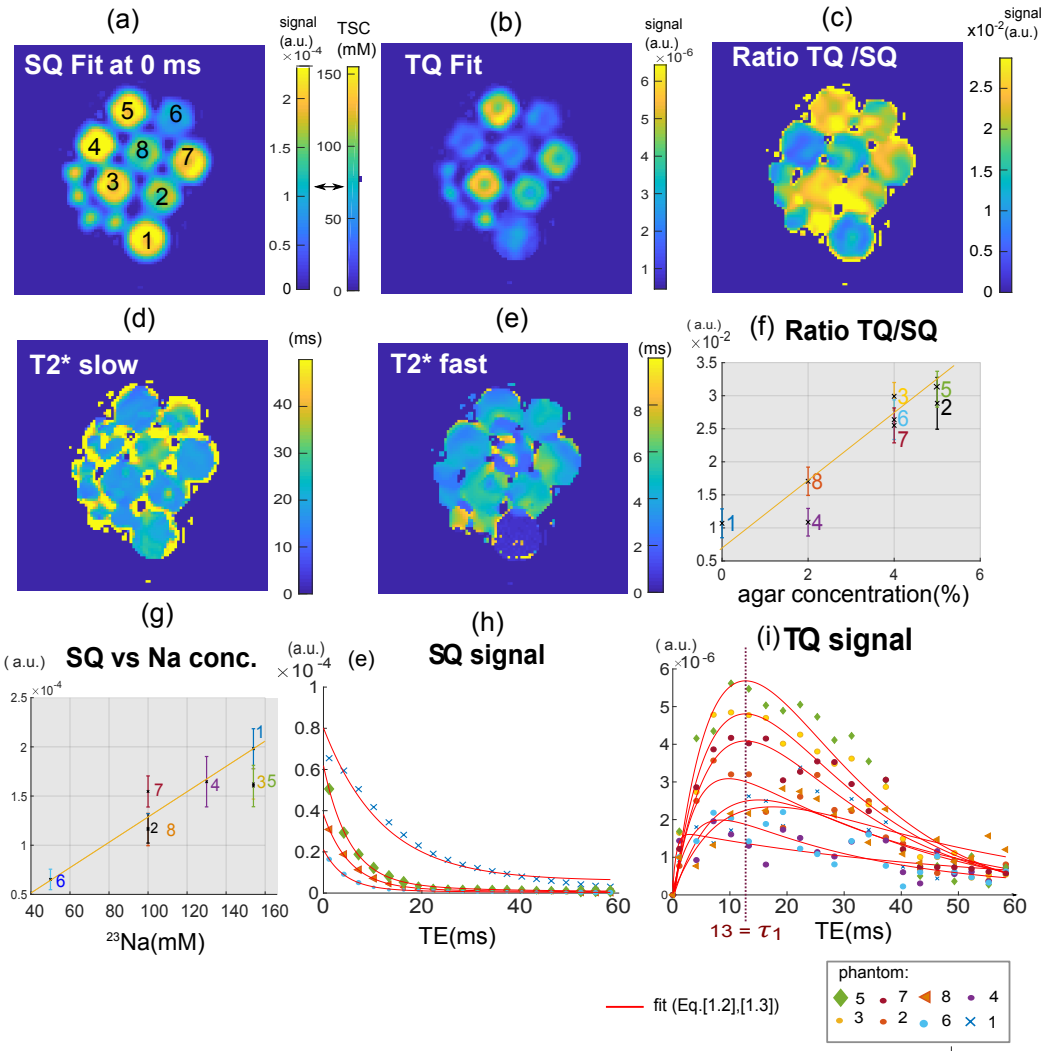

Figure. 8.6: TQ signal and SQ signal Phantom result over TE, Relationship SQ-Signal to TSC(mM) and TQ-Signal to Agarose Content: phantom numbers are shown again in the sketch along with phantom contents. Spectroscopic result for the different phantom tubes is shown for comparison to preclinical results. Center voxel SQ and TQ signal evolution over echo time with respective voxel wise fit. SQ signal is only shown for a selection of 4 tubes with different sodium content for a clearer plot. TQ signal evolution showed the, from simulation expected signal increase until approximative τ_1. Sodium content versus signal strength at interpolated echo time 0 ms shows qualitatively a linear relationship. TQ signal at echo time of 13 ms normalized by SQ signal strength was comparable for the same agar concentrations. Liquid phantom as well as 2 % agar density can be well distinguished from the 4 % and 5 % agar density.

8.3 CRISTINA multi-echo in-vivo results

In Volunteer1 and 5, the skin was notably more visible in the TQ image than in the SQ image. Comparison of volunteers and patients is warranted to discern TQ signal potential variations in diseased tissue.

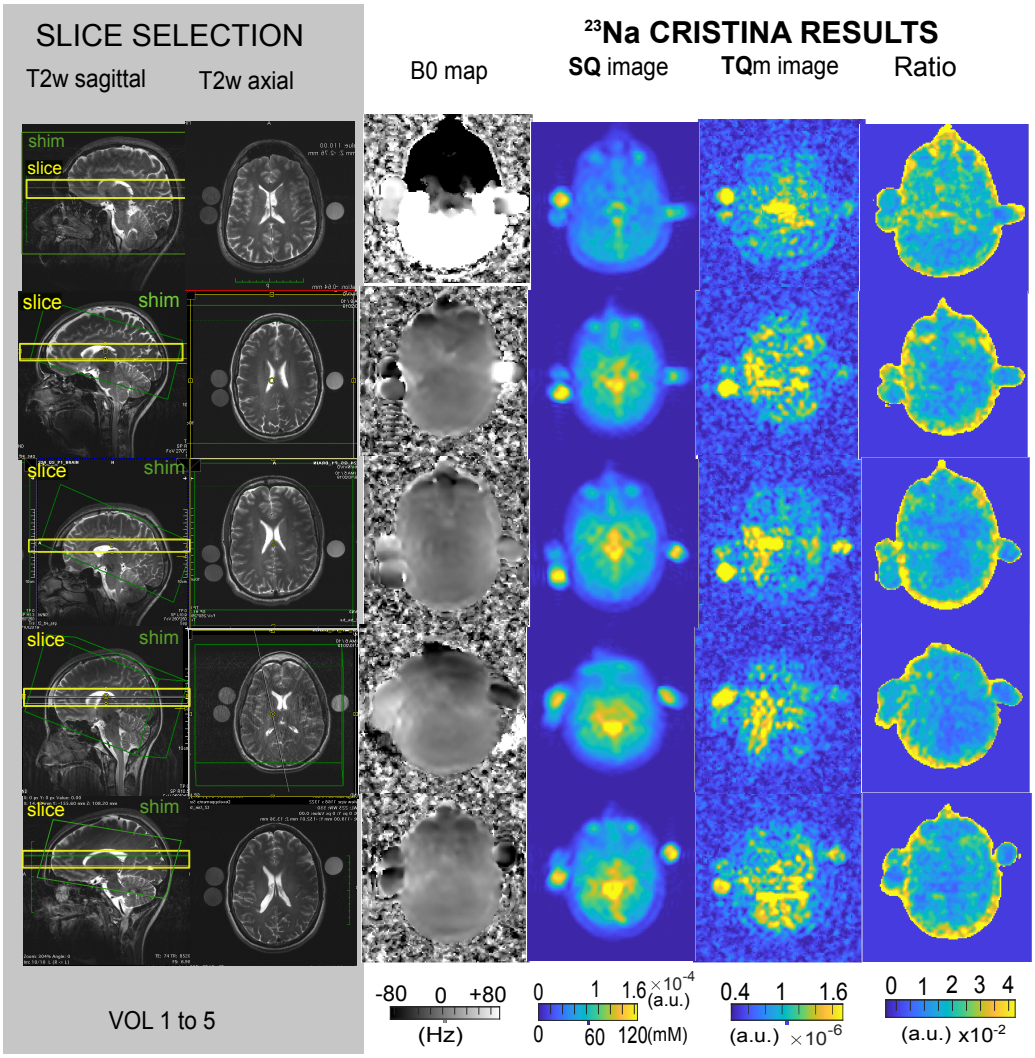

Figure. 8.7: CRISTINA results for 5 healthy volunteers in the brain. 2D slice position and shim volume is shown for a T2 weighted scan. The B0 map was calculated from the first two echoes of the signal along Φ, to reconstruct the total SQ and TQ images along echo time. It shows variations between -150Hz to +100Hz (i.e. multiple B0-induced signal cancellation are expected) and differences between volunteers, highlighting the need for B0 correction. The TQ signal is shown averaged over echo time from 4ms to 21ms for higher SNR.

9 Discussion

The more commonly available higher field strengths open up sodium measurement, and in particular, multi-quantum techniques to a broader community which is why it is important to correctly interpret the signals that are acquired. A deeper insight into the formation of the TQ signal on the cellular level was crucial to establish as a potential biomarker for clinical diagnostics and therapy monitoring. In this thesis the overall aim was to gain further insight into the triple-quantum signal behavior on a cellular level as well as a transfer and development of triple-quantum measurement techniques to the clinics to eventually leverage this signal as a new biomarker for clinical diagnostics and treatment monitoring. This aim was pursued in three different parts. The first part, the preclinical work, comprised an important starting point in order to justify the triple-quantum signal as an important indication for cell vitality and hence give the basis of developing a new biomarker. The result of healthy cells showing a TQ signal whereas dead cells did not is an important finding for future investigations. Moreover, the ongoing discussion of separation extra- and intracellular cell compartments based on the triple-quantum (TQ) signal was addressed by liposomal cell phantoms showing that the TQ signal came from double lipid membrane interaction.

In the second part, a simulation study was carried out, that attempts to explain the coherence transfer mechanisms in the three-pulses sequence in a graphical way, important for the multidisciplinary field of MRI and will be freely available. The understanding of the different options for measuring TQC signal along with the resulting efficient phase-cycling choice is especially important, as sodium MR techniques are on the rise thanks to hardware improvements. Eventually, probing MQC signal in sodium MRI allows to fully capture the underlying physical properties within each voxel. Further, this part served to analyze and find an optimal way of measurement that can withstand common biases of every day clinical MR scans, with the most important being B0 inhomogeneity. Not addressed, the B0 inhomogeneity can lead to serious signal drop outs and therefore might lead to erroneous conclusions in the quantification of TQ signal.

An ideal way of combining existing measurement techniques was found by this simulation study which was confirmed by implementation and measurements in the third part of the thesis. The implemented Cartesian multi-echo, multi-quantum

MR imaging sequence (CRISTINA) fills a gap in the clinical community because its justification is based on simulation and further the reconstruction and signal fitting code will be made freely available. The Cartesian signal acquisition facilitates reconstruction in comparison with radial techniques. TQ imaging sequences are even less common than SQ imaging techniques in clinical trials. An argument for giving important cellular vitality information was delivered in this thesis by the preclinical work which makes clinical TQ signal measurements an important tool.

9.1 Preclinical Findings

A deeper understanding of the connection between the TQ signal and cellular processes was gained from the cell and liposome experiments.
The central question of intra- and extracellular signal separation was addressed by comparing the TQ signal from human HEP G2 liver cells on a microcavity array chip to liposome and nanoparticle solutions. The latter served to model different scenarios of sodium ion encapsulation in a cell like double-lipid membrane structure of liposomes. The liposomes and nanoparticles experiments allowed to interpret the TQ signal formation of the cells. Initially, two types of simple liposome types were envisioned, the first with sodium ions inside the liposomes and the second type of liposomes with water inside. Both being immersed in liquid saline solution. As expected, liposomes with “intra-cellular” sodium ions showed a TQ signal. However, on the basis of liposome results alone TQ signal formation could not be attributed directly to one of the two scenarios: TQ signal arose from: A) the sodium ions that were encapsulated, or B) the sodium ions from extra-liposomal space, in the vicinity of the membrane. Liposomes without sodium ions inside showed no TQ-signal (2σ). This leads to the interpretation, that sodium ion interaction with the membrane from the extra liposomal space does not suffice to result in a TQ signal, given the measurement settings.
Chemical sciences literature reported that sodium ions can be trapped within the negatively charged fatty acids structure of the liposome double-lipid membrane due to the mixing production process and the permeability coefficient of sodium ions and water [40, 99, 100, 101]. A denser packing of the lipids with a change in configuration of the lipid acyl chains was reported [103]. Because the water filled liposomes did not exhibit a TQ signal, a penetration of sodium ions into the cell membrane from extracellular space did not occur despite the strong gradient of extracellular (154 mM) and intracellular (0 mM) sodium. Nanoparticles served to

differentiate TQ signal arising from the entrapped sodium ions within the double lipid membrane structure or the intra liposomal space because nanoparticles show no lipid-bilayer membrane structure. TQ signal was comparable to the reference measurement of the bioreactor filled with cell medium solution. In summary TQ signal in the liposomes was produced by the ions, entrapped within the double lipid layer structure and TQ signal did neither arise due to “intra-cellular" space of the liposomes nor through the interaction of the sodium ions with the membrane from “extra-cellular" space. It has to be noted that the produced liposomes present a greatly simplified version of cells, as cell organelles and membrane proteins are missing. This simplified model facilitated the search of the origin of the TQ signal around biological membranes. A detailed study with physiological intra- and extra cellular protein concentrations could be done in the future.

Bioreactor measurements with HEP G2 liver cells

Three insights were drawn from the bioreactor cell measurements: 1) Vital cells exhibited a TQ signal. 2) Perfusion stop (C_{PS}), leading to a decreased oxygen and nutrient supply, resulted in a lower, but measurable TQ signal. A down-regulation of the metabolism of the cells in the situation of low oxygen supply can be imagined. Re-perfusion of the cells on the third day resulted in a TQ signal close to the original value of the first day. Standard perfusion re-supplied constantly aerated medium with nutrients and oxygen for the cells. The setup was not modified during the perfusion stop and re-perfusion. 3) dead cells which were exposed to air without cell culture medium for about 20 min showed no TQ signal within the sensitivity. Light microscopy confirmed, that the cell constituents were still on the chip, although it is unknown if cell apoptosis destroyed the cell compartments. Reference measurement of the bioreactor showed that the background TQ signal deviated only by one standard deviation from the noise level. These results suggest, that viable cells exhibit a TQ signal, whereas impaired cells do not. Under the lack of nutrients and oxygen, the in vitro cells showed a lower TQ signal strength which was recovered when supply of oxygen and nutrients achieved original values. The recovering TQ signal showed that the cells survived the period of stress. The metabolism change could have affected the transmembrane transport of sodium which is a process that needs energy and resulted in a change in TQ signal strength. Further studies could relate the TQ signal to the sodium-potassium pump directly by specifically blocking it’s functioning with the drug oubain as e.g in [45].

Additional cell line

Further, the TQ signal could be linked to viable versus dead cells, because dead

cells did not exhibit a TQ signal whereas living cells did. This result was confirmed by another cell line, the neonatal cardiomyocytes, where there is an added visual confirmation in the continuing beating of the cell compounds on the microcavity array chip. Experiments were conducted under standard perfusion and perfusion stop conditions to mimic the situation in myocardial infarction, where obstruction of blood flow is observed leading to cell death. A significant TQ signal under standard perfusion was measured which declined in the non-perfusion state, hence the TQ signal could be a potential marker for ischemia as well as for detecting live cells. Isoprenaline stimulation did not show a notable increase in TQ-signal. However, it was reported that Isoprenaline stimulation in cardiomyocytes is affected by culture conditions. Bovine serum which was added to the medium already acts as a stimulator for hypertrophy in neonatal cardiomyocytes. Therefore, cells should be cultured in basal medium to study the hypertrophic response due to Isoprenaline.[90, 92]

Study design limitations

The bioreactor experiments are not without limitations. The human liver cell loaded microcavity array presents a valuable way to study cells in vitro with MR techniques. However, the physiological structure of the 3D cell compound in the bioreactor differs from real human tissue structure. Notably, the extracellular space in this setup is comprised of collagen. This lack of extracellular space, as found in vivo, made it possible to attribute the measured TQ signal to originate from the cells. Due to the difference of the cell culture and real human tissue in an organ, it would be valuable to measure the TQ signal in vivo. Additionally, different cell lines should be measured to transfer the findings from human liver cells to other cell lines. A further limitation is that there was no additional reference used to measure the viability of the cells. Within the presented experimental setup, it is not possible currently to incorporate, e.g., fluorescence microscopy verification in a meaningful way. For microscopy evaluation, the cells have to be taken out of the bioreactor and therefore cannot give information at the same time as the sodium TQ-signal. A dual resonant surface receive coil could facilitate interleaved ^{1}H spectroscopy measurements to get additional insight in the metabolism of the cells, however loss of sensitivity compared to the single resonant sodium surface coil could be problematic given the low TQ signal. Further, the multivariate data fit results present an approximation. The bi-exponential model was fitted to all data, with the fit boundaries enabling mono-exponential decay. This study was not done with toxic shift reagents to separate intra- and extracellular cells.

Single Voxel Localization

With current settings, LOC-S triple-quantum signal was higher for equal voxel size and material than for LOC sequence. However, the latter sequence takes longer before data readout due to the additional 180° pulse which leads to signal drop. Further optimization of the crusher gradients and pulse shapes could reach higher resolution. Increasing the evolution time enhanced the TQ signal due to the difference in relaxation time of SQ and TQ signal. This effect could be phantom dependent because a difference of 2 ms for the optimum evolution time was measured. Especially for localization, where low TQ signal is problematic, it is useful to measure at the optimum time point. The exact time point could be further evaluated in a simulation. Two methods for single voxel localization of the TQTPPI sequence were successfully implemented and validated on phantom and in-vivo rat. Localization performed well in- vitro and in-vivo for voxel sizes of 10x10x40mm^3 without destroying quantum coherences. In-vitro results further showed that a varying agar concentrations with equal sodium concentrations could be distinguished based on the triple-quantum signal with both sequences.

The presented pre-clinical work could be extended to incorporate cell organelles and proteins within the inner compartments of the cell phantoms as well as adding typical external cell proteins on the outside in concentrations comparable to the in vivo situation. Investigating the level of protein concentration that leads to a triple-quantum signal could refine the intra- versus extracellular TQ signal discussion further. This work suggests, that the TQ signal of cells (studied on HEP G2 and cardiomyocytes) could be useful as an indicator for normoxic and thus actively metabolizing cells, reflecting the activity in transmembrane sodium transport. The unique bioreactor setup enabled mimicking of hypertrophy ex-vivo and observation of the corresponding TQ signal. In translation to the clinic, in vivo cardiac TQ signal could provide additional information that relates to cell function.

9.2 Simulation work and clinical transfer

A step forward was the translation of the in vitro cell experiments to human studies, to investigate and possibly classify the TQ signal in healthy and diseased tissue. The rationales for different sequence designs for TQ coherence sodium MRI measurement were considered in a unified formalism, theoretically and graphically. From the improved understanding of the different options, an efficient design was proposed to compensate for B0 and stimulated echo in only 2x6-steps phase cycles.

The proposed CRISTINA sequence further leveraged multi-echo readout to rapidly sample the temporal evolution of MQ coherences. Eventually, CRISTINA data were enhanced by the unified formalism to draw a complete characterization of the sodium signal, including B0, relaxometry, total signal of both SQ and TQ coherences and signal ratio. Although different options have been presented over the last decades, an overview and comparison between the various techniques was lacking. Furthermore, a graphical and intuitive formalism to simulate the techniques of coherence transfer and phase cycling was presented.

Indeed, both T2* relaxation properties and total sodium concentrations can be inferred, provided that a calibrated sample is within the imaging plane. Thus, the pairing of the common theoretical framework which was presented in this thesis with the experimental design for efficient MQC sodium MRI can provide refined tissue characterization and hence diagnostics and treatment monitoring. Simulation results showed that the conventional six step phase cycle is, as expected, most susceptible to B0 inhomogeneity. The additional phase cycle in quadrature for B0 inhomogeneity mitigation effectively alleviates the problem. The TQTPPI method proposed a different second phase cycle to suppress DQ signals. However, the DQ coherence signal is differentiated by Fourier decomposition and ends up at twice the single quantum coherence frequency, whereas the TQ signal ends up at three times the SQ frequency. Therefore, the additional cycle for DQ transfer suppression doubles the measurement time with effectively an averaging repetition of the SQ and TQ signal. The 45° phase increment over samples TQ and misses to capture the full TQ signal amplitude. The Nyquist sampling frequency is twice the highest frequency of interest, resulting in a maximum phase increment of 60° for efficient TQ sampling. Any smaller phase increment results in oversampling and serves to accumulate signal, which can be substituted by averaging. The advantage of the TQTPPI method using time proportional phase increments is given in the possibility of obtaining the T2* long and short values from the fit of the signal along the evolution time without prior knowledge of the optimal evolution time. A standard phase-cycle with fixed evolution time τ_1 and one single echo readout in an imaging experiment cannot provide this information.

The SISTINA design [94] focused on the phase cycle to suppress stimulated echo signals. Although the stimulated echo signal is the highest at the time point of the maximum TQC signal, the stimulated echo signal assimilates to a zero quantum (ZQ) coherence signal, i.e. as a continuous offset, after Fourier decomposition. But the interesting aspect from SISTINA was the multiple echo readout that allows to capture the temporal evolution of both SQC and TQC. From the signals' temporal evolution, a multi parametric fit can model the bi-exponential relaxation and yield

the distribution of the signal in the two T2* compartments. An additional feature of SISTINA is the use of the dead time between the first and the second pulse for one or multiple radial k-space acquisitions with ultra short echo time (UTE) readouts. While these additional measurements can serve to improve the overall SNR, CRISTINA results demonstrated that there is no extra information (notably concerning SQ signal) carried within the UTE signal that cannot be inferred from the later multi-echo Cartesian readout signal. Instead of sum of squares reconstruction a quadrature reconstruction can be beneficial if a B0 map is unavailable. The complex reconstruction involving the B0 map allows to recover the complete signal. Fleysher's two phase cycles choice focused on the B0 offset mitigation. This design effectively helps to retrieve any lost signal and remove STE and DQC signals impact while operating at the Nyquist frequency. Thus, an efficient MQC sodium-MRI sequence design - named CRISTINA - was drawn that benefits from the efficient Fleysher's 2x6 steps phase cycles, in combination with SISTINA multi-echo readout to mimic TQTPPI assumption-free signal sampling.

Experimental Proof of Concept of Multi Quantum Imaging

Sodium MRI is an important active field of research [105, 106, 107, 108, 109] with new coils and clinical studies being published recently. However TQ techniques are not well represented and CRISTINA TQ sequence could be of interest to interpret pathologies. CRISTINA design was empowered by the theoretical formalism to extract MQ signals free of B0, DQ and STE biases. The reconstruction of the acquired Cartesian MQ data can be done straightforward using Fourier transform. B0 can be mapped using a simple least-square fit of the phase data. And a multi-parametric fit results in T2* fast and T2* slow maps as well as quantification values for SQ and TQ signals. The asymmetric echo choice reduced the lowest possible TE to 1.15 ms and with extrapolation of the fit, a TE = 0 ms SQ image can be reconstructed. Therefore, all relevant information for quantification methods can be obtained with the sequence.

9.3 Future Directions

Considerations and open points

Although the standard cartesian gradient echo sequence is much lower in SNR, institutions without the possibility of sequence implementation are limited to this option. Up to now the possibility of measuring sodium images with either density adapted radial (DAR) or twisted projection imaging (TPI) relies on either collaboration or in-house reimplementation. In order to finally drive sodium imaging into the clinic

a consensus of the community is needed on which sequence to focus on so that a vendor version can be discussed. This is crucial for establishing sodium images for clinical diagnosis and therapy monitoring that are valid across different sites and vendors. The easy to reconstruct, multiple-echo multi-quantum sequence, CRISTINA, could be a valid candidate for such a trial. Further optimization remains to be considered regarding acquisition parameters such as TE sampling and receiver bandwidth. Currently, the phantom measurement took 20 min per phase cycle but was chosen with conservative values of 2-fold oversampling the TQ frequency by $\Delta\Phi = 30^\circ$ and measurement of 10 full phase cycles for averaging. The total measurement time of 40 min could, therefore, be reduced by the use of $\Delta\Phi = 60^\circ$ and fewer phase cycles. The matrix size was 48x32 and a subsequent higher resolution was achieved by POCS reconstruction of the first asymmetrically acquired echo and zero filling. Higher resolution acquisitions will be tested at 3 T and 7 T. Moreover, it must be noted that at present, CRISTINA remains a 2D imaging sequence, and for the presented measurement set a relatively thick slice of 20 mm was used. Further, signal processing-based MR reconstruction from reduced data could be investigated to speed up the measurement time [49, 110, 111, 112, 58, 62]. Compressed sensing evolved in interest of reducing scan time by realizing that MR images are sparse and therefore compressible. An accurate reconstruction from an under sampled dataset can be achieved if the artifacts from under-sampling are incoherent and reconstruction of the image is done by a nonlinear method. Especially sodium MRI suffers from long scan times and could benefit from compressed sensing techniques [69].

Machine Learning

Traditional machine learning algorithms in the form of supervised and unsupervised learning (e.g. support vector machine, k-nearest neighbors, linear regression) were proposed for classification on medical images to facilitate objective decision making in the clinic [113, 114]. Especially when different imaging modalities (CT, ^{1}H MRI, ^{23}Na MRI, PET) are combined, a faster and more objective workflow could potentially be established. Deep learning emerged as dominant technique for supervised learning of labeled data and has been shown to yield excellent results in the field of image recognition [115]. Certainly, there is a higher hurdle on the usage of machine learning algorithms for medical imaging as they build the basis of diagnosis and therapy and therefore need to be truthful. Nevertheless, especially with deep learning methods great results have already been achieved in the field of MRI in image acquisition acceleration, segmentation, and establishing a mapping relationship from undersampled to fully-sampled k-space data [116, 117]. The field of superresolution [118, 119] could prove interesting for improving the quality of

sodium MR images keeping in mind advantages and limitations of deep learning techniques for MRI [120]. So far there have not been publications on sodium image enhancement using deep neural networks and there is ample opportunity to explore emerging deep learning techniques that could enhance sodium images and resolve challenges such as long image acquisition times and low resolution. A hurdle is the need for a large number of high-quality training datasets and the risk of errata due to overtraining. Necessity for careful analysis or reevaluation is evident and guidelines for medical images should be established to guarantee meaningful data that can be used for diagnosis or treatment monitoring. As the quality of the sodium images lies at the basis for classification and deep learning techniques, keeping mathematical reconstruction methods and refining further the signal acquisition concepts to improve the poor SNR are still important tasks not to be forgotten in the age of artificial intelligence. Specifically for the work of this thesis, the multi-parametric fitting routines could be optimized in the future by e.g., using a neural network approach[121, 122] and even considering the multiple dimensions instead of working voxel per voxel.

10 Conclusion

TQ signal was investigated as a biomarker for cell viability. TQ signal disappeared for non-viable cells viable cells whereas for viable cells a TQ signal was obtained. A TQ signal decrease was found during simulated ischemia in neonatal cardiomyocytes. The intra versus extracellular study based on the liposomes yielded TQ signal formation due to interaction of the sodium ions with the negatively charged fatty acid chains. A separation of the compartments based on TQ signal is not possible except if toxic shift reagents are being used. Simulation of the different phase cycling techniques proofed an important tool to understand the deleterious effects of magnetic field inhomogeneity (B0) as well as its remedy by acquiring two phase cycles in quadrature that are reconstructed together to be robust against B0. These phase cycles were successfully implemented in the CRISTINA sequence at clinical scanners and successfully validated on an agar phantom. The study on five healthy volunteers showed the importance of B0 field robustness and a TQ signal as well as TQ to SQ ratio maps were acquired. Further clinical studies are needed to measure the differences of TQ and TQ over SQ signal in pathologies. In conclusion, the TQ signal could be an indicator of cell viability and be utilized in future clinical studies to relate changes of the MQ multi-echo signal evolution to pathologies.

List of Publications

11

Journal Articles related to the thesis

- 2019 Hoesl MAU, Schad LR, S Rapacchi, Efficient 23Na triple-quantum signal imaging on clinical scanners - Cartesian Imaging of Single and Triple-Quantum 23Na (CRISTINA). Magn Reson Medicine. submitted Sept 2019, MRM-19-20481

- 2019 Hoesl MAU, Kleimaier D, Hu R, et al. 23Na Triple-quantum signal of in vitro human liver cells, liposomes, and nanoparticles: Cell viability assessment vs. separation of intra- and extracellular signal. J Magn Reson Imaging. 2019:1-10. doi:10.1002/jmri.26666

- 2019 Hu R, Kleimaier D, Malzacher M, Hoesl MAU, Paschke NK, Schad LR. X-nuclei imaging: Current state, technical challenges, and future directions. J Magn Reson Imaging. 2019;0(0). doi:10.1002/jmri.26780

Further Journal Articles

- 2017 Allison Toltz Michaela Hoesl Jan Schuemann Jan Seuntjens Hsiao-Ming Lu Harald Paganetti “Time-resolved diode dosimetry calibration through Monte Carlo modeling for in vivo passive scattered proton therapy range verification”, Journal of Applied Clinical Medical Physics, 18(6). doi: 10.1002/acm2.12210.

- 2016 Maspero M, Seevinck P R, Schubert G, Hoesl M A U, Asselen B van, Viergever M A, Lagendijk J J W, Meijer G J, Berg C A T van den 2017 Quantification of confounding factors in MRI-based dose calculations as applied to prostate IMRT *Phys. Med. Biol. 62*

- 2015 Hoesl M, Deepak S, Moteabbed M, Park Y, Orbain J, Bentefour E and Lu H 2015 Clinical Commissioning of An In-Vivo Range Verification System for Prostate Cancer Treatment with Anterior and Anterior Oblique Proton Beams *Phys Med Biol 42*

Conference Contributions (selection)

- ISMRM 2020 - submittedM Hoesl et al. Proc. Intl. Soc. Mag. Reson. 6172“ Efficient clinical multi-echo, multi-quantum sodium MRI sequence ”,Non-Proton MRS/MRI
- ISMRM 2019 M Hoesl et al. Proc. Intl. Soc. Mag. Reson. 6172“Non-invasive assessment of myocardial cell viability based on 23Na triple-quantum signal”,Non-Proton MRS/MRI
- ISMRM 2018 M Hoesl et al. Proc. Intl. Soc. Mag. Reson. 7678 “Can sodium triple-quantum signal separate extra- and intracellular signals? investigation on HEP G2 liver cells, liposomes and nanoparticles”,Non-Proton MRS/MRI
- ISMRM 2018 M Hoesl et al. Proc. Intl. Soc. Mag. Reson. 6181 “Voxel localization for sodium NMR triple-quantum signal; sequence design and test in agarose phantoms and in-vivo rat”, Non-Proton MRS/MRI
- ESTRO 2018 Bluemink, J. J., Hoesl, M., Seravalli, E., Van den Berg, C. A. T., Raaymakers, B. W., Visser, J. (2018). PO-0920: Proton planning on segmented CTs for head and neck tumors. Radiotherapy and Oncology, 127, S494-S495.
- ISMRM Benelux 2016 Oral: M Hoesl et al. “Fast generation of pseudo-CT in the Head and Neck for MR guided Radiotherapy”
- ISMRM 2016 M Hoesl et al. Proc. Intl. Soc. Mag. Reson. Med. 24 (2016) 2115“Fast generation of pseudo-CT in the Head and Neck for MR guided Radiotherapy”
- AAPM 2015 M Hoesl et al. *Med. Phys. 42* 2015“Clinical Commissioning of An In-Vivo Range Verification System for Prostate Cancer Treatment with Anterior and Anterior Oblique Proton Beams”
- AAPM 2015 Poster: Toltz A, Hoesl M, Schuemann J, Seuntjens J, Lu H and Paganetti, In-Vivo Diode Dosimetry Proton Therapy Range Verification Validation Study for Pediatric CSI *Med. Phys. 42*
- AAPM 2016 Poster: Maspero M, Seevinck P, Schubert G, Hoesl M, Meijer G, Viergever M, Lagendijk J, and van den Berg C (2016), Comparison Study for CT and MR-Only Prostate IMRT Treatment Planning, *Med. Phys 43*

Bibliography

[1]Geoffrey Bodenhausen. “MULTIPLE-QUANTUM NMR”. In: *Prog. Nucl. Magn. Reson. Spectrosc.* 14 (1980), pp. 137–173 (cit. on p. 3).

[2]G. Bodenhausen, R. L. Vold, and R. R. Vold. “Multiple quantum spin-echo spectroscopy”. In: *J. Magn. Reson.* 37.1 (1980), pp. 93–106 (cit. on p. 3).

[3]Geoffrey Bodenhausen, Herbert Kogler, and R. R. Ernst. “Selection of coherence-transfer pathways in NMR pulse experiments”. In: *J. Magn. Reson.* 58.3 (1984), pp. 370–388 (cit. on pp. 3, 71).

[4]Guy Jaccard, Stephen Wimperis, and Geoffrey Bodenhausen. “Multiple-quantum NMR spectroscopy of S=3/2 spins in isotropic phase: A new probe for multiexponential relaxation”. In: *J. Chem. Phys.* 85.11 (1986), p. 6282 (cit. on pp. 3, 6, 43, 71, 72).

[5]James Pekar and John S. Leigh. “Detection of biexponential relaxation in sodium-23 facilitated by double-quantum filtering”. In: *J. Magn. Reson.* 69.3 (1986), pp. 582–584 (cit. on pp. 3, 5, 6).

[6]J. R. C. van der Maarel. “Relaxation of spin quantum number S=3/2 under multiple-pulse quadrupolar echoes”. In: *J. Chem. Phys.* 94.7 (1991), p. 4765 (cit. on p. 3).

[7]S. P. Yu, L. M.T. Canzoniero, and D. W. Choi. “Ion homeostasis and apoptosis”. In: *Curr. Opin. Cell Biol.* 13.4 (2001), pp. 405–411 (cit. on p. 4).

[8]Carl D. Bortner and John A. Cidlowski. “Uncoupling cell shrinkage from apoptosis reveals that Na+ influx is required for volume loss during programmed cell death”. In: *J. Biol. Chem.* 278.40 (2003), pp. 39176–39184 (cit. on p. 4).

[9]Guillaume Madelin and Ravinder R. Regatte. “Biomedical applications of sodium MRI in vivo”. In: *J. Magn. Reson. Imaging* 38.3 (2013), pp. 511–529 (cit. on pp. 4, 53).

[10]Paul A. Bottomley. “Sodium MRI in human heart: A review”. In: *NMR Biomed.* 29.2 (2014), pp. 187–196 (cit. on pp. 4, 5, 53).

[11]Keith R. Thulborn, Denise Davis, James Snyder, Howard Yonas, and Amin Kassam. “Sodium MR Imaging of Acute and Subacute Stroke for Assessment of Tissue Viability”. In: *Neuroimaging Clin. N. Am.* 15.3 (Aug. 2005), pp. 639–653 (cit. on p. 4).

[12]Muhammad S Hussain, Robert W Stobbe, Yusuf A Bhagat, et al. “Sodium imaging intensity increases with time after human ischemic stroke”. In: *Ann. Neurol.* 66.1 (July 2009), pp. 55–62 (cit. on p. 4).

[13]Wafaa Zaaraoui, Simon Konstandin, Bertrand Audoin, et al. “Distribution of Brain Sodium Accumulation Correlates with Disability in Multiple Sclerosis: A Crosssectional 23Na MR Imaging Study”. In: *Radiology* 264.3 (Sept. 2012), pp. 859–867 (cit. on p. 4).

[14]M. Inglese, G. Madelin, N. Oesingmann, et al. “Brain tissue sodium concentration in multiple sclerosis: A sodium imaging study at 3 tesla”. In: *Brain* 133.3 (2010), pp. 847–857 (cit. on p. 4).

[15]Maria Petracca, Roxana O. Vancea, Lazar Fleysher, et al. “Brain intra- and extracellular sodium concentration in multiple sclerosis: a 7 T MRI study”. In: *Brain* 139.3 (Jan. 2016), pp. 795–806 (cit. on p. 4).

[16]K. A. Dani and S. Warach. “Metabolic Imaging of Ischemic Stroke: The Present and Future”. In: *American Journal of Neuroradiology* 35.6 suppl (June 2014) (cit. on p. 4).

[17]A. Biller, S. Badde, A. Nagel, et al. “Improved brain tumor classification by sodium MR imaging: Prediction of IDH mutation status and tumor progression”. In: *Am. J. Neuroradiol.* 37.1 (2016), pp. 66–73 (cit. on p. 4).

[18]Frank G. Zoellner, Raffi Kalayciyan, Jorge Chacón-Caldera, Fabian Zimmer, and Lothar R. Schad. “Pre-clinical functional Magnetic Resonance Imaging part I: The kidney”. In: *Zeitschrift für Medizinische Physik* 24.4 (Dec. 2014), pp. 286–306 (cit. on p. 4).

[19]Frank G. Zoellner, Simon Konstandin, Jonathan Lommen, et al. “Quantitative sodium MRI of kidney”. In: *NMR in Biomedicine* 29.2 (Feb. 2016), pp. 197–205 (cit. on p. 4).

[20]N Jon Shah, Wieland A Worthoff, and Karl-Josef Langen. “Imaging of sodium in the brain: a brief review”. In: *NMR Biomed.* 29.2 (Feb. 2016), pp. 162–174 (cit. on p. 4).

[21]A Guermazi, H Alizai, M D Crema, et al. “Compositional MRI techniques for evaluation of cartilage degeneration in osteoarthritis”. In: *Osteoarthr. Cartil.* 23.10 (Oct. 2015), pp. 1639–1653 (cit. on p. 4).

[22]Michaela A.U. Hoesl, Dennis Kleimaier, Ruomin Hu, et al. “23Na Triple-quantum signal of in vitro human liver cells, liposomes, and nanoparticles: Cell viability assessment vs. separation of intra- and extracellular signal”. In: *J. Magn. Reson. Imaging* (2019), pp. 1–10 (cit. on pp. 4, 9).

[23]William D Rooney, Xin Li, Manoj K Sammi, et al. “Mapping human brain capillary water lifetime: high?resolution metabolic neuroimaging”. In: *NMR Biomed.* 28.6 (2015), pp. 607–623 (cit. on p. 4).

[24]Deborah Burstein and Charles S Springer Jr. “Sodium MRI revisited”. In: *Magn. Reson. Med.* 82.2 (Aug. 2019), pp. 521–524 (cit. on p. 5).

[25]Gil Navon. “Complete elimination of the extracellular 23Na NMR signal in triple quantum filtered spectra of rat hearts in the presence of shift reagents”. In: *Magn. Reson. Med.* 30.4 (1993), pp. 503–506 (cit. on p. 5).

[26]Patrick M Winter and Navin Bansal. “Triple-Quantum-Filtered 23Na NMR Spectroscopy of Subcutaneously Implanted 9L Gliosarcoma in the Rat in the Presence of TmDOTP5?” In: *J. Magn. Reson.* 152.1 (2001), pp. 70–78 (cit. on p. 5).

[27]W. D. Rooney and Jr. Springer. “A Comprehensive Approach to the Analysis and Interpretation of the Resonances of Spins 3 / 2 from-Living Systems”. In: *NMR Biomed.* 4 (Mar. 1991), pp. 209–226 (cit. on pp. 5, 6).

[28]Victor D. Schepkin, Isaac O. Choy, Thomas F. Budinger, J. Nilas Young, and William M. Decampli. “Multi-dose crystalloid cardioplegia preserves intracellular sodium homeostasis in myocardium”. In: *J. Mol. Cell. Cardiol.* 31.9 (1999), pp. 1643–1651 (cit. on p. 5).

[29]Victor D. Schepkin, Andreas Neubauer, Armin M. Nagel, and Thomas F. Budinger. “Comparison of potassium and sodium binding in vivo and in agarose samples using TQTPPI pulse sequence”. In: *J. Magn. Reson.* 277 (2017), pp. 162–168 (cit. on pp. 5, 43, 71–73).

[30]Ronald Ouwerkerk. “Sodium Magnetic Resonance Imaging: From Research to Clinical Use”. In: *J. Am. Coll. Radiol.* 4.10 (2007), pp. 739–741 (cit. on p. 5).

[31]Adrian Tsang, Robert W. Stobbe, and Christian Beaulieu. “Triple-quantum-filtered sodium imaging of the human brain at 4.7 T”. In: *Magn. Reson. Med.* 67.6 (June 2012), pp. 1633–1643 (cit. on p. 5).

[32]Simon Konstandin and Armin M. Nagel. “Measurement techniques for magnetic resonance imaging of fast relaxing nuclei”. In: *Magn. Reson. Mater. Physics, Biol. Med.* 27.1 (2014), pp. 5–19 (cit. on pp. 5, 30).

[33]Stephen F Lincoln and Andre E Merbach. “Substitution reactions of solvated metal ions”. In: *Adv. Inorg. Chem.* 42.LCIB-ARTICLE-1995-009 (1995), pp. 1–88 (cit. on p. 5).

[34]Bruce Alberts, A Johnson, J Lewis, et al. *Molecular Biology of the Cell, 4th edition*. New York: Garland Science, 2002 (cit. on pp. 5, 50).

[35]William D. Rooney and Charles S. Springer. “The molecular environment of intracellular sodium:23Na NMR relaxation”. In: *NMR Biomed.* 4.5 (Oct. 1991), pp. 227–245 (cit. on p. 6).

[36]Richard Kemp-Harper, Steven P Brown, Colan E Hughes, Peter Styles, and Stephen Wimperis. “23 Na NMR methods for selective observation of sodium ions in ordered environments”. In: *Prog. Nucl. Magn. Reson. Spectrosc.* 30.3-4 (1997), p. 157 (cit. on p. 6).

[37]Johan R C Van Der Maarel. “Thermal relaxation and coherence dynamics of spin 3/2. I. Static and fluctuating quadrupolar interactions in the multipole basis”. In: *Concepts Magn. Reson. Part A Bridg. Educ. Res.* 19.2 (2003), pp. 97–116 (cit. on pp. 6, 43).

[38]Johan R C Van Der Maarel. “Thermal relaxation and coherence dynamics of spin 3/2. II. Strong radio-frequency field”. In: *Concepts Magn. Reson. Part A Bridg. Educ. Res.* 19.2 (2003), pp. 117–133 (cit. on pp. 6, 43).

[39]A.D. Bangham. “Model membranes”. In: *Chem. Phys. Lipids* 8.4 (1972), pp. 386–392 (cit. on p. 8).

[40]H Hauser, MC Phillips, M Stubbs, and T Ženiš. “Ion permeability of phospholipid”. In: *Nature* 239.5371 (1972), pp. 342–344 (cit. on pp. 8, 108).

[41]Anthony Carruthers and Donald L. Melchior. “How bilayer lipids affect membrane protein activity”. In: *Trends Biochem. Sci.* 11.8 (1986), pp. 331–335 (cit. on p. 8).

[42]Rebecca L. McCall and Rachael W. Sirianni. “PLGA Nanoparticles Formed by Single- or Double-emulsion with Vitamin E-TPGS”. In: *J. Vis. Exp.* 82 (2013), pp. 1–8 (cit. on pp. 8, 49).

[43]Fabienne Danhier, Eduardo Ansorena, Joana M. Silva, et al. “PLGA-based nanoparticles: An overview of biomedical applications”. In: *J. Control. Release* 161.2 (2012), pp. 505–522 (cit. on p. 8).

[44]Eric Gottwald, Tanja Kleintschek, Stefan Giselbrecht, et al. “Characterization of a chip-based bioreactor for three-dimensional cell cultivation via Magnetic Resonance Imaging”. In: *Z. Med. Phys.* 23.2 (2013), pp. 102–110 (cit. on pp. 8, 50, 52).

[45]Andreas Neubauer, Cordula Nies, Victor D. Schepkin, et al. “Tracking protein function with sodium multi quantum spectroscopy in a 3D-tissue culture based on microcavity arrays”. In: *Sci. Rep.* 7.1 (2017), p. 3943 (cit. on pp. 8, 109).

[46]Michaela A.U. Hoesl, Stanislas Rappachi, and Lothar Schad. “Efficient 23Na triple-quantum signal imaging on clinical scanners - Cartesian Imaging of Single and Triple-Quantum 23Na (CISTINA)”. In: *Magn. Reson. Medicine* (2019) (cit. on p. 9).

[47]J J Sakurai. *Modern Quantum Mechanics*. Ed. by San Fu Tuan. Addison-Wesley Publishing Company, 1994 (cit. on p. 12).

[48]M E Haacke, R W Brown, M R Thompson, and R Venkatesen. *Magnetic Resonance Imaging: Physical Principles and Sequence Design.* John Wiley & Sons; Second edition, 2014 (cit. on p. 13).

[49]Guillaume Madelin. “Sodium Magnetic Resonance Imaging: Biomedical Applications”. In: long version of a review article that will be published in Journal of Magnetic Resonance Imaging in 2013 (Dec. 2012). arXiv: 1212.4400 (cit. on pp. 16, 17, 40, 95, 114).

[50]Matthias A Dieringer, Michael Deimling, Davide Santoro, et al. “Rapid parametric mapping of the longitudinal relaxation time T1 using two-dimensional variable flip angle magnetic resonance imaging at 1.5 Tesla, 3 Tesla, and 7 Tesla”. In: *PLoS One* 9.3 (Mar. 2014), e91318–e91318 (cit. on p. 17).

[51]Ronald N (Ronald Newbold) Bracewell. *The Fourier transform and its applications*. Second edition. New York : McGraw-Hill, [1978] ©1978, 1978 (cit. on p. 20).

[52]Richard G. Brewer and Erwin L. Hahn. “Atomic Memory”. In: *Sci. Am.* 251.6 (1984), pp. 50–57 (cit. on p. 23).

[53]Gengsheng L. Zeng. “A fast method to emulate an iterative POCS image reconstruction algorithm”. In: *Med. Phys.* 44.10 (2017), e353–e359 (cit. on p. 27).

[54]Fernando E. Boada, James D. Christensen, Frank R. Huang-Hellinger, Timothy G. Reese, and Keith R. Thulborn. “Quantitativein vivo tissue sodium concentration maps: The effects of biexponential relaxation”. In: *Magn. Reson. Med.* 32.2 (Aug. 1994), pp. 219–223 (cit. on p. 29).

[55]Jurgen Rahmer, Peter Bornert, Jan Groen, and Clemens Bos. “Three-dimensional radial ultrashort echo-time imaging with T2 adapted sampling”. In: *Magn. Reson. Med.* 55.5 (May 2006), pp. 1075–1082 (cit. on p. 29).

[56]Sonia Nielles-Vallespin, Marc Andre Weber, and Michael et al. Bock. “3D radial projection technique with ultrashort echo times for sodium MRI: Clinical applications in human brain and skeletal muscle”. In: *Magn. Reson. Med.* 57.1 (Jan. 2007), pp. 74–81 (cit. on p. 29).

[57]Fernando E. Boada, Joseph S. Gillen, Gary X. Shen, Sam Y Chang, and Keith R. Thulborn. “Fast three dimensional sodium imaging”. In: *Magn. Reson. Med.* 37.5 (), pp. 706–715 (cit. on p. 29).

[58]Fernando E. Boada, Gary X. Shen, Sam Y. Chang, and Keith R. Thulborn. “Spectrally weighted twisted projection imaging: Reducing T2 signal attenuation effects in fast three-dimensional sodium imaging”. In: *Magn. Reson. Med.* 38.6 (Dec. 1997), pp. 1022–1028 (cit. on pp. 29, 114).

[59]Armin M. Nagel, Frederik B. Laun, Marc André Weber, et al. “Sodium MRI using a density-adapted 3D radial acquisition technique”. In: *Magn. Reson. Med.* 62.6 (2009), pp. 1565–1573 (cit. on pp. 29, 30).

[60]Paul T. Gurney, Brian A. Hargreaves, and Dwight G. Nishimura. “Design and analysis of a practical 3D cones trajectory”. In: *Magn. Reson. Med.* 55.3 (Mar. 2006), pp. 575–582 (cit. on p. 29).

[61]Yongxian Qian and Fernando E. Boada. “Acquisition-weighted stack of spirals for fast high-resolution three-dimensional ultra-short echo time MR imaging”. In: *Magn. Reson. Med.* 60.1 (July 2008), pp. 135–145 (cit. on pp. 29, 30).

[62]James G. Pipe, Nicholas R. Zwart, Eric A. Aboussouan, et al. “A new design and rationale for 3D orthogonally oversampled k-space trajectories”. In: *Magn. Reson. Med.* 66.5 (Nov. 2011), pp. 1303–1311 (cit. on pp. 29, 30, 114).

[63]Ryan K. Robison, Ashley G. Anderson, and James G. Pipe. “Three-dimensional ultrashort echo-time imaging using a FLORET trajectory”. In: *Magn. Reson. Med.* 78.3 (Sept. 2017), pp. 1038–1049 (cit. on pp. 29, 30).

[64]Dennis L. Parker, Grant T. Gullberg, and Philip R. Frederick. “Gibbs artifact removal in magnetic resonance imaging”. In: *Med. Phys.* 14.4 (July 1987), pp. 640–645 (cit. on p. 29).

[65]J.M. Star-Lack. “Optimal gradient waveform design for projection imaging and projection reconstruction echoplanar spectroscopic imaging”. In: *Magn. Reson. Med.* 41.4 (Apr. 1999), pp. 664–675 (cit. on p. 29).

[66]Ian C. Atkinson, Aiming Lu, and Keith R. Thulborn. “Clinically constrained optimization of flexTPI acquisition parameters for the tissue sodium concentration bioscale”. In: *Magn. Reson. Med.* 66.4 (Oct. 2011), pp. 1089–1099 (cit. on p. 29).

[67]Yongxian Qian, V. Andrew Stenger, and Fernando E. Boada. “Parallel imaging with 3D TPI trajectory: SNR and acceleration benefits”. In: *Magn. Reson. Imaging* 27.5 (June 2009), pp. 656–663 (cit. on p. 29).

[68]Guillaume Madelin, Gregory Chang, Ricardo Otazo, Alexej Jerschow, and Ravinder R. Regatte. “Compressed sensing sodium MRI of cartilage at 7T: Preliminary study”. In: *J. Magn. Reson.* 214 (Jan. 2012), pp. 360–365 (cit. on p. 29).

[69]Klaas P. Pruessmann, Markus Weiger, Markus B. Scheidegger, and Peter Boesiger. “SENSE: Sensitivity encoding for fast MRI”. In: *Magn. Reson. Med.* 42.5 (Nov. 1999), pp. 952–962 (cit. on pp. 29, 114).

[70]Simon Konstandin and Armin M. Nagel. “Performance of sampling density-weighted and postfiltered density-adapted projection reconstruction in sodium magnetic resonance imaging”. In: *Magn. Reson. Med.* 69.2 (2013), pp. 495–502 (cit. on p. 30).

[71]Christian Mirkes, G. Shajan, Jonas Bause, et al. “Triple-quantum-filtered sodium imaging at 9.4 Tesla”. In: *Magn. Reson. Med.* 75.3 (Mar. 2016), pp. 1278–1289 (cit. on p. 30).

[72]Sandro Romanzetti, Christian C. Mirkes, Daniel P. Fiege, et al. “Mapping tissue sodium concentration in the human brain: A comparison of MR sequences at 9.4Tesla”. In: *Neuroimage* 96 (Aug. 2014), pp. 44–53 (cit. on p. 30).

[73]J I Jackson, C H Meyer, D G Nishimura, and A Macovski. “Selection of a convolution function for Fourier inversion using gridding (computerised tomography application)”. In: *IEEE Trans. Med. Imaging* 10.3 (1991), pp. 473–478 (cit. on p. 30).

[74]James G. Pipe and Padmanabhan Menon. “Sampling density compensation in MRI: Rationale and an iterative numerical solution”. In: *Magn. Reson. Med.* 41.1 (Jan. 1999), pp. 179–186 (cit. on p. 30).

[75]Kenneth O. Johnson and James G. Pipe. “Convolution kernel design and efficient algorithm for sampling density correction”. In: *Magn. Reson. Med.* 61.2 (Feb. 2009), pp. 439–447 (cit. on p. 30).

[76]Ryan K. Robison, Ajit Devaraj, and James G. Pipe. “Fast, simple gradient delay estimation for spiral MRI”. In: *Magn. Reson. Med.* 63.6 (June 2010), pp. 1683–1690 (cit. on p. 30).

[77]Ergun Ahunbay and James G. Pipe. “Rapid method for deblurring spiral MR images”. In: *Magn. Reson. Med.* 44.3 (Sept. 2000), pp. 491–494 (cit. on p. 30).

[78]Sebastian Weingartner, Friedrich Wetterling, Simon Konstandin, et al. “Scan time reduction in 23Na-Magnetic Resonance Imaging using the chemical shift imaging sequence: Evaluation of an iterative reconstruction method.” In: *Zeitschrift fur medizinische Phys.* 25.3 (2015), pp. 275–86 (cit. on p. 30).

[79]Tanja Platt, Reiner Umathum, Thomas M. Fiedler, and Armin M. et al. Nagel. “In vivo self-gated 23Na MRI at 7 T using an oval-shaped body resonator”. In: *Magn. Reson. Med.* 3 (Sept. 2018), pp. 1005–1019 (cit. on p. 30).

[80]Herman J C Berendsen and Hommo T Edzes. “THE OBSERVATION AND GENERAL INTERPRETATION OF SODIUM MAGNETIC RESONANCE IN BIOLOGICAL MATERIAL”. In: *Ann. N. Y. Acad. Sci.* 204.1 (Mar. 1973), pp. 459–485 (cit. on p. 42).

[81]J A Magnuson and N S Magnuson. “NMR STUDIES OF SODIUM AND POTASSIUM IN VARIOUS BIOLOGICAL TISSUES”. In: *Ann. N. Y. Acad. Sci.* 204.1 (Mar. 1973), pp. 297–309 (cit. on p. 42).

[82]D Marion. “Reprint of Application of phase sensitive two-dimensional correlated spectroscopy (COSY) for measurements of 1H 1H spin spin coupling constants in proteins”. In: *Biochem. Biophys. Res. Commun.* 425.3 (2012), pp. 519–526 (cit. on pp. 43, 71, 72).

[83]G Drobny, A Pines, S Sinton, D P Weitekamp, and D Wemmer. “Fourier transform multiple quantum nuclear magnetic resonance”. In: *Faraday Symp. Chem. Soc.* 13 (1978), pp. 49–55 (cit. on p. 43).

[84]Zsolt Ugray, Leon Lasdon, John Plummer, et al. “Scatter search and local NLP solvers: A multistart framework for global optimization”. In: *INFORMS J. Comput.* 19.3 (2007), pp. 328–340 (cit. on p. 44).

[85]F S Moolman, H Rolfes, S W Van Der Merwe, and W W Focke. “Optimization of perfluorocarbon emulsion properties for enhancing oxygen mass transfer in a bio-artificial liver support system”. In: *Biochem. Eng. J.* 19.3 (2004), pp. 237–250 (cit. on p. 49).

[86]Uri M. “Size of HepG2 (liver carcinoma) cell”. In: *B10Numbers* (2004), p. ID 108919 (cit. on p. 49).

[87]Torben Clausen. “Na+-K+ Pump Regulation and Skeletal Muscle Contractility”. In: *Physiol. Rev.* 83.4 (Oct. 2003), pp. 1269–1324 (cit. on p. 52).

[88]Ronald Ouwerkerk, Paul A Bottomley, Amy E Spooner, et al. “Tissue Sodium Concentration in Myocardial Infarction in Humans: A Quantitative 23Na MR Imaging Study”. In: *Radiology* 248.1 (2008) (cit. on p. 53).

[89]Angela K Peter, Maureen A Bjerke, and Leslie A Leinwand. “Biology of the cardiac myocyte in heart disease”. In: *Mol. Biol. Cell* 27.14 (July 2016), pp. 2149–2160 (cit. on p. 53).

[90]“Cardiomyocyte-Specific miRNA-30c Over-Expression Causes Dilated Cardiomyopathy”. In: *PLoS One* 9.5 (May 2014), e96290 (cit. on pp. 53, 110).

[91]Johannes Backs, Barbara C Worst, Lorenz H Lehmann, et al. “Selective repression of MEF2 activity by PKA-dependent proteolysis of HDAC4”. In: *J. Cell Biol.* 195.3 (Oct. 2011), pp. 403–415 (cit. on p. 53).

[92]Jian-xin Shen. “Isoprenaline enhances local Ca2+ release in cardiac myocytes”. In: *Acta Pharmacol. Sin.* 27 (July 2006), p. 927 (cit. on pp. 53, 110).

[93]Lazar Fleysher, Niels Oesingmann, and Matilde Inglese. “B0 inhomogeneity-insensitive triple-quantum-filtered sodium imaging using a 12-step phase-cycling scheme”. In: *NMR Biomed.* 23.10 (2010), pp. 1191–1198 (cit. on pp. 71, 73, 76).

[94]Daniel P. Fiege, Sandro Romanzetti, Christian C. Mirkes, Daniel Brenner, and N. Jon Shah. “Simultaneous single-quantum and triple-quantum-filtered MRI of 23Na (SISTINA)”. In: *Magn. Reson. Med.* 69.6 (2013), pp. 1691–1696 (cit. on pp. 71, 73, 112).

[95]Costin Tanase and Fernando E Boada. “Triple-quantum-filtered imaging of sodium in presence of B 0 inhomogeneities”. In: *J. Magn. Reson.* 174 (2005), pp. 270–278 (cit. on p. 73).

[96]E. L. Hahn. “Spin Echoes”. In: *Phys. Rev.* 73.679 (1948), pp. 580–591 (cit. on p. 73).

[97]Peter B. Kingsley. “Product operators, coherence pathways, and phase cycling. Part II. coherence pathways in multipulse sequences: spin echoes, stimulated echoes, and multiple quantum coherences”. In: *Concepts Magn. Reson.* 7.2 (1995), pp. 115–136 (cit. on p. 73).

[98]Deborah Burstein. “Stimulated echoes: Description, applications, practical hints”. In: *Concepts Magn. Reson.* 8.4 (1996), pp. 269–278 (cit. on p. 73).

[99]A. Carruthers and D. L. Melchior. “Studies of the Relationship between Bilayer Water Permeability and Bilayer Physical State”. In: *Biochemistry* 22.25 (1983), pp. 5797–5807 (cit. on p. 108).

[100]David W. Deamer and John Bramhall. “Permeability of lipid bilayers to water and ionic solutes”. In: *Chem. Phys. Lipids* 40.2-4 (June 1986), pp. 167–188 (cit. on p. 108).

[101]E London. *Lipid Bilayer Structure*. Elsevier, Encycl. Biol. Chem., 2013, pp. 733–735 (cit. on p. 108).

[102]Rainer A Bockmann, Agnieszka Hac, Thomas Heimburg, and Helmut Grubmuller. “Effect of sodium chloride on a lipid bilayer”. In: *Biophys. J.* 85.3 (2003), pp. 1647–1655.

[103]Malgorzata Kotulska and Krystian Kubica. “Structural and energetic model of the mechanisms for reduced self-diffusion in a lipid bilayer with increasing ionic strength”. In: *Phys. Rev. E* 72.6 (2005), p. 61903 (cit. on p. 108).

[104]Victor D. Schepkin, I. Oojin Choy, Thomas F. Budinger, et al. “Sodium TQF NMR and intracellular sodium in isolated crystalloid perfused rat heart”. In: *Magn. Reson. Med.* 39.4 (1998), pp. 557–563.

[105]Victor D. Schepkin. “Statistical tensor analysis of the MQ MR signals generated by weak quadrupole interactions”. In: *Z. Med. Phys.* (2019), pp. 1–11 (cit. on p. 113).

[106]Yupeng Liao, Nazim Lechea, Arthur W. Magill, et al. “Correlation of quantitative conductivity mapping and total tissue sodium concentration at 3T/4T”. In: *Magn. Reson. Med.* 82.4 (2019), pp. 1518–1526 (cit. on p. 113).

[107]Carlotta Ianniello, Guillaume Madelin, Linda Moy, and Ryan Brown. “A dual-tuned multichannel bilateral RF coil for 1H/23Na breast MRI at 7 T”. In: *Magn. Reson. Med.* 82.4 (2019), pp. 1566–1575 (cit. on p. 113).

[108]Frank Riemer, Damien McHugh, Fulvio Zaccagna, et al. “Measuring Tissue Sodium Concentration: Cross-Vendor Repeatability and Reproducibility of 23 Na-MRI Across Two Sites”. In: *J. Magn. Reson. Imaging* (2019) (cit. on p. 113).

[109]Laura Boehmert, Andre Kuehne, Helmar Waiczies, et al. “Cardiorenal 23Na MRI at 7.0 Tesla using a 4/4 channel 1H/23Na RF antenna array”. In: *Magn. Reson. Med.* March (2019), pp. 2343–2356 (cit. on p. 113).

[110]Li Feng, Robert Grimm, Kai T obias Block, et al. “Golden-angle radial sparse parallel MRI: combination of compressed sensing, parallel imaging, and golden-angle radial sampling for fast and flexible dynamic volumetric MRI”. In: *Magn. Reson. Med.* 72.3 (2014), pp. 707–717 (cit. on p. 114).

[111]Michael Lustig, David L Donoho, and Juan M et al. Santos. “Compressed sensing MRI”. In: *Signal Process. Mag. IEEE* 25.2 (2008), pp. 72–82 (cit. on p. 114).

[112]Michael Paquette, Sylvain Merlet, Guillaume Gilbert, Rachid Deriche, and Maxime Descoteaux. “Comparison of sampling strategies and sparsifying transforms to improve compressed sensing diffusion spectrum imaging”. In: *Magn. Reson. Med.* 73.1 (2015), pp. 401–416 (cit. on p. 114).

[113]Eyal Lotan, Rajan Jain, Narges Razavian, Girish M Fatterpekar, and Yvonne W Lui. “Applications in Glioma Imaging”. In: *Neuroradiol. Neck Imaging* January (2019), pp. 1–12 (cit. on p. 114).

[114]Guillaume Madelin, Frederick Poidevin, Antonios Makrymallis, and Ravinder R. Regatte. “Classification of sodium MRI data of cartilage using machine learning”. In: *Magn. Reson. Med.* 74.5 (2015), pp. 1435–1448 (cit. on p. 114).

[115]Yann Lecun, Yoshua Bengio, and Geoffrey Hinton. “Deep learning”. In: *Nature* 521.7553 (2015), pp. 436–444. arXiv: 1807.07987 (cit. on p. 114).

[116]Shanshan Wang, Zhenghang Su, Leslie Ying, et al. “ACCELERATING MAGNETIC RESONANCE IMAGING VIA DEEP LEARNING Paul C . Lauterbur Research Center for Biomedical Imaging , SIAT , CAS , Shenzhen , P . R . China Department of Biomedical Engineering and Department of Electrical Engineering , The State Universit”. In: *Isbi 2016* (2016), pp. 514–517 (cit. on p. 114).

[117]Sergey Korolev, Amir Safiullin, Mikhail Belyaev, and Yulia Dodonova. “Residual and Plain Convolutional Neural Networks for 3D Brain MRI Classification”. In: *arXiv* (2017). arXiv: 1701.06643 (cit. on p. 114).

[118]Christian Ledig, Lucas Theis, Ferenc Huszar, et al. “Photo-realistic single image super-resolution using a generative adversarial network”. In: *Proc. - 30th IEEE Conf. Comput. Vis. Pattern Recognition, CVPR 2017* 2017-Janua (2017), pp. 105–114. arXiv: 1609.04802 (cit. on p. 114).

[119]Chao Dong, Chen Change Loy, Kaiming He, and Xiaoou Tang. “Image Super-Resolution Using Deep Convolutional Networks”. In: *IEEE Trans. Pattern Anal. Mach. Intell.* 38.2 (Feb. 2016), pp. 295–307 (cit. on p. 114).

[120]Wenling Shang, Kihyuk Sohn, Diogo Almeida, and Honglak Lee. “Understanding and Improving Convolutional Neural Networks via Concatenated Rectified Linear Units”. In: *arXiv* 48 (2016). arXiv: 1603.05201 (cit. on p. 115).

[121]Alena Kathrin Schnurr, Khanlian Chung, Tom Russ, Lothar R. Schad, and Frank G. Zoellner. “Simulation-based deep artifact correction with Convolutional Neural Networks for limited angle artifacts”. In: *Z. Med. Phys.* 29.2 (2019), pp. 150–161 (cit. on p. 115).

[122]Alexander Selvikvåg Lundervold and Arvid Lundervold. “An overview of deep learning in medical imaging focusing on MRI”. In: *Z. Med. Phys.* 29.2 (2019), pp. 102–127 (cit. on p. 115).

List of Figures

List of Tables

Declaration

This thesis is the result of my independent investigation under supervision. Where my work is indebted to the work or ideas of others, for example from the literature or the internet, I have acknowledged this within the thesis.

I declare that this study has not already been accepted for any other degree, nor is it currently being submitted in candidature for any other degree.

I am aware that a false declaration could have legal implications.

Erklearung:
Hiermit erkläre ich, die vorliegende Arbeit selbständig verfasst zu haben und keine anderen als die in der Arbeit angegebenen Quellen und Hilfsmittel benutzt zu haben.

Mannheim, January 22, 2020

Michaela Anna Ulrike Hösl, MSc